

### **Central Lancashire Online Knowledge (CLoK)**

Title	Interstellar Mapping And Acceleration Probe: The NASA IMAP Mission
Type	Article
URL	https://knowledge.lancashire.ac.uk/id/eprint/57378/
DOI	https://doi.org/10.1007/s11214-025-01224-z
Date	2025
Citation	McComas, D. J., Christian, E. R., Schwadron, N. A., Gkioulidou, M., Allegrini, F., Baker, D. N., Bzowski, M., Clark, G., Cohen, C. M. S. et al (2025) Interstellar Mapping And Acceleration Probe: The NASA IMAP Mission. Space Science Reviews, 221 (8). p. 100. ISSN 0038-6308
Creators	McComas, D. J., Christian, E. R., Schwadron, N. A., Gkioulidou, M., Allegrini, F., Baker, D. N., Bzowski, M., Clark, G., Cohen, C. M. S., Cohen, I., Collura, C., Cully, M. J., Dalla, Silvia, Desai, M. I., Driesman, A., Eng, D., Fox, N. J., Funsten, H. O., Fuselier, S. A., Galli, A., Giacalone, J., Hahn, J., Hegarty, K. P., Horbury, T., Horanyi, M., Kistler, L. M., Kubiak, M. A., Kubota, S., Livi, S., Lugaz, N., Lee, C. O., Luhmann, J., Matthaeus, W., Mitchell, D. G., Mitchell, J. G., Moebius, E., Pope, S., Provornikova, E., Rankin, J. S., Reisenfeld, D. B., Reno, C., Richardson, J. D., Russell, C. T., Shaw-Lecerf, M. M., Scherrer, J., Skoug, R. M., Shen, M. M., Spence, H. E., Sternovsky, Z., Strumik, M., Szalay, J. R., Tapley, M., Tokumaru, M., Turner, D. L., Weidner, S., Westlake, J., Wurz, P. and Zank, G. P.

It is advisable to refer to the publisher's version if you intend to cite from the work. https://doi.org/10.1007/s11214-025-01224-z

For information about Research at UCLan please go to <a href="http://www.uclan.ac.uk/research/">http://www.uclan.ac.uk/research/</a>

All outputs in CLoK are protected by Intellectual Property Rights law, including Copyright law. Copyright, IPR and Moral Rights for the works on this site are retained by the individual authors and/or other copyright owners. Terms and conditions for use of this material are defined in the http://clok.uclan.ac.uk/policies/



# Interstellar Mapping And Acceleration Probe: The NASA IMAP Mission

D.J. McComas<sup>1</sup> • E.R. Christian<sup>2</sup> · N.A. Schwadron<sup>3</sup> · M. Gkioulidou<sup>4</sup> · F. Allegrini<sup>5,6</sup> · D.N. Baker<sup>7</sup> · M. Bzowski<sup>8</sup> · G. Clark<sup>4</sup> · C.M.S. Cohen<sup>9</sup> · I. Cohen<sup>4</sup> · C. Collura<sup>4</sup> · M.J. Cully<sup>4</sup> · S. Dalla<sup>10</sup> · M.I. Desai<sup>5,6</sup> · A. Driesman<sup>4</sup> · D. Eng<sup>4</sup> · N.J. Fox<sup>11</sup> · H.O. Funsten<sup>12</sup> · S.A. Fuselier<sup>5,6</sup> · A. Galli<sup>13</sup> · J. Giacalone<sup>14</sup> · J. Hahn<sup>4</sup> · K.P. Hegarty<sup>4</sup> · T. Horbury<sup>15</sup> · M. Horanyi<sup>7</sup> · L.M. Kistler<sup>3</sup> · M.A. Kubiak<sup>5</sup> · S. Kubota<sup>4</sup> · S. Livi<sup>5</sup> · N. Lugaz<sup>3</sup> · C.O. Lee<sup>16</sup> · J. Luhmann<sup>16</sup> · W. Matthaeus<sup>17</sup> · D.G. Mitchell<sup>4</sup> · J.G. Mitchell<sup>2</sup> · E. Moebius<sup>3</sup> · S. Pope<sup>5</sup> · E. Provornikova<sup>4</sup> · J.S. Rankin<sup>1</sup> · D.B. Reisenfeld<sup>12</sup> · C. Reno<sup>1</sup> · J.D. Richardson<sup>18</sup> · C.T. Russell<sup>19</sup> · M.M. Shaw-Lecerf<sup>1</sup> · J. Scherrer<sup>4</sup> · R.M. Skoug<sup>12</sup> · M.M. Shen<sup>1</sup> · H.E. Spence<sup>3</sup> · Z. Sternovsky<sup>7</sup> · M. Strumik<sup>8</sup> · J.R. Szalay<sup>1</sup> · M. Tapley<sup>5</sup> · M. Tokumaru<sup>20</sup> · D.L. Turner<sup>4</sup> · S. Weidner<sup>1</sup> · J. Westlake<sup>11</sup> · P. Wurz<sup>11</sup> · G.P. Zank<sup>21,22</sup>

Received: 24 June 2025 / Accepted: 1 October 2025 © The Author(s) 2025

#### Abstract

NASA's Interstellar Mapping and Acceleration Probe (IMAP) mission provides extensive and well-coordinated new observations of the inner and outer heliosphere and scientific closure on two of the most important topics in Heliophysics: 1) the acceleration of charged particles and 2) the interaction of the solar wind with the local interstellar medium. These topics are intimately coupled because particles accelerated in the inner heliosphere propagate outward through the solar wind and mediate its interaction with the very local interstellar medium (VLISM). The IMAP mission is designed to address these topics, provide extensive new real-time measurements critical to Space Weather observations and predictions, and much more. IMAP's ten instruments are mounted on a simple, spinning spacecraft that orbits about the first Sun-Earth Lagrange point, L1, and repoints its Sun-facing solar arrays and spin axis toward the Sun each day. The instruments provide complete and synergistic observations that examine particle energization processes at 1 au while simultaneously probing the global heliospheric interaction with the VLISM. The 1 au in-situ observations include solar wind electrons and ions from solar wind through suprathermal energies, pickup and energetic ions, as well as the interplanetary magnetic field. IMAP provides Energetic Neutral Atom (ENA) global imaging of the outer heliosphere via ENAs from tens of eV up through hundreds of keV, as well as observations of interstellar neutral atoms traversing the heliosphere. IMAP also directly measures interstellar dust that enters the heliosphere and the solar-wind-modulated ultraviolet glow. This paper provides the mission overview for the full IMAP mission, acts as a roadmap to the other papers in this IMAP collection and provides the citable reference for the overall IMAP mission going forward.

**Keywords** Heliosphere · Space weather · Interstellar medium · ENAs · Energetic particles · Solar wind · Plasma · Magnetic fields · IBEX · IMAP

Extended author information available on the last page of the article





100 Page 2 of 82 D.J. McComas et al.



Fig. 1 Logos of the 25 institutions involved in IMAP's science and/or development of the mission. These institutions span 12 US states and five other countries (UK, Poland, Switzerland, Germany, and Japan)

#### 1 Mission Overview

The Interstellar Mapping and Acceleration Probe (IMAP), with an international team of 25 partner institutions (Fig. 1), uses a suite of 10 scientific instruments to create comprehensive maps of the Sun's galactic interaction, including measurements of the solar wind, high-energy particles, and magnetic fields in interplanetary space, as well as interstellar and solar system dust grains. This groundbreaking NASA Heliophysics mission simultaneously investigates two compelling and linked fundamental problems in space physics today, the acceleration of charged particles to high energies, and how the interaction of these high energy particles with the local interstellar medium structures and defines our heliosphere.

The heliosphere – our home in the galaxy – is the region of space surrounding our solar system, which is dominated by the Sun's presence. It is formed by the million mile-perhour solar wind, which flows outward from the Sun in all directions in space, all the time, inflating a "bubble" in the very local interstellar medium (VLISM). The heliosphere shields the solar system from most of the harsh particle radiation present in the galaxy, thereby creating a habitable zone that includes our home on Earth and making human exploration to our neighboring planets (e.g., Mars) even possible. Understanding the physics of the outer heliosphere and its dynamically evolving interaction with the VLISM over time can help us comprehend our solar system's place in, and interaction with, the galaxy.

Our heliosphere exists in the domain of the interstellar medium, undergoing significant interactions near the edge of the local interstellar cloud. The understanding of the interstellar magnetic field and its broader connection with the field throughout the galactic medium is essential for understanding high energy cosmic rays (e.g., Schwadron et al. 2014b), and the galactic medium. The heliosphere and the VLISM immediately outside it provide the lens by which we view our evolving galaxy and connect these properties to the universe as a whole.

The IMAP mission was identified as the top new mission priority in the National Academy of Science's 2013 Solar and Space Physics (Heliophysics) Decadal Survey: "So-



**Table 1** The Ten Instruments in the IMAP Payload (imaging instruments shaded)

Solar Wind and Pickup Ion Instrument
Combined Dual Ion Composition Experiment
High energy Ion Telescope
Solar Wind Electron instrument
Magnetic Field instrument
Low Energy ENAs and Neutrals
High Energy ENAs
Ultra-high Energy ENAs
Interstellar Dust Experiment
Ly-α Helioglow photometer

lar and Space Physics: A Science for a Technological Society" (National Research Council 2013). That community consensus document drew together two different white paper inputs from the over 180 white papers submitted for consideration. The first was a white paper that called for expanded energetic neutral atom (ENA) observations following on from the NASA Small Explorer IBEX (Interstellar Boundary Explorer) mission (McComas et al. 2009a) in addition to other observations, such as interstellar dust. IBEX launched into Earth orbit in 2008, made many seminal discoveries and firsts (e.g., McComas et al. 2009b, 2017), and is still taking groundbreaking observations and making new discoveries, as it continues to work perfectly after over a decade and a half in space (McComas et al. 2024). The second white paper called for detailed in-situ observations of the solar wind and energetic particles to better understand particle acceleration.

Both white papers that led to IMAP called for an observatory in orbit around the Sun-Earth L1 Lagrange point and as it turns out, their science was not just complementary, but synergistic, as some of the particles accelerated in the inner heliosphere are ultimately "recycled" through charge exchange in the outer heliosphere and return to L1 as ENAs. The Decadal Survey group recommended that NASA request proposals for the combined IMAP mission, as a PI-led mission in NASA's Solar Terrestrial Probes (STP) line. In 2017, NASA issued this Announcement of Opportunity (AO) as STP-5 and on 1 June 2018, they announced their selection of our team.

Our proposal was organized around the four Science Objectives specified in the IMAP AO. These were published by McComas et al. (2018b) and are quoted here (italics, listed from the LISM inward):

- improve understanding of the composition and properties of the local interstellar medium (LISM),
- 2) advance understanding of the temporal and spatial evolution of the boundary region in which the solar wind and the interstellar medium interact,
- identify and advance the understanding of processes related to the interactions of the magnetic field of the Sun and the LISM, and
- 4) identify and advance understanding of particle injection and acceleration processes near the Sun, in the heliosphere and heliosheath.

To address these Objectives, the IMAP team proposed a set of ten unique science instruments (Table 1 and Fig. 2), three of them with two sensor heads each, and one on its own dedicated pivot platform. Our extensive observations span from in-situ measurements of the interplanetary magnetic field, solar wind electrons, and ions from solar wind (SW) energies up through suprathermal ions (STs), pickup ions (PUIs) and energetic particles (EPs); these



100 Page 4 of 82 D.J. McComas et al.



**Fig. 2** The IMAP instrument suite. The top five instruments make in-situ observations of ions, electrons, and magnetic fields and provide continuous real-time space weather (I-ALiRT, red box) data in addition to subsequently telemetering complete science data. The three ENA cameras (lower left) have overlapping energy ranges that roughly match in-situ ion measurements above. Finally, IMAP directly measures interstellar dust, and the UV glow modulated by the 3-D solar wind structure

are accompanied by global imaging of the 3-D solar wind structure using the Ly- $\alpha$  backscatter helioglow. For the outer heliosphere, we make precise observations of interstellar neutral (ISN) atoms and interstellar dust (ISD) that enter the heliosphere, as well as remote observations of the plasma and energetic ions in the heliosheath and in the VLISM, via global observations of ENAs, which are produced in these regions. Collectively, these instruments produce a complete and synergistic set of observations, which directly address IMAP's coupled Objectives of understanding particle acceleration and the global heliospheric interaction.

Our ground testing program included direct cross-calibration of pairs of IMAP instruments prior to launch to ensure continuous well-calibrated observations of ions and ENAs across IMAP's various instrument energy ranges. In particular, the pairs: SWAPI & CoDICE, IMAP-Lo & IMAP-Hi, and IMAP-Hi & IMAP-Ultra were cross calibrated as separate pairs in the same vacuum chamber at the same time and rotated back and forth into various steady ion and neutral beams over their overlapping energy and species ranges.

Beyond ground-based cross calibration, instruments with overlapping energy and species ranges, and even shared look directions at different phases of IMAP's spin, will be further cross calibrated by comparing observations in space. In addition, IMAP-Lo and IMAP-Hi will be cross-calibrated with IBEX-Lo and IBEX-Hi for as long as the IBEX mission survives. This crucial set of combined measurements provides a continuous multi-decadal IBEX/IMAP data set, which will be critical to observe and quantify the global outer heliospheric ENAs over time and produce the needed "four dimensional" understanding of our heliosphere (3-D spatial and temporal evolution).

Because of the integrative science that IMAP is designed to do, all IMAP instrument data are processed through a single combined Science Operations Center (SOC), which autonomously processes Level 0-3 science data for the entire payload. Furthermore, we also have developed a Combined Analysis, Visualization, and Access (CAVA) data analysis software suite that allows the IMAP science team access and seamlessly integrates data from any subset of the ten instruments. These two unique features of IMAP avoid the common problems associated with individual instrument teams producing separate, asynchronous data sets that subsequently need to be combined. A single unified SOC and CAVA are two



critical innovations for the mission to fully enable the sorts of system science that IMAP is designed to do.

IMAP's 10 instruments are mounted onto the spacecraft bus, which was designed with an "open bay" geometry that allowed instruments to be integrated and de-integrated in any order as needed by the individual instrument development schedules. The IMAP spacecraft subsystems have high heritage, with most being derived from the Parker Solar Probe (PSP) mission (Fox et al. 2016), with needed modifications for IMAP. As of this writing, PSP has been functioning well in space (in a much harsher environment than that at L1) for over six years and continues to do so.

IMAP launched on a Falcon 9 rocket at 07:30:50 EDT on September 24, 2025 from Launch Complex 39A at NASA's Kennedy Space Center. The rocket also carried secondary payloads of 1) NOAA's Space Weather Follow On (SWFO-L1) mission and 2) NASA's Carruthers mission, named after the late physicist George R. Carruthers, which observes the geocorona in UV light. It takes about four months for IMAP to get to the Sun-Earth L1 point, over which time the spacecraft and instruments are all turned on, tuned, and fully commissioned. After inserting into orbit around L1, IMAP enters Phase E and begins routinely sending back both continuous real-time space weather observations and our mission science data.

The IMAP spacecraft is a simple Sun-pointed spinner, which, like IBEX, rotates at four Revolutions Per Minute (RPM). Unlike IBEX, the spin axis is repointed roughly  $1^{\circ}$  each day to keep it pointed in a direction parallel to the nominal solar wind aberration angle ( $\sim$ 4° to the right of the Sun in the ecliptic plane, when viewed from the spacecraft). This close tracking of the average solar wind direction, along with being far away from terrestrial-related backgrounds that dominated IBEX noise sources, means that IMAP produces far better and cleaner ENA measurements as well as continuously observing the solar wind, pickup ions, energetic particles, and the IMF. The IMAP spacecraft and instruments are designed to operate far longer than the two-year nominal mission and the spacecraft includes consumables (e.g., hydrazine) to operate for at least five years, even for a highly off-nominal launch. Given anything close to the nominal launch performance, IMAP should have hydrazine for orbit maintenance and daily repointing for many decades.

The IMAP mission carries out critical space weather research and provides key real-time space weather observations and associated operations (e.g., Baker 2002 and references therein) that will revolutionize magnetospheric forecasting (Posner 2007). In particular, the IMAP Active Link for Real-Time (I-ALiRT; Lee et al. 2025) continuously telemeters real-time space weather data taken by SWAPI, CoDICE, HIT, SWE, and MAG (red box in Fig. 2). The IMAP SOC analyzes and posts these real-time data with a latency of <5 minutes. Thus, IMAP provides critical inputs for magnetospheric models and operational space weather prediction tools. The improved cadence and novel measurements (e.g., charge-state ratios, solar wind electron data, and high-energy electron fluxes) compared to the Advanced Composition Explorer (ACE; Stone et al. 1998) enhances the accuracy of predicting geomagnetic indices (e.g., Dst, Kp) and auroral activity, enabling better mitigation of space weather impacts on technological infrastructure (Pulkinnen et al. 2013).

The IMAP team published much of our original science proposal in a Space Science Reviews article, as a description of the IMAP mission as we originally proposed in 2017 (McComas et al. 2018b). The IMAP mission has been continuously under development since selection in 2018 and has just launched at the time of this writing. This current paper and companion papers document the actual IMAP mission and its capabilities after development, assembly and integration, at the time of launch. The IMAP mission we are flying fully meets the original requirements laid out in our accepted proposal (McComas et al. 2018b), and in



100 Page 6 of 82 D.J. McComas et al.

many cases, goes well beyond those to offer even greater capabilities and science data to the entire science community.

In addition to this mission overview paper, this IMAP mission collection comprises 17 papers and also contains papers on the overall observatory (Hegarty et al. 2025); mission and science operations (Reno et al. 2025); three papers giving scientific background for IMAP from our three science theme teams: Acceleration and the broader context of the solar wind and space weather (Cohen et al. 2025), Outer heliosphere through ENAs (Reisenfeld et al. 2025), and Samples of interstellar material (Szalay et al. 2025); individual papers documenting each of the ten science instruments on IMAP: SWAPI (Rankin et al. 2025), CoDICE (Livi et al. 2025), HIT (Christian et al. 2025), SWE (Skoug et al. 2025), MAG (Horbury et al. 2025), IMAP-Lo (Schwadron et al. 2025), IMAP-Hi (Funsten et al. 2025), IMAP-Ultra (Gkioulidou et al. 2025), IDEX (Horányi et al. 2025), and GLOWS (Bzowski et al. 2025); and finally a paper on our IMAP I-ALiRT space weather data system (Lee et al. 2025).

This paper is organized as follows. Section 2 describes IMAP Science, which leads into a discussion of IMAP as a Unified Space Physics Observatory (Sect. 3) and IMAP Instruments and Measurements (Sect. 4). In Sect. 5 we summarize the Spacecraft and Mission Design and our Operations, Data, CAVA, and Real-Time Space Weather in Sect. 6. In addition, this paper includes the Appendix, which provides a mission-level definition of select technical terminology and a list of acronyms used throughout this paper and collection. Finally, the current state of our Calibration and Measurement Algorithms Document (CMAD) is provided as a supplemental file to this paper and thus, this paper also serves as the citable reference for the CMAD, even though the online version will evolve and grow over the mission's science operational lifetime.

Finally, this paper acts as the citable reference for the overall IMAP mission and, along with the other papers in this collection, documents the complete IMAP mission at the time of launch.

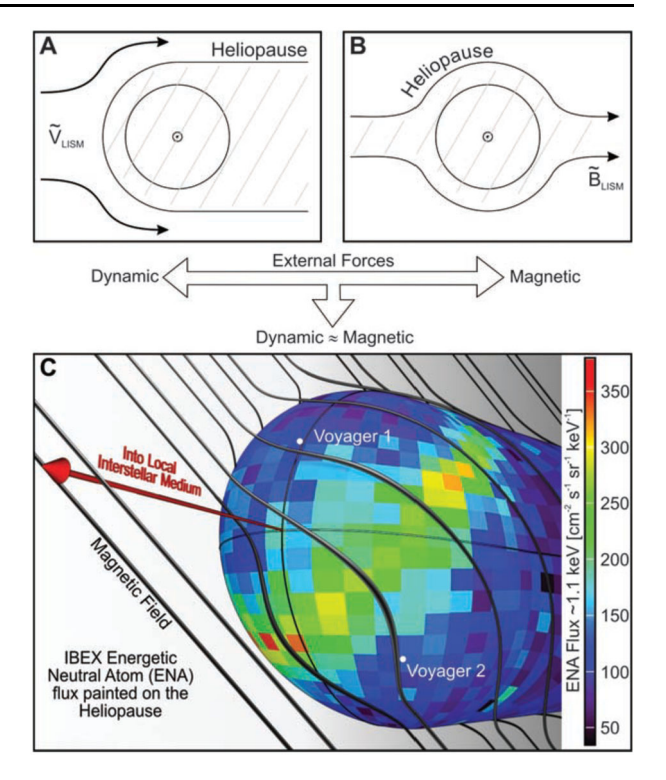
#### 2 IMAP Science

The Sun's hot corona is constantly expanding outward into space in all directions to form a solar wind of ionized plasma. This time-varying, supersonic solar wind picks up locally ionized interstellar neutrals drifting into the heliosphere, creating the PUI population, interacts with the planets in a variety of ways, creates space weather here at Earth, and ultimately fills our heliosphere and defines its boundaries through the interaction with the surrounding plasma and gas of the VLISM. Parker's (1961) classic paper defined the two extreme cases for astrospheres, such as our own heliosphere: 1) one which was dominated by the relative motion of the star and sits surrounding interstellar medium, where the dynamic (ram) pressure of the plasma forces the astro/heliosphere into a "bullet" shaped object with an astro/heliotail stretching back in the downwind direction (Fig. 3A), and 2) another interaction dominated by a very strong interstellar magnetic field with a roughly spherical astro/heliosphere, centered on the Sun, and escape of the solar wind into the interstellar medium as "drainage plumes" along the VLISM magnetic field (Fig. 3B). IBEX discovered that our own heliosphere's interaction is far more complex and interesting than either of these extremes, being intermediate between them (McComas et al. 2009b; Fig. 3C).

The PUI-laden solar wind and embedded IMF are compressed across the termination shock and produce a flow that is far more turbulent in the heliosheath – the region beyond the termination shock but inside the heliopause, which separates heliospheric plasma from



Fig. 3 Schematic diagrams of Parker's (1961) extreme cases of possible astrosphere configurations (top) and the intermediate configuration of our own heliosphere as discovered by IBEX. Figure taken from McComas et al. (2009b)



the VLISM. The compressed and turbulent heliosheath acts to deflect the vast majority of galactic cosmic ray (GCR) particle radiation around the heliosphere (Zank and Frisch 1999; Scherer et al. 2002; Schwadron et al. 2011). This deflection helps protect our solar system's neighborhood in the galaxy. All life on Earth has developed and evolved within our protective heliospheric bubble. Understanding the heliosphere's critical interaction with the VLISM in detail is one of the primary pressing challenges in heliophysics today – a challenge that IMAP was designed to resolve.

The other pressing scientific problem that IMAP is designed to address is particle acceleration, which controls the distribution of energy from the core plasma population to the tails of the particle distributions where a small minority of particles carry significant portions of the total particle energy in the plasma. Similar processes to those taking place in the heliosphere are responsible for accelerating particles throughout the galaxy, and cosmos, ultimately forming the highest energy galactic cosmic rays observed in space. These galactic cosmic rays are largely formed from astrophysical shocks such as supernova remnant shocks.

Our heliosphere is controlled by physical processes and interactions involved in particle acceleration, and particle transport (Giacalone et al. 2022; Klein and Dalla 2017; Cohen et al. 2021), which ultimately play critical roles in shaping our interstellar boundaries, controlling the heliosphere's environment, and mediating the propagation of high energy particle populations external to our solar system, such as cosmic rays. Our heliosphere is a physical case study by which we understand similar processes active in other astrospheres, and the myriad astrophysical interactions at work throughout the galactic environment and cosmos.

These particle acceleration processes produce energetic particles that interact with planetary magnetospheres and atmospheres and may even have played an important role in form-



100 Page 8 of 82 D.J. McComas et al.

ing the building blocks of life (Todd 1994; Shaviv and Veizer 2003; Rhode and Muller 2005; Airapetian et al. 2016). At the same time, these energetic particles play a central role in space weather that adversely impacts our technological infrastructure and endangers astronauts in space (Schwadron et al. 2014a). The heliosphere provides the only place where space particle acceleration can be observed directly in situ.

In addition to discovering the intermediate (Parker) state of our heliosphere, the very first IBEX observations (McComas et al. 2009b; Schwadron et al. 2009; Funsten et al. 2009b; Fuselier et al. 2009b) showed the dominance of energized particles, as opposed to the original solar wind, producing ENAs in the heliosheath (Gruntman et al. 2001). Energized PUIs and other energetic particles dominate the pressure and interaction in the heliosheath both at IBEX energies up to 6 keV and likely at energies above that as suggested by Cassini/INCA (Krimigis et al. 2004, 2009). Thus, the dominant pressure provided by suprathermal and energetic particles arise from a significant amount of the solar wind dynamic energy being converted into particle acceleration (McComas et al. 2009b; Schwadron et al. 2009; Krimigis et al. 2009).

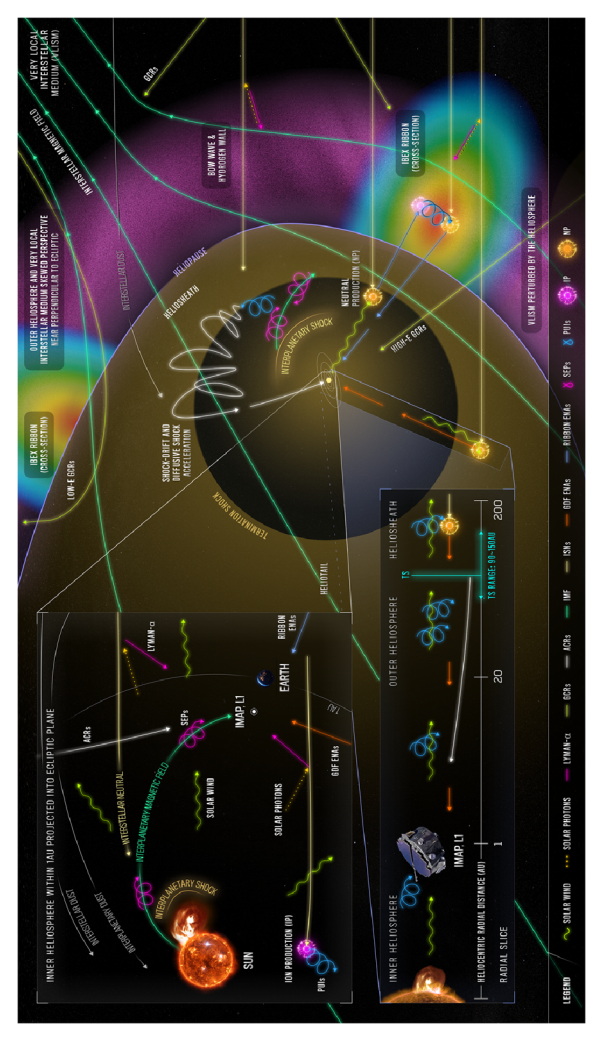
The linkage of large suprathermal populations to the global heliospheric interaction led to a new understanding of just how important particle acceleration is not just to our heliosphere, but to stellar and other astrophysical interactions throughout the cosmos. Thus, for larger astrophysical settings, one needs to scale-up the acceleration processes in our solar system, such as compressional waves and shocks driven by coronal mass ejections (CMEs), which accelerate solar energetic particles (SEPs). As McComas et al. (2018b) summarized: "The unified observations and analyses provided by the IMAP mission are crucial to understanding the inextricable link between the origins of particle acceleration and the global interactions of our heliosphere with the VLISM."

We have learned so much more about the heliosphere in the more than 15 years after the initial IBEX results, and of course, the real heliosphere is far more complicated than the simple schematic diagrams shown in Fig. 3. In Fig. 4 we attempt to capture core elements of the complexity of our heliosphere's interaction with the VLISM as we understand it today. This figure is also used as a starting point for expanded diagrams in each of the three Science Theme papers (Cohen et al. 2025; Reisenfeld et al. 2025; Szalay et al. 2025), completing a set of four interrelated diagrams for summarizing the IMAP science.

NASA's assessment of the strategic importance of the IMAP mission is shown in Table 2, which is taken from our IMAP Level 1 Requirements Document. This shows that IMAP is a major contributor to three of the four key science goals outlined in the Heliophysics Decadal Survey *Solar and Space Physics: A Science for a Technological Society* (National Research Council 2013), which can be traced back to the three overarching science goals for NASA's Heliophysics Division outlined in NASA's 2014 Science Plan (NASA 2014).

The next three subsections summarize the three overarching science themes of the IMAP mission: acceleration and the broader context of the solar wind and space weather (2.1), exploring the outer heliosphere through ENAs (2.2), and samples of interstellar material (2.3). For each of these themes we assembled a "Theme Team" comprised of IMAP scientists to focus scientific planning and discussions through the development phase of the mission and to help the mission science leadership in organizing research in these areas during the science phase of the mission. Finally, Papers 4–6 of this IMAP collection (Cohen et al. 2025; Reisenfeld et al. 2025; Szalay et al. 2025, respectively) provide much more detailed descriptions of the science themes.





beliosphere. The solar wind flows radially outward, incorporating an increasing fraction of PUIs and PUI pressure all the way out to the termination shock, after which it gets from the Sun into the heliosheath. The inset in the upper-left shows a zoom in on processes and populations in the inner heliosphere, around and sunward of where IMAP is rame, producing a bow wave and hydrogen wall. The IBEX ribbon ENAs are generated outside the heliopause through one of a number of secondary ENA sources. The bulk of he non-ribbon, globally distributed flux (GDF) of ENAs is generated in the heliosheath (lower inset), where turbulent flows help deflect dangerous GCRs away from the inner swept back toward the heliotail. Particle acceleration occurs all the way from the Sun, through various processes in the solar wind (upper inset), out to the termination shock ydrogen wall and interstellar bow wave ahead of the heliosphere in its upstream direction. The inset in the bottom-left shows a heliocentric radial slice, along a log-spaced axis ig. 4 An attempt at an "all-encompassing" schematic diagram of the large scale heliospheric interaction. The VLISM flows in from the right side of the figure in the solar and beyond. Here, different particle populations and physical processes are marked with different colors, line-types, and symbols, as defined in the legend along the bottom of the graphic. The solar wind density and its rough variation in heliocentric distance both inside and outside of the termination shock are indicated with the yellow shading in the nain portion of the graphic. Cross-sections of the  $\sim 1$  keV ENA intensity of the IBEX "Ribbon" are shown just outside of the heliopause, while the magenta haze indicates the ocated near 1 au



100 Page 10 of 82 D.J. McComas et al.

Table 2 Major and Supporting Contributions of the IMAP Mission

Science mission directorate goal	Decadal survey goal	IMAP objective
SMD 2) Advance our understanding of the connections that link the Sun, the Earth,	DS-3) Determine the interactions of the Sun with the solar system and the	O1) Improve understanding of the composition and properties of the local interstellar medium
planetary space environments, and the outer reaches of our solar system	interstellar medium	O2) Advance understanding of the temporal and spatial evolution of the boundary region in which the solar wind and the interstellar medium interact
		O3) Identify and advance understanding of processes related to the interactions of the magnetic field of the Sun and the local interstellar medium.
SMD 3) Develop the knowledge and capability to predict extreme conditions in space to protect life and society and to safeguard human and robotic explorers beyond Earth	DS-1) Determine the origins of the Sun's activity and predict the variations in the space environment	O4) Identify and advance understanding of particle injection and acceleration processes near the Sun, in the heliosphere and heliosheath.
SMD 1) Explore the physical processes in the space environment from the Sun to the Earth and throughout the solar system	DS-4) Discover and characterize the fundamental processes that occur both within the heliosphere and throughout the universe	

#### 2.1 Acceleration and the Broader Context of the Solar Wind and Space Weather

IMAP provides a unique opportunity to connect in-situ measurements with remote sensing observations from the same spacecraft. Such coupling between the remote solar observations and in-situ measurements have transformed our understanding of solar wind acceleration and structures; solar energetic particle acceleration and transport; and space weather impacts in the inner heliosphere (see Fig. 4). With IMAP, similar holistic views are obtained for the outer heliosphere to significantly advance our understanding of the global heliosphere, its interactions with the interstellar medium and the impact of variable solar activity.

IMAP measures the key related entities of interstellar neutral atoms and their secondary components, PUIs, anomalous cosmic rays (ACRs), and ENAs. In particular, PUIs that have been created from ionization of interstellar neutral atoms and carried outward by the solar wind are accelerated in the vicinity of the termination shock to produce ACRs, some of which then transit back into the inner heliosphere (see e.g., Axford et al. 1977; Krymsky 1977; Bell 1978; Blandford and Ostriker 1978; Armstrong et al. 1985; Jokipii 1986; Klecker 1995; Giacalone et al. 2022). The PUIs also interact with interstellar neutrals to generate the ENAs resulting in the observed GDF and IBEX ribbon populations (e.g., Zank et al. 2010; Zirnstein et al. 2014; Zank 2015; McComas et al. 2009c; Heerikhuisen et al. 2010). Secondary ISN components, created by charge exchange between pristine ISN atoms and the perturbed interstellar plasma flowing around the heliopause (Baranov and Malama 1993), provide information about the plasma state in front of the heliopause and its deformation due to the interstellar magnetic field (Bzowski et al. 2019). Detailed in-situ measurements of the PUIs at 1 au for a variety of solar wind conditions and under the influence of different



solar wind structures elucidate their formation and evolution. Combining these observations with in-situ observations of ACRs and their characteristics, tests and constrains models of the acceleration mechanisms at the termination shock and the subsequent transport through the heliosphere. Detailed ENA maps as a function of time and energy, in conjunction with the PUI observations, advance our understanding of the conditions and variability of the heliospheath, the VLISM and the acceleration processes involved.

In studying these relationships, IMAP is poised to make significant advances in understanding several aspects of fundamental acceleration and transport of particles throughout the heliosphere. Given the critical role that PUIs play in both the ACR and ENA generation in the outer heliosphere, significant attention is focused on studies of PUIs locally at IMAP. Interplanetary shocks are fairly common at 1 au and are well characterized by the in-situ plasma and fields measurements onboard. The heating and acceleration of PUIs at interplanetary shocks is studied for a variety of shock characteristics, some of which may prove to be reasonable analogs for the termination shock and its local conditions. These studies advance our understanding and lead to significant improvements in the modeling of the termination shock physics and PUI interactions, to resolve, for example, the current differences in the IBEX ENA observed flux and the expected values obtained from current models (Gkioulidou et al. 2022).

Current ENA models also assume a coupling between the PUIs and solar wind, such that the PUIs are expected to have the same bulk velocity as the solar wind (although PUIs have quite different density and pressure). However, it is possible that this is a poor assumption and PUIs may be as a less coupled population, which could have significant impacts on modeling results. Through complementary high time resolution and full 3D velocity measurements of the PUIs, made under a variety of solar wind conditions, IMAP studies this question of coupling in detail and provides critical information for modeling of the ENA production in the outer heliosphere and from that, interpretations of the IMAP GDF ENA observations. Similarly, the PUIs respond to local magnetic field fluctuations, both at or near shocks and in other solar wind structures, inform the transport of PUIs in the heliosheath and how PUI populations may interact with the LISM magnetic field. The application of emerging understanding of PUI interactions and transport from IMAP 3D velocity space measurements and high time resolution measurements constrains models attempting to explain the origin of the ENA ribbon.

PUIs are only one constituent of the suprathermal charged particle population observed at 1 au. The suprathermal tail appears to be ubiquitous, however the potential contributors to the population are, in some cases, extremely variable (Gosling et al. 1981; Tan et al. 1989; Tsurutani and Lin 1985; Chotoo et al. 2000; Desai et al. 2001, 2003, 2006; Kucharek et al. 2003; Allegrini et al. 2008). In particular, the contribution from particles associated with solar activity and transients, such as interplanetary shocks, vary not only on short timescales but also on longer, solar cycle, timescales. The short-term variability of the suprathermal population apparent at 1 au is not likely to survive out to the outer heliosphere, however the longer-term variability may be evident in the observed ENA maps when examined as a function of the phase of the solar cycle.

Large scale structure of the solar wind itself has also been connected to changes in the IBEX ENA observations (McComas et al. 2018a). While individual solar wind transients such as CMEs are generally eroded as they traverse the heliosphere, different streams and structures can combine to become global merged interaction regions (GMIRs) that can result in pressure enhancements impacting the heliosheath and even inciting waves and shocks in the surrounding VLISM. IMAP measures the latitudinal structure of the solar wind (Bzowski et al. 2025), makes detailed measurements of the transients at 1 au and examines the statistical distribution of the solar wind parameters to inform modeling of the large-scale variability



of the solar wind and its ultimate impact on the generated ENA populations reflected in the IMAP remote sensing observations. IMAP has substantially better time resolution both in the ENA maps compared to IBEX, and in the global solar wind structure, enabling more detailed studies of the ENA variability and its connection to solar wind changes (McComas et al. 2020). Additionally, the models used to propagate these solar wind disturbances out to the termination shock and beyond have dramatically improved since the early IBEX observations. In this context, the velocity and density of the solar wind inferred from IMAP measurements of the Ly-a helioglow provide another path to understanding the large-scale structure of the solar wind. The helioglow-based 3D solar-wind structure is complementary to IMAP in-situ measurements in the ecliptic plane.

Many studies have shown that particles and waves can affect interplanetary shock structures and play a significant role in the energy budget (see, e.g., Trotta et al. 2021). While this has been studied with past in-situ data, with IMAP these observations can be examined with an eye towards the applicability for the termination shock and ultimately the generation of ACRs and ENAs. As with the PUI-shock studies, the variety of shocks measured by IMAP likely contain a subset that can be viewed as analogs for the termination shock. The broad, continuous energy coverage of particle measurements made by IMAP provides unparalleled opportunities to examine the interplay between the particle distribution, solar wind turbulence and the shock characteristics in situ. Furthermore, the combination of PUI and ACR data with high energy ENA observations better informs the nature of PUI acceleration to ACRs at the termination shock, and more broadly at astrophysical shocks on even much larger spatial scales.

Naturally, in addition to the unique combination of the in-situ and remote sensing measurements on IMAP, the particle and fields observations at 1 au make significant contributions to inner heliospheric science and space weather research and operations. IMAP joins the robust Heliophysics Systems Observatory (HSO) and overlaps with several long-term spacecraft located at L1, including ACE and Wind. This overlap provides the opportunity to intercalibrate spacecraft measurements such that the already decades-long, L1 plasma and fields database can be reliably extended into the future with IMAP observations. Such a database has proved critical for studying solar-cycle time dependences and for making the connection between 1 au solar wind and PUI characteristics with the ENA emissions from the outer heliosphere. This combination of L1 spacecraft also offers a singular opportunity for multi-point observations of solar wind and IMF structures on spatial scales of 5–200 Earth radii (Eastwood et al. 2017). These measurements resolve small-scale variations in solar wind turbulence and magnetic field topology that influence magnetospheric reconnection and particle energization.

Furthermore, IMAP's high-cadence measurements and real-time data significantly advance terrestrial magnetospheric physics by providing critical upstream boundary conditions for studying solar wind-magnetosphere coupling, geomagnetic storms, and radiation belt dynamics. Solar wind structures such as CMEs, CIRs, and interplanetary shocks are primary drivers of magnetospheric compression, reconnection, and particle injection, which trigger geomagnetic storms and substorms (Gosling 1993; Tsurutani et al. 2006). IMAP's particle and fields measurements provide unprecedented characterization of these structures from the critical L1 point upstream of the Earth's magnetosphere. Suprathermal ions, including PUIs, serve as seed populations for acceleration at interplanetary shocks and within the magnetosphere, contributing to the ring current and radiation belts. These data and their related high energy SEP component support studies of particle transport, acceleration, and loss in the magnetosphere, particularly during geomagnetic storms when wave-particle interactions are prevalent (e.g., Baker and Kanekal 2008; Reeves et al. 2011). The resulting scientific



advances deepen our knowledge of fundamental magnetospheric processes, complementing IMAP's primary objectives in heliospheric and interstellar science.

#### 2.2 Exploring the Outer Heliosphere Through ENAs

IMAP seeks to develop and execute an integrated observation and theory and modeling campaign to understand the nature of the heliosheath and VLISM, and how the two interact. The Outer Heliosphere through ENAs Science Theme is organized around four topical areas: i) the physics of the heliosheath and VLISM, ii) the global structure of the heliosphere, iii) the nature of the IBEX ribbon, and iv) possible observation of helium and other heavy ions. The greatly improved observational capabilities of the IMAP ENA imagers over their predecessors enable IMAP to not only address outstanding issues remaining from previous studies but also make new discoveries beyond what we can currently imagine.

#### 2.2.1 Physics of the Heliosheath and VLISM

This topic is concerned with the physical processes occurring within the heliosheath and VLISM, and how they are controlled by internal and external forces. We have limited knowledge of the heliosheath energy distribution, especially below 100 eV and above 6 keV, leaving open questions regarding the nature of the heliosheath thermodynamic state, such as how heliosheath plasma is energized by the solar wind and PUI distributions, and how plasma flows are affected by both the outbound solar wind and external compression by the VLISM. Additionally, major discrepancies persist between observed and modeled ENA fluxes, especially in the energies below 0.7 keV (Galli et al. 2023) and above 6 keV (e.g., Gkioulidou et al. 2022; Kornbleuth et al. 2023; Galli et al. 2023), demonstrating significant gaps in our understanding of heliosheath processes. IMAP provides measurements of the ENA distribution from 0.1 keV eV to over 100 keV and spatial resolution across the entire sky. IMAP also measures latitudinal profiles of solar wind at an unprecedented cadence of each Carrington rotation, providing source context for interpretation of heliosheath ENA variations. In addition to direct analysis, these measurements provide models with a comprehensive set of constraints that need to be matched. We have also learned that the VLISM plasma beyond the heliopause is another source of GDF ENAs, (Zirnstein et al. 2022) and although it is challenging to untangle the relative contributions from heliosheath and VLISM plasma, IMAP's improved capabilities enable studies of the plasma processes occurring in both regions.

One of the most important discoveries from IBEX is that the heliosheath is highly sensitive to solar wind conditions. This was dramatically demonstrated when a rapid increase of the solar wind dynamic pressure starting in late 2014 led to a strong increase in ENA flux, first observed in late 2016 south of the nose, and then progressively expanding to encompass more of the sky in the following years (McComas et al. 2018a, 2019; Zirnstein et al. 2018). It appears that a new solar wind pressure enhancement began in 2024, and we wait with anticipation to see if there is a corresponding ENA flux enhancement in the early IMAP science data. IMAP extends the catalog of consecutive 6-month ENA maps started in 2009 by IBEX across multiple solar cycles (e.g., McComas et al. 2024 and references therein), allowing us to develop a deep understanding of how the heliosheath is governed by changes in solar conditions. One critical application of this research is the question of how the heliosheath attenuation of the GCR flux is affected by such variations (Manuel et al. 2015; Boschini et al. 2019).



100 Page 14 of 82 D.J. McComas et al.

#### 2.2.2 Global Structure of the Heliosphere

The shape of the heliosphere is mainly governed by the balance between the outward pressure of the solar wind and the inward pressure of the VLISM plasma and magnetic field. IBEX ENA observations have been used to empirically constrain the heliopause distance through use of the "sounding method" whereby time variations in the outgoing solar wind flow are correlated with variations in the return ENA signal, from which the distance can be inferred from the time delay (Reisenfeld et al. 2021; Zirnstein et al. 2022). In the nose direction, the sounding method results match the in-situ Voyager heliopause distances of  $\sim$ 120 au within uncertainties. The larger sensitivity of IMAP over IBEX allows us to apply the sounding method with improved accuracy. Moreover, extending the ENA map catalog to multiple decades makes it possible to detect changes in the size and boundary of the heliosphere as it "breathes" over the solar cycle.

Notably, few ENAs in the IBEX energy range are formed beyond  $\sim 350$  au in the tailward direction, which limits the ability of the sounding method to find the heliopause in this direction. This is a consequential limitation because the extent of the heliotail is debated, with competing heliosphere models predicting a heliopause distance from as little as 300 au (e.g. Dialynas et al. 2017; Opher et al. 2020) to as much as 20,000 au. (e.g., Zank et al. 2010; Pogorelov et al. 2017; Izmodenov and Alexashov 2020). Depending on the flux levels, IMAP's extended energy range allows the heliotail to be probed to larger distances because the ENA production distance extends farther at higher energies (Kornbleuth et al. 2023).

The solar wind spatial distribution of slow and fast wind, varying over the solar cycle, is another important factor shaping the heliosphere. The Ly-a helioglow observed by IMAP is used to infer this three-dimensional structure of the solar wind velocity and density, which influences the heliospheric boundaries via modulation of PUI density and temperature in the heliospheath.

#### 2.2.3 Exploring the Nature of the IBEX Ribbon

The IBEX ribbon is a narrow, bright ENA feature that encircles the sky. The IBEX ribbon is observed by IBEX at energies from  $\sim 0.5-6$  keV, appearing in the sky where the look direction is roughly perpendicular to the orientation of the VLISM magnetic field as it drapes around the heliosphere (McComas et al. 2009b; Schwadron et al. 2009; Zirnstein et al. 2015). A consensus is growing that the ribbon source is located beyond the heliopause and is formed via a "secondary ENA" mechanism (e.g., McComas et al. 2024 and references therein); however, there are still outstanding questions related to the ribbon's origin to be addressed by IMAP. The improved sensitivity and higher angular resolution of IMAP's ENA imagers advances our understanding of the spatial and temporal variation within the ribbon, such as what governs the shape of the cross-sectional profile of the ribbon, variations in the width of the profile as a function of position along the ribbon, and the time- and energy-dependence of the ribbon's center. IMAP's angular resolution, and the  $\sim 3$ -month observation cadence at low latitudes allows us to observe small-scale structures and temporal fluctuations within the ribbon, predicted to occur by VLISM turbulence models (Giacalone and Jokipii 2015; Zirnstein et al. 2020).

With the extension of GDF observations to lower and higher energies with greatly improved sensitivity and energy resolution, IMAP also discovers how low and high in energy the ribbon spans. IBEX-Lo observed the ribbon down to  $\sim$ 0.4 keV, but it is unclear if it extends further (McComas et al. 2014; Galli et al. 2014). IMAP's improved sensitivity to low energy ENAs lets us determine how low in energy the ribbon extends. At high energy, the



ribbon appears to become a broader structure at IBEX-Hi's highest energy passband, perhaps transforming into the "belt" enhancement observed by the INCA instrument on board Cassini (Krimigis et al. 2004, 2009; Dialynas et al. 2013; Westlake et al. 2020) With the combination of the extended IMAP-Hi energy range to 15 keV and the IMAP-Ultra energy range starting at  $\sim$ 5 keV, we fully characterize the evolution of the ribbon to higher energies and determine whether the belt is a continuation of the ribbon as a VLISM structure, or something else.

#### 2.2.4 Helium and Heavier ENAs

The observation of ENAs for elements heavier than hydrogen is particularly challenging due to their lower solar abundance and the lower detection sensitivity of ENA imagers for these species (Grzedzielski et al. 2013; Swaczyna and Bzowski 2017). However, the IMAP-Hi instrument has sufficient sensitivity to at least look for heavy ENAs. Here, we distinguish heavy ENAs, which originate from the heliosheath or ribbon, from interstellar neutrals, which are a beamed population that IMAP-Lo is optimized to detect. The number of expected heavy ENA detections is orders of magnitudes lower than hydrogen ENAs (Swaczyna and Bzowski 2017). Nevertheless, by integrating data over large regions of the sky, it may be possible to gather enough statistics to identify a meaningful signal, particularly in the case of helium ENAs. If this is possible, the detection of heavy ENAs contributes to the study of VLISM composition (Grzedzielski et al. 2010; Swaczyna et al. 2014, 2022a,b). Spatial variations in heavy ENA populations may provide further insights into the structure of the heliosphere (Grzedzielski et al. 2013; Swaczyna et al. 2017). Finally, because helium ENA formation extends to much larger distances in the heliotail than hydrogen ENAs, their observation could also be a useful tool for studying the distant heliotail (Swaczyna and Bzowski 2017).

The above discussion of ENA topics is the tip of the iceberg regarding what can be learned from the rich ENA data sets that IMAP provides. The comprehensive instrument suite of IMAP, providing both in-situ particle measurements and remote observations of the heliospheric boundary via ENAs, offers opportunities for studies that cut across the science themes, such as the precise tracking of solar wind structures outward to the heliospheric boundaries and their effect on the heliosheath and the ribbon.

#### 2.3 Samples of Interstellar Material

The "samples of interstellar material" theme focuses primarily on IMAP Objective O1, i.e. "Improve understanding of the composition and properties of the local interstellar medium" (McComas et al. 2018b, and above), and focuses on the key scientific opportunities for IMAP associated with directly sampling the interstellar and interplanetary material at  $\sim$ 1 au. This area is organized into three broad scientific questions that directly relate to IMAP's Science Objectives: 1) What is the state of the pristine upstream LISM and how does it relate to its origins and evolution? 2) How does the VLISM interact with the heliosphere? 3) How does interstellar material, as well as interplanetary dust, affect the near-Sun environment?

## 2.3.1 What Is the State of the Pristine Upstream LISM and How Does It Relate to Its Origins and Evolution?

The composition of the pristine LISM provides key information about the evolution of matter in our galaxy from the Big Bang to today. Big Bang Nucleosynthesis set the element



and isotope composition of all matter in the universe at its beginning, with only H, D, and He isotopes, and some traces of Li as initial conditions (Coc and Vangioni 2017; Copi et al. 1995), whose abundances can be tied to the baryon density of the universe. Solar system abundances were frozen in the state of matter in our galaxy at the birth of the Sun about 4.6 billion years ago. They are derived from photospheric observations and meteoritic samples (Asplund et al. 2021; Lodders 2010). The LISM, with its neutral gas and dust, features the composition of galactic matter in our immediate neighborhood at the present time, after processing by a series of supernova explosions ~14 million years ago (Zucker et al. 2022).

These three points in time provide important constraints on evolution of matter in the universe and, in particular, in our galaxy. While there has been significant progress in constraining the abundances in the early universe (Turner 2022) and determining a detailed account of solar system abundances, observational evidence of the abundances in our interstellar neighborhood is scant, except for light elements and their isotopes.

IMAP provides a uniquely equipped observatory to analyze the material from the VLISM that transits through our heliosphere. IMAP measures neutral atoms and dust grains originally from the VLISM. Szalay et al. (2025) outlines how IMAP measurements can improve our understanding of the upstream, pristine LISM. These observations allow better understanding of the initial formation conditions of our solar system and determine how the interstellar medium interacts with our heliosphere.

#### 2.3.2 How Does the VLISM Interact with the Heliosphere?

Our Sun and heliosphere move through the VLISM at a relative speed of  $\sim$ 25 km s<sup>-1</sup>. This flow pressure, along with the VLISM magnetic and particle pressures, confine the SW as it flows radially away from the Sun at supersonic speeds. Bulk plasma particles cannot cross the heliopause as they are normally tied to their respective field lines (solar and interstellar fields, respectively). The interstellar magnetic field drapes around the heliopause, distorting what would be an otherwise axially symmetric shape. However, this interaction is more complex than this idealized situation because magnetic reconnection can connect solar and interstellar fields at the boundary and because of the presence of neutral atoms in the solar wind and in the partially ionized interstellar medium. As they have no charge, neutral atoms readily cross the heliopause and exchange information both ways, creating a unique interaction that extends from hundreds to roughly  $\sim 1000$  au from the Sun in the upwind direction. Specifically, momentum exchange between the heliosphere and VLISM shapes this electromagnetic interaction. Throughout our heliosphere, interstellar neutrals and dust are filtered, processed and exist in different abundances (e.g., Gloeckler and Geiss 2001). Interaction between the perturbed interstellar plasma flowing past the heliopause and the unperturbed ISN gas creates secondary populations of neutral atoms that IMAP can measure and resolve from the primary (Bzowski et al. 2019). The way our heliosphere processes and filters this VLISM has many open questions, such as: How is VLISM filtered and processed by the heliosphere? How does the VLISM magnetic field drape over our heliosphere? How does the heliosphere affect the VLISM? IMAP is uniquely configured to investigate and resolve these key open questions.

### 2.3.3 How Does Interstellar Material, as Well as Interplanetary Dust, Affect the Near-Sun Environment?

This question circles back to the topics discussed in Sect. 2.1, which addresses the role of PUIs on the near-Sun environment. To investigate how interstellar material and interplanetary dust affect the near-Sun environment, we pose the following questions that IMAP



directly addresses: What is the relative abundance of interstellar PUIs compared to the inner source or any other solar system object-related sources? What is the composition of dust at 1 au that provides a seed population for the inner source PUIs? This third question exemplifies, once again, how IMAP's science themes are interconnected, as the direct in-situ measurements of the near-Sun plasma and dust environment allow us to significantly advance our understanding of the physics of the interstellar medium.

#### 3 IMAP as a Unified Space Physics Observatory

As described in McComas et al. (2018b), the IMAP instrument suite provides complete and coordinated observations that simultaneously enable three levels of study. These include *discovering* global properties of the interstellar interaction as a part of the coupled system with the origins of particle acceleration from IMAP. IMAP also enables *exploring* fundamental and global properties of the interstellar interactions and particle acceleration by combining IMAP observations with physics-based calculations, theory, and simple modeling. More deeply, IMAP enables in depth *understanding* of the interstellar interactions and origins of particle acceleration through interactive analyses that combine IMAP data in refining advanced models and simulations. At all three levels, our CAVA tool kit enables seamless and efficient examination across multiple instrument data sets to provide the team with truly integrated analysis and research capability from the start of the science phase of the mission.

Theory and modeling (T&M) are vital to IMAP's success by enabling discovery, exploration, and understanding. Therefore, the IMAP Science Team incorporated T&M Co-Is from the start, who have been specifically tasked "to ensure deep investigation of 1) the origins of particle acceleration in suprathermal populations, 2) the roles of turbulence in microphysical processes, and 3) kinetic interactions across scales in shocks, interaction and reconnection regions at 1 au, out through the solar wind and into the heliosheath".

Our approach to defining the observational requirements for the mission was directly driven by our four Science Objectives. This analysis led to five overarching observational drivers and additional required context measurements (italics, taken directly from McComas et al. 2018b):

- 1) High-sensitivity global heliospheric imaging;
- 2) ENA energy spectra covering core solar wind through EPs;
- 3) Neutral H, He, O, Ne, and D fluxes and flow direction as a function of time of year;
- 4) *High-time-resolution* (<1 min) *PUI*, *STs*, and energetic ion measurements;
- 5) Complete solar wind electron, proton, heavy ion, and magnetic field measurements to resolve solar wind structures, CMEs, shocks, and kinetic substructures.

Further, measurements of interstellar dust enable great additional discovery science, while maps of the UV helioglow inform the primary and secondary populations of ISN H, and the latitudinal structure of solar wind for supporting context.

Typical particle fluxes are shown in Fig. 5 of the in-situ ions (left) and ENAs (right) for various heliospheric ion and neutral populations. Some small fractions of the lower-energy ions are accelerated to higher energies. For example, pickup ions, with up to twice the local solar wind speed at pickup reach four times the local solar wind energy. Above that energy, a suprathermal ion tail often observed in the solar wind extends to even higher energies. Due to their high energies and speeds, these latter two types of ions are preferentially injected into particle acceleration (e.g., Giacalone et al. 1993) and provide many of the needed seed populations for EPs. The bottom sections of the two panels show the IMAP instrument



100 Page 18 of 82 D.J. McComas et al.

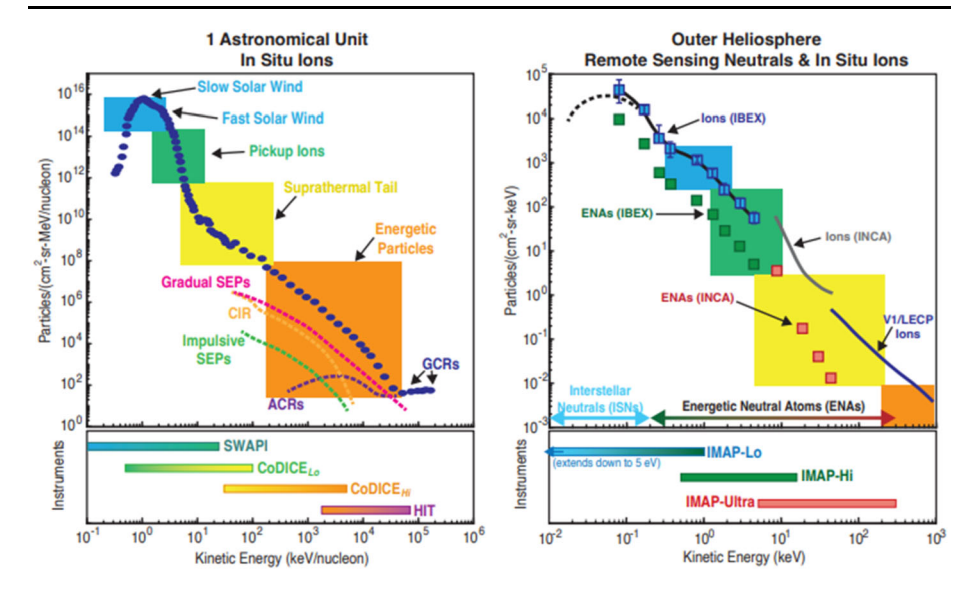


Fig. 5 Characteristic energy distributions of in-situ ions from the solar wind, pickup ions, suprathermal and energetic particles, and anomalous and galactic cosmic rays (left panel). Shown are 1 au oxygen fluences from ACE during a 3-year period, with representative particle spectra obtained for gradual and impulsive SEPs, CIRs, ACRs, and GCRs (adapted from Mewaldt et al. 2001). The overlapping energy ranges for the various IMAP ion instrument measurements are Indicated across the bottom. Right panel similarly shows characteristic energy distributions but for ENAs coming in from the heliosheath and VLISM; again, the bottom portion shows the overlapping energy ranges for the various IMAP ENA measurements, as well as for interstellar neutrals. Ion fluxes are from Voyager 1, along its particular trajectory and ENA observations are from Cassini and IBEX (Fuselier et al. 2012) for the same direction. Figure is adapted from McComas et al. (2018b)

coverage over various energy ranges. For ions, these cover six and a half decades and for ENAs, four and a half. Importantly, there is a good overlap in the energy ranges covered by these instruments and the overlaps were cross calibrated well against known beams in the laboratories before launch.

Part of IMAP's integrative science is to measure both the solar wind and energetic particles traveling from  $\sim 1$  au outward through the heliosphere and some of them then returning back as ENAs from the outer heliosphere. Therefore, colored boxes in Fig. 5 indicate roughly how the in-situ ions map from source ions into returning ENAs. Figure 6 provides estimates of transit times that it takes different IMAP observables at different characteristic energies to propagate outward from the inner heliosphere and inward from the outer heliosphere. The propagation times are plotted as a function of heliocentric distance.

In addition to the in-situ and remote (ENA) ion observations, IMAP carries other instruments to round out the mission as a complete heliophysics observatory. Figure 7 shows one example of each of the four sets of additional observations. From top to bottom, MAG measures the interplanetary magnetic field at low frequency, as well as solar wind magnetic turbulence at higher frequencies. IDEX observes dust travelling in from the interstellar medium, as well as dust from other planetary and solar system sources. GLOWS images the Ly- $\alpha$  backscatter glow from which 3-D structure of the solar wind is derived and infers the solar wind structure, enabling assessment of attenuation of ENA fluxes between their origin and detection sites and facilitating interpretation of compositional observations of ISN



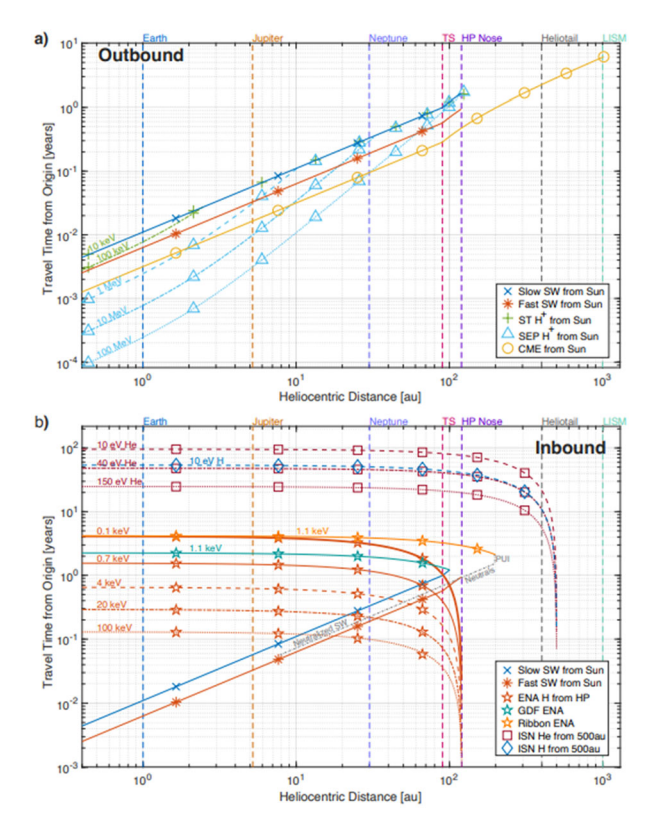
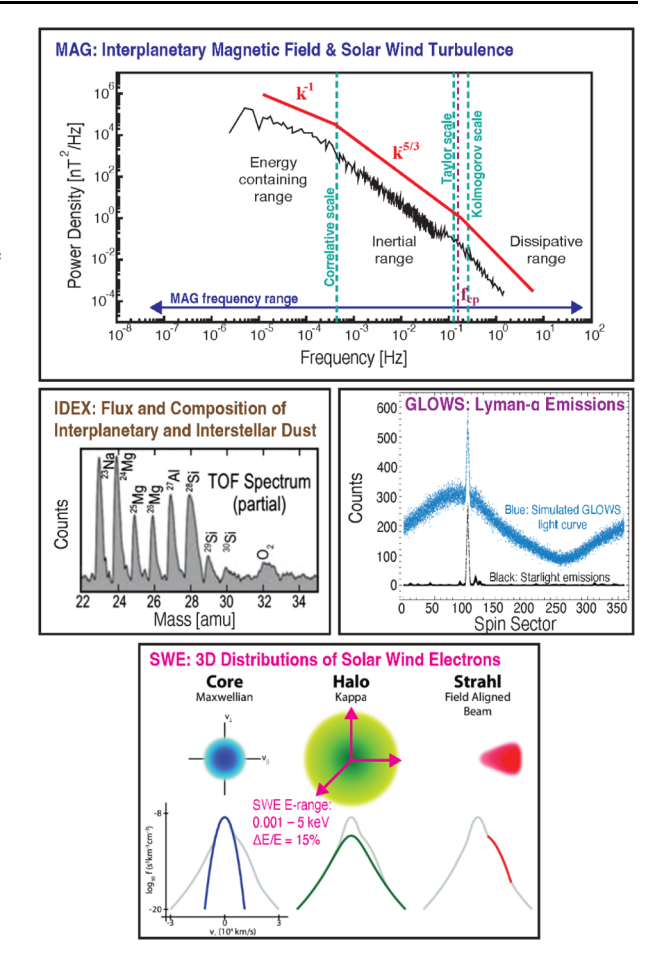


Fig. 6 Particle and plasma propagation times shown a) from the Sun outbound into the outer heliosphere and local interstellar medium and b) from the heliosheath and local interstellar medium inbound to the inner heliosphere and 1 au. For each particle species and population (shown with different colors and symbols, as indicated on the legends), travel times from origins (also indicated in the legends) are shown in years on a log10 scale. In both plots, representative distances for Earth-orbit (1 au), Jupiter-orbit (5.2 au), Neptuneorbit (30 au), termination shock (TS, 90 au), heliopause nose (120 au), mid-heliotail (400 au) and VLISM (1000 au) are shown with vertical dashed lines and labeled on the top of the axes. In panel a), slow solar wind (SW), fast SW, CMEs, and suprathermal (ST) and SEP protons (H+) are all shown originating from the Sun and traveling outward in heliocentric distance. Multiple energies are shown for the following populations: ST and SEP protons, ENAs, and ISNs. ST protons are shown for 10 and 100 keV; SEP protons are shown for 1, 10, and 100 MeV. Travel times for both ST protons and SEPs are calculated assuming that those particles travel along and perfectly parallel to idealized Parker spiral IMF moving at the slow solar wind speed (i.e., convecting outward) in the ecliptic plane. Note that this assumption represents an upper-bound on outward travel times; particularly for the highest energy SEPs, drift-diffusion through the heliosphere will result in shorter travel times than those shown here. For inbound populations in b), hydrogen ENAs are shown originating from the heliopause at 120 au and traveling inward to smaller heliocentric distances, while hydrogen and helium ISNs are shown originating from the LISM at 500 au and traveling inward. ENAs and ISNs are shown at: 0.1, 0.7, 4.0, 20, and 100 keV (ENAs), 10 eV (both ISN H and He), 40 and 150 eV (ISN He only). For all populations with multiple energies, the slowest to fastest are shown with thick, solid, dashed, dash-dot, and dotted lines. Also shown in b) are representations of the inner heliosphere sources and subsequent inbound ENAs from the GDF and IBEX ribbon populations. For GDF ENAs (example shown is a 1.1 keV hydrogen ENA), a source in the slow solar wind and neutralization in the heliosheath is indicated, with a total round-trip travel time of  $\sim$ 2.1 years. For the ribbon ENAs (also shown with a 1.1 keV hydrogen ENA), faster solar wind neutralizes in the inner heliosphere (gray dash-dot line), propagating out into the very local interstellar medium, around 200 au, where it is ionized (i.e., becomes an interstellar PUI) and then re-neutralized, returning to the inner heliosphere as a ribbon ENA over a total round-trip travel time of  $\sim$ 4.0 years



100 Page 20 of 82 D.J. McComas et al.

Fig. 7 Other instruments in the IMAP payload measure the interplanetary magnetic field and solar wind turbulence (MAG), interstellar (and other solar system) dust (IDEX), the solar wind Ly- $\alpha$  helioglow (GLOWS), and solar wind electrons (SWE). The MAG and SWE plots were adapted from Bruno and Carbone (2013) and Verscharen et al. (2019), respectively



atoms. Finally, SWE measures the 3-D solar wind electron distribution, including its core, halo, and Strahl populations.

#### 4 Instruments and Measurements

IMAP's ten instruments deliver comprehensive observations that span from in-situ measurement of particles, fields, and dust to remote imaging of the solar wind and its interaction with the VLISM at the very boundaries of our heliosphere. Table 3 shows the mapping of IMAP's four Scientific Objectives (Sect. 1) to our baseline science requirements, instruments, and description of the differences from Baseline to Threshold requirements. From our Level 1 Requirements Document, the Baseline Mission is defined by "the verifiable requirements to which the mission must be designed." In contrast, the Threshold Mission is defined as "the minimum requirements to which the mission must achieve prior to launch and still be deemed worth flying."

The sensitivities, resolutions, collecting powers, time cadences, and calibration have all been set to measure the key elements of our heliosphere and the energized particles in it.



 Table 3
 Mapping of the IMAP Scientific Objectives (listed above) to Required Instruments

IMAP scientific objective			Requirement name	IMAP instrument required	Difference between baseline science requirement and		
O1	O2	О3	O4			threshold science requirement	
X				NEUTRAL H AND D	IMAP-Lo	Reduced observation time and accuracy	
X				NEUTRAL He	IMAP-Lo	Reduced observation time	
X				NEUTRAL 0 AND Ne	IMAP-Lo	Reduced observation time and accuracy	
	X	X		ENA HI-RES SKYMAP	IMAP-Hi, IMAP-Ultra	Reduced observation time and sky coverage	
	X	X		ENA ENERGY SPECTRA	IMAP-Lo, MAP-Hi, IMAP-Ultra	Reduced observation time and sky coverage	
	X	X		ENA HI-RES TEMPORAL	IMAP-Hi, IMAP-Ultra	Reduced energy range, energy resolution, and sky coverage per map	
		X	X	THERMAL IONS	SWAPI	Narrower energy range and reduced cadence	
		X	X	THERMAL ELECTRONS	SWE	Narrower energy range and reduced cadence	
			X	SOLAR WIND COMPOSITION AND CHARGE-STATES	CoDICE-Lo	Narrower energy range, reduced energy resolution, reduced cadence, and reduced composition	
X		X	X	PICK-UP IONS	SWAPL CoDICE-Lo	Narrower energy range, reduced energy resolution, and reduced cadence	
		X	X	SUPRATHERMAL IONS	CoDICE-Hi	Narrower energy range, reduced energy resolution, reduced cadence for pickup H	
		X	X	ENERGETIC PROTONS AND HEAVY IONS	HIT	Reduced energy resolution and energy range	
		X	X	3D MAGNETIC FIELD	MAG	High rate sampling removed and reduced resolution	
X				DUST COMPOSITION	IDEX	Not in threshold	
X				UV 121.6 mn Ly-a	GLOWS	Not in threshold	

Table 4 provides the observation capabilities of all ten IMAP instruments, including their covered ranges, resolutions, and cadences of observations.

The IMAP instruments have been built, tested, and verified to meet the full Baseline science requirements in all areas. As shown in Fig. 8, IMAP meets (blue) all of the Baseline requirements and in most cases exceeds them (green) providing added resiliency for both 1) accomplishing all of the IMAP mission science goals and 2) going ever farther with new scientific firsts, discoveries, and insights.

On the ground, detailed calibrations were carried out for all instruments. In addition, we cross calibrated pairs of instruments: IMAP-Lo with IMAP-Hi, IMAP-Hi with IMAP-Ultra, and SWAPI with CoDICE together in the same beamline at the same time. This innovation was first carried out on IBEX and was expanded for IMAP. CoDICE and HIT were also cross calibrated by using radioactive sources and a standard reference detector. In all



Table 4 Summary of IMAP Instrument Suite Capabilities

Instrument	Observable	Range	Resolution	Cadence
SWAPI	SW ions and PUIs, 1D VDFs	0.1–20 keV/q	SW FoV: 30° × 10°	SW: ≤ 1-min
			Energy ΔΕ/Ε: 0.085 PUI FoV: 220° × 20° Energy ΔΕ/Ε: 0.085	PUI ≤ 10-min
CoDICE-Lo	SW and ST ions and PUIs, w/ composition and charge states, 3D	0.5–80 keV/q	Angular: ≤15° Energy ΔE/E: 0.04	≤ 1-hour
CoDICE-Hi	VDFs ST and EP ions, w/ composition, arrival direction	0.05–2 MeV/nuc	m/ $\Delta$ m $\geq 2$ (He) Angular: $\leq 30^{\circ}$ Energy $\Delta$ E/E: 0.41 m/ $\Delta$ m $> 4$	≤ 1-min
HIT	EP, electrons and ions w/ composition, 3D distributions at	Ions: 2–70 MeV/nuc Elec: 0.5–1 MeV	Angular: $24^{\circ} \times 22.5^{\circ}$ Energy $\Delta E/E$ : $\sim 0.10$ m/ $\Delta m > 10$	≤ 1 min for H, ≤ 10 min for He, ≤ 1hr for
SWE	several energies SW electron, 3D VDFs	1–5000 eV	Angular: $\leq 30^{\circ}$ Energy $\Delta E/E \leq 0.15$	O and Fe ≤ 1-min
MAG	Magnetic field vector	±512 nT; ±60,000 nT; (auto-ranging)	4 pT @512 nT	2 Hz (64 Hz for around 8 hours/day)
IMAP-Lo	ISN and ENA flux and composition	5–1000 eV	Angular: $9^{\circ}$ Energy $\Delta$ E/E: 0.7 and 1 m/ $\Delta$ m $\geq$ 4	Full Sky-Map: 1-year
IMAP-Hi	ENA flux and composition	0.41–15.6 keV	Angular: $4.1^{\circ}$ Energy $\Delta$ E/E: $0.47$ m/ $\Delta$ m $\geq 4$	Full Sky-Map: 6-months
IMAP-Ultra	ENA and EP flux and composition	ENA: 3–300 keV Ions: 3–5000 keV	≤6° at ≥10 keV H Energy ΔE/E: 0.12 - 0.21 (intrinsic resolution).	Full Sky-Map: 3-months
			sky maps binned in $\sim$ 0.4 $\Delta$ E/E to optimize SNR.	
			SSD: m/∆m ~4	
			MCP: H (lights), O (Heavies)	
IDEX	Interstellar and interplanetary dust	$2 \times 10^{-13} - 5 \times 10^{-11} \text{ g};$ 1–286 amu	$m/\Delta m > 120$ at 56 amu	Continuous collection of discrete events
GLOWS	$H(Ly-\alpha)$ glow	120.5±4.3 nm	Angular: 4°	1 light curve per pointing

cases, by independently knowing the input ion and neutral sources, we can guarantee correct intercalibration of different instrument sensitivities and other properties through the overlapping energy ranges. In-space, cross-calibrations are essentially continuous amongst all instruments with overlapping energy ranges, although the input source is, of course, not independently known. Finally, in flight GLOWS observes EUV bright stars, which are characterized and function effectively as standard candles.





Fig. 8 Summary of instruments' top-level requirements and margins. Blue coloring indicates fully meeting Baseline requirements, while green indicates exceeding them

Much of the background in IBEX's ENA images, as well as background in numerous in-situ observations from other missions, stem from the energetic particles and radiation in the near-Earth, magnetospheric space environment. Thus, when we developed and proposed the IMAP mission concept, we chose to station the spacecraft in the much quieter Sun-Earth L1 point. IMAP measurements also benefit significantly from our approach of having the IMAP spacecraft be a sun-pointed spinner, like IBEX. In the case of IMAP, however, we repoint the spin axis each day by  $\sim 1^{\circ}$  (360°/365.24 days) to keep the spacecraft spin axis



pointed  $\sim$ 4° to the right of the Sun center. This angle accounts for the aberration of the solar wind ( $\sim$ 4° on average at 1 au) and minimizes its effect on the ENA observations.

The size of the Lissajous orbit is important. For IMAP, we have settled on a  $+/-9.5^{\circ}$  ×+/-3.9° orbit around L1. This size balances the competing goals of maximum lifetime for the mission within the propulsion capabilities and the tightness of the ellipse needed to do our solar wind science. In particular, the in-situ instruments (SWAPI, CoDICE, HIT, SWE, and MAG) benefit from making measurements within a correlation length. The solar wind correlation length, while variable, is of order  $1 \times 10^6$  km ( $\sim 150 R_{\rm E}$ ) at 1 au (e.g. Weygand et al. 2011), so making measurements within around a correlation length of the Earth-Sun line throughout the orbit makes them good predictions of what will shortly arrive at Earth. This orbit also provides a truly unique opportunity for multi-spacecraft studies of the small-scale structure of the solar wind in combination with other L1 spacecraft making measurements contemporaneously with IMAP (SWFO-L1, ACE, Wind, DSCOVR, SOHO, and Aditya-L1). The IMAP spacecraft and mission design ensure adequate propulsion for an extended mission out to at least five years, and if the launch is at all close to nominal, there should be propellent to last much longer.

In the ten subsections below, we briefly summarize each of the 10 IMAP instruments' design and capabilities. For each instrument, more complete descriptions are provided in the individual instrument papers of this IMAP collection.

#### 4.1 SWAPI

The Solar Wind and Pickup Ion (SWAPI) instrument (Rankin et al. 2025; Fig. 9) measures the combined distributions of the solar wind thermal plasma (H<sup>+</sup> and He<sup>++</sup>) and lighter species of PUIs (H<sup>+</sup> and He<sup>+</sup>). SWAPI primarily contributes to Science Objectives 1 and 4 (Sect. 1 and Tables 2 and 3 above), with measurements that contribute to the fundamental understanding of the solar wind, sources and acceleration of particles, PUIs, and physical processes regulating the global heliosphere. SWAPI's observations of the PUI He<sup>+</sup> distribution from low energies to beyond the PUI cutoff (0.1 to 20 keV/q energies; with about 10 min. cadence), for example, enable high time-resolution measurements of the PUI gravitational focusing cone. This, combined with measurements from CoDICE, IMAP-Lo, and GLOWS allows determination of the LISM flow properties with unprecedented accuracy (Sect. 2.2). Meanwhile, SWAPI also delivers the high time and energy resolution required to observe the spatial structure and transients in the solar wind plasma that are key to identifying energetic particle sources and linking these to local acceleration processes (Sect. 2.1). Specifically, this includes plasma properties (e.g, velocity, density, temperature) derived from 1D distribution functions of solar wind H<sup>+</sup> and He<sup>++</sup>, as well as the first measurements at high time resolution ( $\sim$ 12 s) of the suprathermal tail. SWAPI also contributes to I-ALiRT by extending the ACE solar wind measurements to high time resolution (12 s), with an energy resolution of 27 energy bands per decade.

SWAPI is a spherical top-hat electrostatic analyzer that draws substantial heritage from the Solar Wind Around Pluto (SWAP) instrument on the New Horizons spacecraft (McComas et al. 2008a). SWAP was designed to measure the solar wind and interstellar PUIs at large distances from the Sun, as well as Pluto-generated PUIs. Because of the large distances and the wide range of viewing directions, SWAP was designed to have extremely high sensitivity, a very large field of view, and very low backgrounds. These attributes allowed SWAP to make unprecedented measurements of Pluto's interaction with the solar wind (McComas et al. 2016), as well as unique measurements of the Jovian magnetotail to distances beyond 2500 R<sub>J</sub> (McComas et al. 2007) and fundamental observations of interstellar PUIs



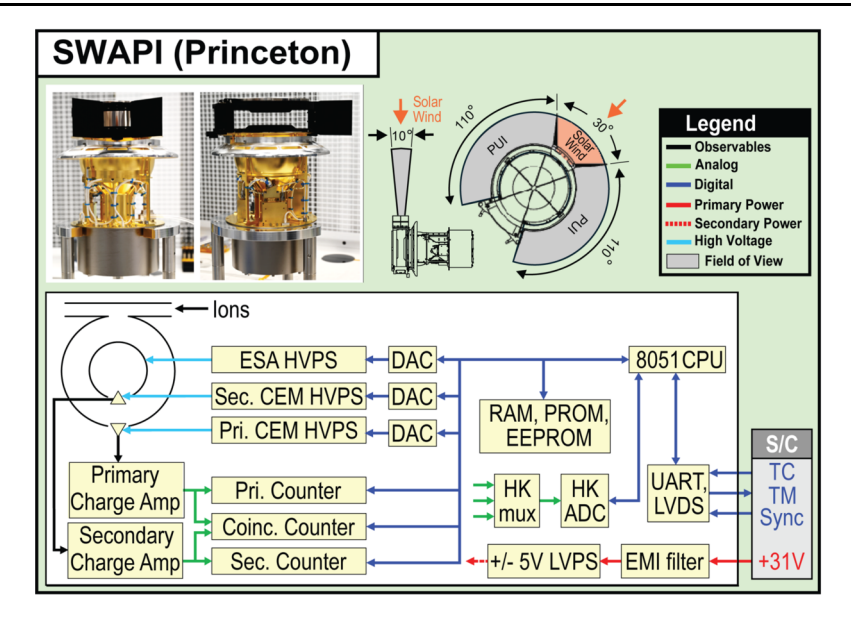


Fig. 9 IMAP's SWAPI instrument, including block diagram and FOVs

(McComas et al. 2021, 2025, and references therein). SWAP continues to make excellent observations of the solar wind and interstellar PUIs, now out past 60 au (McComas et al. 2025). SWAPI returns similar types of measurements, but at higher time cadences and over a wider energy range. In the early days of the SWAPI instrument development, several key modifications were made to the original SWAP design to better adapt it for in-situ measurements at 1 au. Among these were the removal of the retarding potential analyzer (RPA), thereby significantly increasing the open area for PUIs, and the replacement of the deflector ring with a shorter grounded aperture cutoff ring, which provides increased elevation-angle FOV.

The contrast between the high-intensity solar wind and low-intensity PUIs is accounted for at SWAPI's entrance (e.g., the blackened upper section in Fig. 9) by an aperture grid assembly, which includes an electroless-nickel grid with many thousands of tiny holes that reduces the solar wind flux by a factor of ~1000, and carefully designed protruding vanes to manage vignetting. The final version of these features was achieved by a combination of experimentally driven instrument design decisions and forward modeling based on more than 50 years of OMNI data. The configuration of the solar wind-viewing sector enables 0.1% transmission while keeping 99.99% of the solar wind from entering the instrument unattenuated and keeping 99% of the nominal solar wind from scattering within the ESA. Restricting the solar wind in this way leaves the remaining 221.5° of the aperture open for unrestricted entrance of PUIs (plus an additional 12.3° vignetted region on either side of the vanes), as depicted in the instrument FOVs (Fig. 10).

SWAPI's key instrument performance parameters are summarized in Table 5. The instrument ion-optics section comprises: (i) the above-described aperture grid assembly; (ii) an Electrostatic Analyzer (ESA) with energy-per-charge (E/q) selection; (iii) a field-free flight path; and (iv) a coincidence detector section. These elements select the energies and attenuation factors for the measured solar wind and PUIs. Transmitted ions are post-accelerated into the detector section that employs an ultrathin carbon foil (e.g., McComas et al. 2004)



100 Page 26 of 82 D.J. McComas et al.

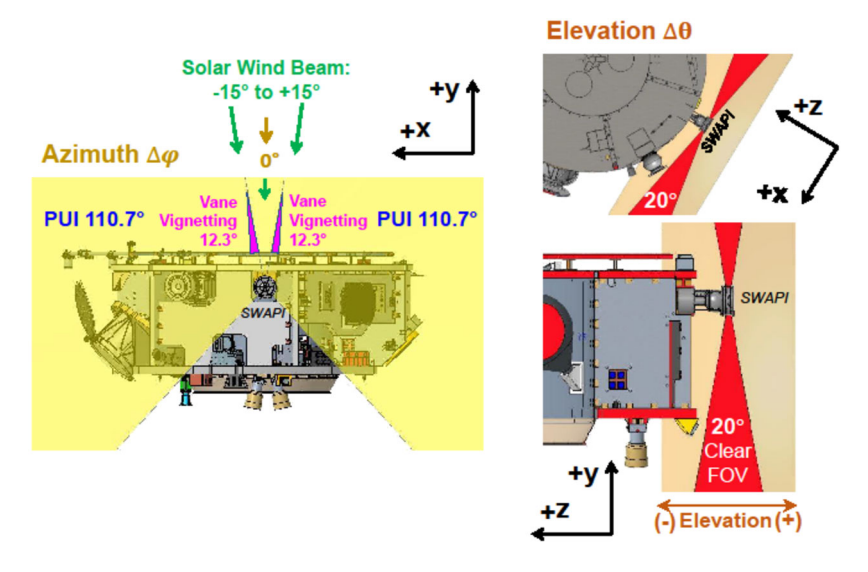


**Fig. 10** SWAPI's azimuth and elevation angle FOV's on IMAP spacecraft. Viewing of solar wind (green) is separate from that for PUIs (yellow)

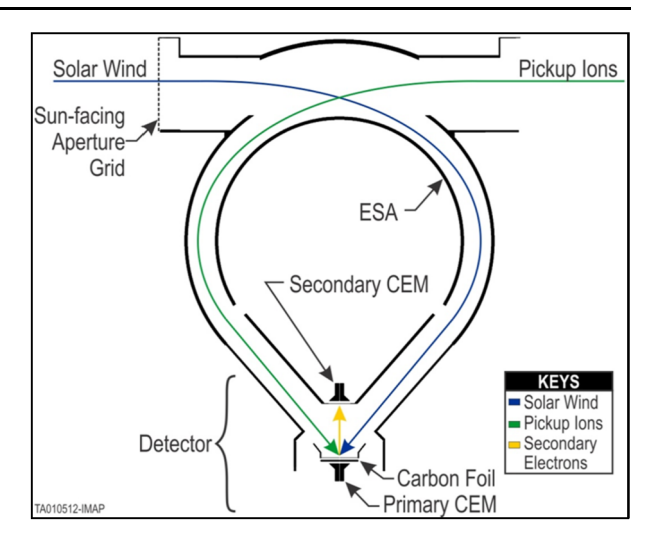
 Table 5
 SWAPI instrument performance parameters

Parameter	Performance		
Instrument Type	Top-hat top plate Electrostatic Analyzer		
Species	SW H <sup>+</sup> and <sup>4</sup> He <sup>++</sup> ; combined PUI He <sup>+</sup> & H <sup>+</sup>		
Energy Range	0.89 to 21.4 keV/q		
Energy Resolution (dE/E)	8.1% Full Width at Half Maximum (FWHM)		
Time Resolution	12 s		
Number of Steps	72 (1 ramp, 62 course, 9 fine)		
Field of View	Sun-viewing: $30^{\circ} \times 10^{\circ}$		
	Non Sun-Viewing: $221^{\circ} \times 20^{\circ}$ (factors in vignetting)		
GF (cm <sup>2</sup> sr eV/eV)	SW Sun-Viewing: $1.00 \times 10^{-7}$ cm <sup>2</sup> sr eV/eV for SW H+		
	(cold plasma w/ 5°FWHM beam)		
	PUI Non-Sun-Viewing: $2.25 \times 10^{-2}$ cm <sup>2</sup> sr eV/eV for PUI He+		
	(hot plasma approximation)		
Dynamic Range	2 MHz to 0.07 Hz counting rates		
Signal to Noise Ratio	Min. SNR of 1 @ 0.07 Hz coincident count rate		
Mass	3.01 kg		
Volume	$0.011 \text{ m}^3$		
Power	2.37 W (peak power, 12 s cycle average)		
Telemetry	443.2 bps (housekeeping + science)		

and two CEMs: a primary CEM (PCEM), which measures ions that pass through the carbon foil, and a secondary CEM (SCEM), which attracts secondary electrons liberated from the carbon foil. A cross-section of the ion-optics is shown in Fig. 11; the instrument block diagram is shown in Fig. 9.



**Fig. 11** SWAPI ion-optics cross section



SWAPI's electronics include a High Voltage Power Supply (HVPS), Low Voltage Power Supply (LVPS) and Processor Board (PB). The ESA, PCEM, and SCEM are tied to three separate HVPSs controlled by an 8051 microcontroller. The ESA HV steps up to 10.2 kV while the CEM HVs are set to separate steady values, up to 4 kV, to maintain detector saturation. Primary and secondary pulses are received from charge amplifiers and accumulated in counters. If both occur within a 100 ns window, a coincidence (COIN) is also registered. SWAPI consists of a single integrated mechanical assembly with a two-sensor detector section and an electronics enclosure. The instrument is mounted on a spacecraft-provided bracket, which in turn is mounted to the bottom side of the top deck of the spacecraft Bay D. The electrical interface with the spacecraft is via a single D type pin power connector and a single subminiature D type data socket connector. The data connector also incorporates connections to the spacecraft Arm and Test Panel for instrument Disable/Safe/Arm selection using the appropriate spacecraft-provided connectors.

The lower-level SWAPI (Level 2) data of primary, secondary, and coincidence count rates over full energy-range sweeps of the ESA, accumulated every 12 s. These count rates reflect values integrated over the entire instrument FOV and most of a spacecraft spin, providing the combined 1D SW and PUI distribution as a function of energy per charge. Forward modeling fits are then performed to the distribution to separate amongst the SW H<sup>+</sup>, SW He<sup>++</sup>, and PUIs, to return parameters such as the density, temperature, and speeds of each population (Level 3a). Inputs from the instrument calibration are also incorporated into the algorithms to report the combined differential flux (Level 3b).

#### 4.2 CoDICE

The Compact Dual Ion Composition Experiment (CoDICE; Livi et al. 2025; Fig. 12) measures the 1) elemental, ionic charge state, and isotope composition and the 3-Dimensional (3D) velocity distribution functions (VDFs) of solar wind He – Fe ions and interstellar pickup He, O, and Ne ions in the  $\sim$ 0.5–80 keV/q energy range in CoDICE<sub>Lo</sub>, and 2) the mass composition and arrival direction of  $\sim$ 0.03–5 MeV/nuc ions in CoDICE<sub>Hi</sub> (Desai et al. 2015, 2016; Desai 2017). These measurements, summarized in Table 6, are required to 1) determine the LISM composition and flow properties and 2) discover the origin of the enigmatic ST tails and advance understanding of the acceleration of particles in the heliosphere.



100 Page 28 of 82 D.J. McComas et al.

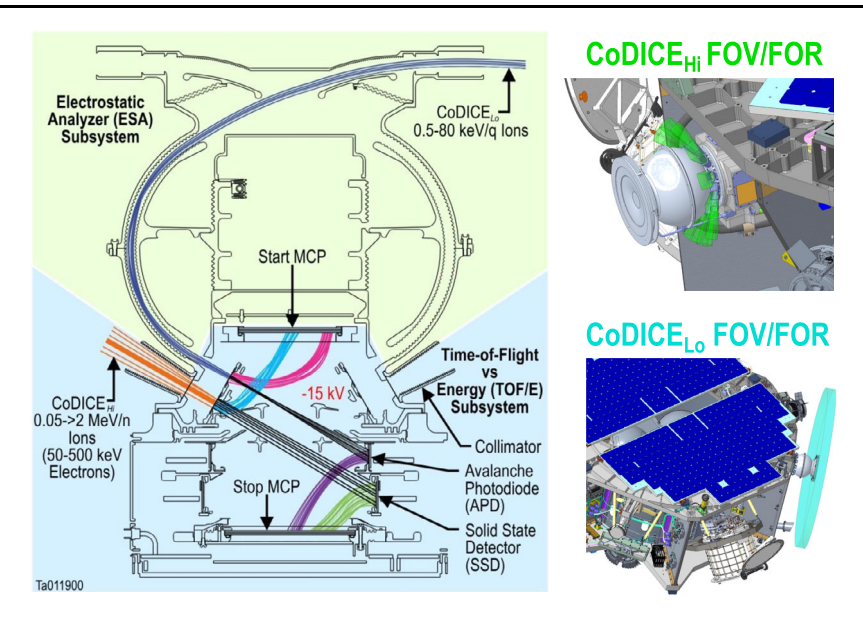


Fig. 12 CoDICE cross-section showing the electro-optical design and simulations of particle trajectories through the ESA and TOF/E subsystems (left). Fields-of-View (FoVs) of the CoDICE $_{\rm Hi}$  (top right) apertures and the CoDICE $_{\rm Lo}$  ESA entrance (bottom right)

The CoDICE sensor comprises two major sub-systems, namely: 1) an ESA, and 2) a Time-of-flight (TOF) vs. residual energy (E) spectrometer. CoDICE<sub>Lo</sub> measures ions between  $\sim 0.5$  and 80 keV/q that enter through the collimated aperture (blue trajectories in Fig. 12) and are selected and focused according to their E/q by the ESA into the Start TOF subassembly. The E/q sweeping steps up to the maximum voltage for the next stepping cycle when SW H $^+$  count rate near  $\sim$ 1 keV/q exceeds a predefined threshold rate. The Start subassembly, biased at -15 kV, accelerates the incoming ions before they strike a thin C foil ( $\sim 1~\mu g~cm^{-2}$ ) at the entrance of the TOF/E subsystem. This interaction produces secondary electrons (red trajectories) that are guided to the outer annulus of the Start MCP. The azimuthal arrival directions of the incoming ions are measured by a position-sensing delay line embedded within the Start MCP subassembly. CoDICE<sub>Lo</sub> measures the full energy range as the ESA steps through all 128 voltage steps during a 4-minute interval. The mostly neutralized ions (black trajectories) then traverse a  $\sim$ 10.64 cm flight path and strike one of 24 Avalanche Photodiodes (APDs, each 300  $\mu$ m thick with an active area of 3×5 mm<sup>2</sup>), where they generate secondary electrons that are guided to the center of the Stop MCP (purple). The TOF between the Start and Stop MCP signals yields the ion velocity. The residual energy E of the neutralized ion is measured by one of the 24 azimuthally distributed APDs that collectively provide  $6^{\circ} \times 360^{\circ}$  instantaneous FOV and cover  $\sim 1.8 \,\pi$  sr in a single spacecraft spin. The combined measurements, E/q, TOF, and E, determine the mass (M), charge state (q), and M/q.

CoDICE<sub>Hi</sub> measures ions between  $\sim$ 0.03 and >2 MeV/nuc (orange) that enter the common TOF/E subsystem through 12 separate  $10^{\circ} \times 16^{\circ}$  FOV collimators and two 100 nm foils that attenuate UV light to <0.1% and stop low-energy (<10 keV) protons. The external foil is 100 nm aluminum, and the internal foil is 50 nm aluminum with 50 nm polyimide. Start and Stop MCP signals are generated by secondary electrons (light blue and green) that are produced as the ions traverse a thin  $\sim$ 1  $\mu$ g cm<sup>-2</sup> C foil located at the TOF/E entrance, The



Table 6 CoDICE performance

Parameter	CoDICE <sub>Lo</sub>	CoDICE <sub>Hi</sub>
Instrument type	PUI, SW, and ST Ion Spectrometer, ESA/TOF/E	ST and Energetic Particle Spectrometer, TOF/E
Species	Interstellar PUIs: PUIs: ${}^{3}\text{He}^{+}$ , ${}^{4}\text{He}^{+}$ , $N^{+}$ , $O^{+}$ , ${}^{20}\text{Ne}^{+}$ , ${}^{22}\text{Ne}^{+}$ , $Ar^{+}$ , SW and STs: Mass and Q-states of SW He-Fe	H-Fe
Energy Range and Resolution	0.5-80 keV/q, $\Delta$ E/E=4%	Ions: $\sim$ 0.05 – >2 MeV/n @ 7 bins/decade
Mass Range and Resolution	M: 3–56 amu; $(M/q)/\Delta(M/q)>60$ (mass dependent) $(M)/\Delta M>6$ (mass dependent)	M: 1–56 amu (M)/ΔM>12
Instantaneous FOV, El. × Az.; Sky Coverage	$24.6^{\circ} \times 6.6^{\circ}$ apertures over $360^{\circ}$ azimuth; ${\sim}1.8~\pi$ sr in full spin	$12~10^{\circ} \times 16^{\circ}$ apertures over $360^{\circ}$ azimuth; $\sim 2.1~\pi$ sr in full spin
Dynamic Range	Quiet time – 10 <sup>5</sup> counts/sec	Quiet time – 10 <sup>5</sup> counts/sec
Time Resolution	1 hr for 3D VDFs of $\mathrm{He^+}$ , <30 min for SW composition	1 min for H, He, e <sup>-</sup> and 15 minutes C-Fe in gradual SEP events
GE of GF	$>2.6 \times 10^{-3}$ cm <sup>2</sup> sr eV/eV; variable to reduce SW He <sup>2+</sup> counts	$\sim$ 0.156 cm <sup>2</sup> sr
Observing Modes	E/q scans optimized to reduce H counts and increase duty cycle of STs	Single mode
Mass	16.1 kg	
Volume	0.0413 m3	
Power	18.5 W @ Hot Operation, 25.1 W average @ Cole	d Operation
Raw Telemetry (4-min	Science: 4762 kbps	Science: 1505 kbps
cycle) Telemetry	I-ALiRT: 115 bps 640 kBps	I-ALiRT: 32 bps 640 kBps

mostly neutralized ions (black trajectories) then traverse a  $\sim$ 12.3 cm flight path and strike one of 12 SSDs distributed over 360° azimuth, respectively. Each SSD, 700  $\mu$ m thick with an active area of 15×15 mm², determines the ion's residual energy. The residual energy along with the TOF, which yields the ion velocity, provides the ion mass. These secondary electrons are detected by the same MCPs shared with CoDICE<sub>Lo</sub>, but in separate areas; Hi-Start electrons (light blue) are guided toward the center portion of Start MCP, and Hi-Stop electrons (green) are guided toward the outer annulus of Stop MCP. CoDICE<sub>Hi</sub> covers 2.1 $\pi$  sr in each spacecraft spin.

Figure 13 shows the CoDICE overall block diagram. CoDICE electronics box (Ebox) comprises the following major subassemblies: 1) LVPS; 2) Processer Board; 3) Sensor High Voltage Power Supply (HVPS-1); 4) Ion-Optics Power Supply (HVPS-2). The LVPS interfaces with the spacecraft via a nine pin D type connector. The LVPS accepts +31 V nominal spacecraft primary power to create secondary voltages (+3.3 V, ±5 V, ±12 V) for all CoDICE subassemblies. The Processor Board interfaces to the spacecraft RS-422 data bus via a nine socket MDM type connector for all spacecraft commands and all instrument telemetry. The Processor Board also interfaces to the spacecraft Arm and safe panel via a nine pin MDM type connector for instrument Disable/Safe/Arm selection using the appropriate spacecraft-provided plugs. The Processor Board: 1) provides a centralized system for command, monitoring, and control; 2) acquires, processes, and packetizes all detector data; 3) provides temperature, current, and voltage monitoring of the HVPS, LVPS, and the



100 Page 30 of 82 D.J. McComas et al.

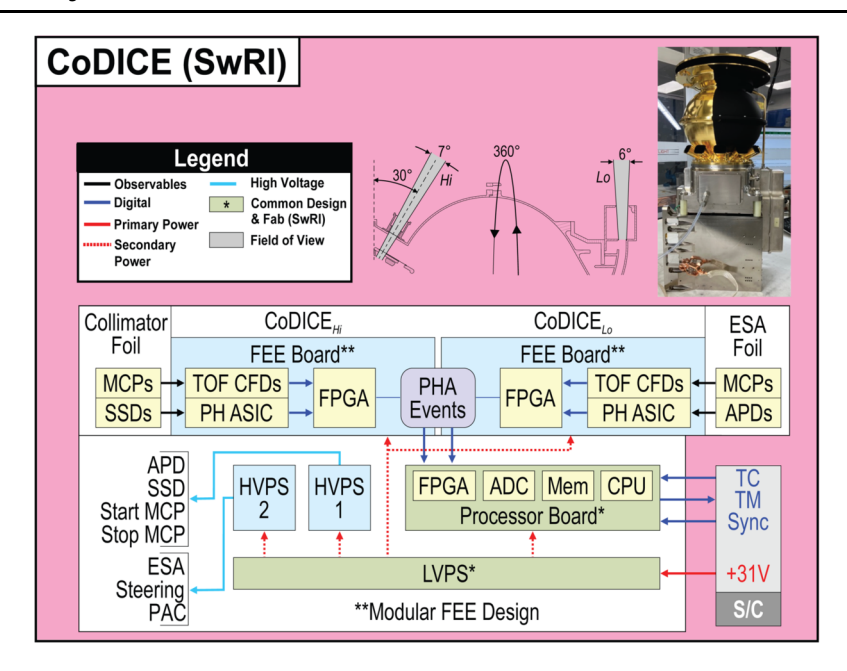


Fig. 13 CoDICE block diagram, with CoDICE flight instrument (inset)

sensor; and 4) distributes a high voltage power supply safing signal. HVPS-1 has 4 HV converters, namely, 1) sensor bulk; 2) 10-stage Start MCP; 3) 8-stage Stop MCP; and 4) APD Bias.

The Sensor Bulk (HVPS-1) supply produces a steady output voltage of +6000 V. The bulk output feeds directly into the Stop Steering regulator (+3200 V nominal, HV optocoupler based) which is resistor divided to produce the SSD Steering voltage (+1600 V nominal). The sensor bulk provides +670 V from a tap on the multiplier/filter to an additional three outputs. One of these three outputs (SSD Bias) also has an HV optocoupler based regulator. The remaining two outputs (APD Optics and SSD Lens) derive from resistive dividers from the previously mentioned tap. The 10-stage Start MCP supply produces an output voltage programmable from zero to -3400 V with up to 120  $\mu$ A. The 8-stage Stop MCP supply produces an output voltage programmable from zero to +5000 V with up to 120  $\mu$ A. The MCP Back voltage is set to a fixed voltage from +1600 V by using a shunt HV optocoupler. This voltage increases as the Stop MCP voltage increases until it reaches +1600 V, then it is regulated to a fixed +1600 V as the Stop MCP voltage continues to increase. The APD Bias supply produces a programmable output voltage of zero to +650 V. There is a slave APD Bias 2 supply producing zero to  $\sim +600$  V to bias 3 APDs that measure particles from the solar wind direction. Since APD Bias 2 is a regulated voltage from APD Bias 1, it cannot generate a voltage greater than the programmed APD Bias 1 voltage.

The Ion-Optics Bulk (HPS-2) supply produces a programmable output voltage from 0 to -15,500 V (nominal -15,000 V) at up to  $200 \mu \text{A}$ . The output of this Bulk supply feeds directly into the ESA-A (Entrance) and ESA-B (Main) HV optocoupler based negative polarity stepping power supplies. This Bulk supply also feeds a resistive divider which provides the Post-Acceleration output (nominal -15,000 V), the Steering output (nominal -13,240 V) and the Start Optics Grid (nominal -2647 V). The backplane routes secondary power from the LVPS to all other CoDICE subassemblies. It routes command and telemetry



from and to the CDH. Processor board for command & data handling (C&DH) All electrical interfaces within the EBox are via cPCI connectors. The low voltage electrical interface to the sensor section is via a pigtail two row 51 pin MDM type connector between the EBox and the Front End Electronics (FEE) housed inside the sensor.

The low voltage terminal block assembly provides for lower-level high voltage termination via high voltage pigtails exiting directly from HVPS-1 & -2 at the EBox exterior prior to being integrated with the CoDICE sensor assembly. The higher voltages were terminated after the sensor section was integrated with the EBox. The lower-level high voltages include: Ion-Optics HVPS voltages and the Start Optics Grid, and Sensor HVPS voltages consisting of Start MCP, Stop Steering, Stop Anode, Start Anode, APD Optics, SSD Lens, SSD Steering, Stop Grid, and Stop MCP Back.

 $CoDICE_{Lo}$  solar wind and pick-up ion data products include 1D and 3D VDFs for multiple species.  $CoDICE_{Hi}$  provides the arrival directions of ST ions with priority given to heavy ion species. CoDICE contributes to the I-ALiRT data stream to provide the solar wind proton intensities and solar wind charge state ratios data products. CoDICE also provides binned data products and direct event data products. The direct event data products contain the complete measurement information for each ion event that is telemetered based on the respective priority schemes, while the binned data provide counts/intensities as a function of energy, detector (APD and SSD), and spin angle at different cadences depending on the data product. Standard data-level definitions are Level 0: the raw CCSDS packets; Level 1a: raw count data decommutated into formatted variables; Level 1b – counts converted to count rates; Level 2: validated science products with count rates converted to intensities using instrument calibration factors; Level 3: higher level science data.

#### 4.3 HIT

The High-energy Ion Telescope (HIT) instrument (Christian et al. 2025; Fig. 14) measures ions from 2-50 MeV/nucleon (species dependent) which, at  $\sim$ 1 au primarily have their origin as SEPs and low energy ACRs. HIT contributes to IMAP Science Objective 4 (see Sect. 2) by observing the elemental composition, energy spectra, angular distributions, and arrival times of H to Ni and linking them to suprathermal measurements from CoDICE. HIT also distinguishes <sup>3</sup>He ions, which are an important tracer of SEP acceleration processes (See Table 7). Eight of the ten HIT apertures are sensitive to ions and are oriented so that as IMAP spins, they observe the full sky ( $4\pi$  sr FOV) (Fig. 14 and Fig. 15). Two additional apertures have been modified to be sensitive to electrons arriving from the sunward and anti-sunward directions with energies of a few hundred keV to a few MeV. These electrons are key pieces to understanding SEP acceleration and transport. These electrons are also important to space weather because their near relativistic speeds can provide valuable early warning for the arrival of large storms (Posner 2007). Selected HIT electron and ion rates are included in the I-ALiRT data to facilitate space weather work. HIT is based on the Low Energy Telescope (LET, Mewaldt et al. 2008) that was flown on the two Solar Terrestrial Relations Observatory (STEREO) spacecraft.

HIT uses a series of silicon solid-state detectors (SSDs) and the classic  $\Delta E/E_{tot}$  method to identify SEP ion species. The ten apertures have nominally identical 24  $\mu m$  thick detectors (L1s) that are circular with a 2 cm² area, divided into three active regions. These L1 detectors and their collimators determine the arrival direction (Fig. 16). The two electron apertures have 1500  $\mu m$  thick circular with 2 cm² SSDs (L4s) directly behind the L1s that have an inner active area with a radius of 5.9 mm and an outer annulus 1.5 mm wide. The L1 detectors in these apertures and the annulus regions of the L4s are used as active anticoincidence to remove low-energy protons and all heavier ions, with the electrons of interest



100 Page 32 of 82 D.J. McComas et al.

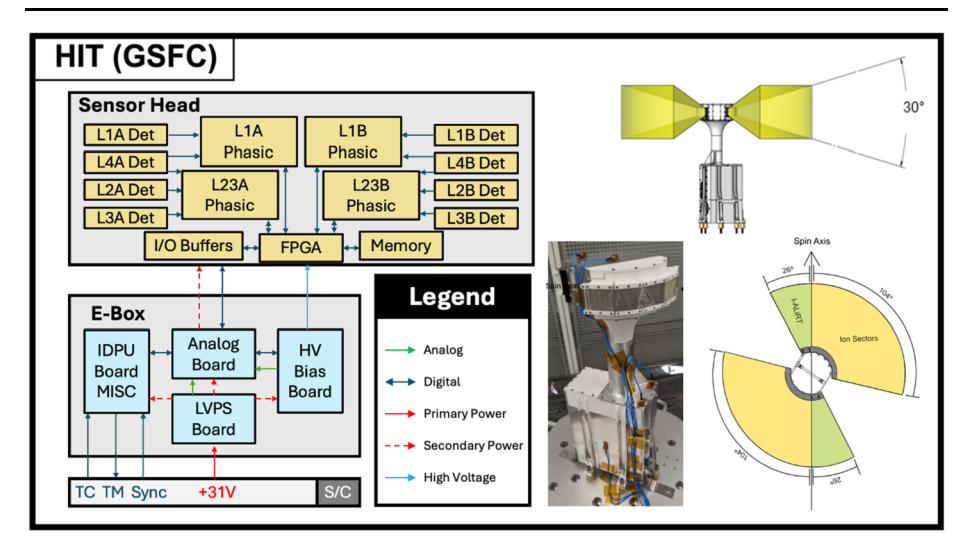


Fig. 14 HIT Block Diagram, Photo, and FOV

**Table 7** HIT instrument performance parameters

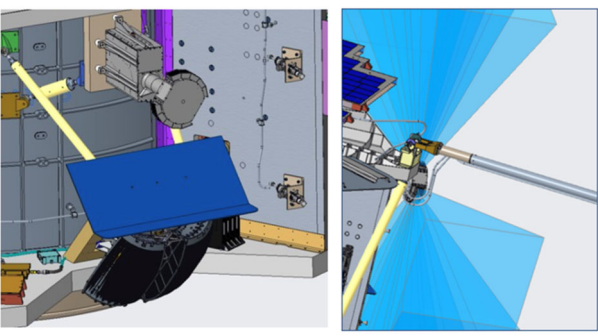
Parameter	Performance	
Instrument Type	Silicon SSD $\Delta$ E/E <sub>tot</sub> ion and electron analyzer	
Species	e <sup>-</sup> , H, <sup>3</sup> He, <sup>4</sup> He, C, N, O, Ne, Mg, Si, S, Ar, Ca, Fe, and Ni	
Energy Range	$\sim$ 1 MeV/nucleon to $\sim$ 70 MeV/nucleon, species dependent	
Energy Resolution (ΔE/E)	~0.1	
Time Resolution	1 minute	
Ion Field of View	Instantaneous two fans $130^{\circ} \times 30^{\circ}$ , with spin $4\pi$	
Electron Field of View	$\sim$ 30° half-angle cone, sunward and anti-sunward	
Mass	3.50 kg	
Volume	$9 \text{ cm} \times 7 \text{ cm} \times 18 \text{ cm}$	
Power	5.96 W	
Telemetry	745 bps	

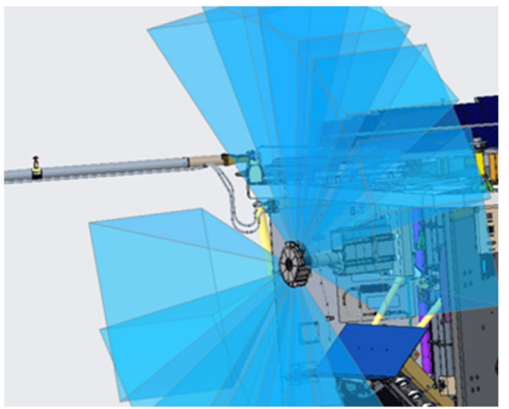
stopping in the inner region of the L4 detectors. Particles from all apertures can stop in a stack of four rectangular SSDs at the center of the sensor head, two 50  $\mu$ m thick rectangular detectors (L2s) with a 10.2 cm<sup>2</sup> area and 10 active regions on the outsides of the stack and two 1000  $\mu$ m thick rectangular detectors (L3s) with 15.6 cm<sup>2</sup> area and three active regions in the middle (Fig. 16).

Two of the active areas on each of the L3 detectors are ganged together, giving a total of 58 signals that are digitized in four dual-range 11-bit 16-channel custom Pulse Height Analyzer ASICs (PHASICs). These PHASICs, the FPGA that controls them, and all their support components reside on a two-part FEE board in the HIT sensor head. Power and digital signals are transferred inside a bracket that attaches the sensor head to an electronics box. The electronic box and bracket are used to position the sensor head so that it has clear a FOV. The electronics box contains four boards, an Analog Board that distributes signals



**Fig. 15** HIT location on spacecraft and FOVs





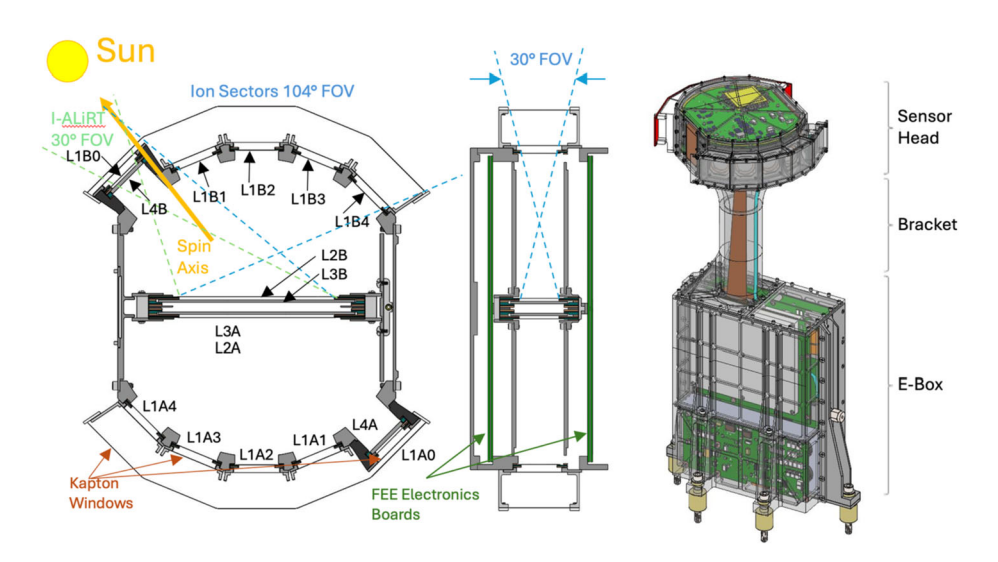


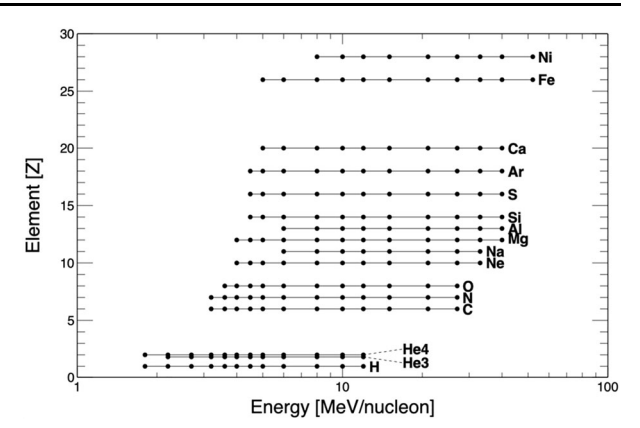
Fig. 16 HIT orientations and locations of SSDs

to the other boards, an Instrument Data Processing Unit (IDPU) board, a LVPS, and a HV Bias board that generates the HV (maximum 250 V) bias for the SSDs.



100 Page 34 of 82 D.J. McComas et al.

Fig. 17 Visualization of energy bins for all ion species measured by HIT. Dots indicate boundaries of the bins, which can be adjusted by uploading new lookup tables if necessary



The processed HIT data (Level 2) consists primarily of omnidirectional particle species intensities (particles  $MeV^{-1}$  cm<sup>-2</sup> sr<sup>-1</sup> s<sup>-1</sup>) at a one-minute cadence. The species and energies are shown in Fig. 17. There are also wider energy bins included to improve statistics during quiet times. Statistical uncertainties are reported and systematic uncertainties are added when they are identified and quantified.

For studies of anisotropy, there are sector intensities at a ten-minute cadence for 10 species and energies. For the sector intensities, the full sky  $(4\pi \text{ sr})$  is divided into 120  $22.5^{\circ} \times 24^{\circ}$  sectors with eight 22.5° bins between the spin axis and counter-spin axis times fifteen 24° bins in the spin direction. The ten sector species are 1.8-4 MeV H, 4-6 MeV H, 6-10 MeV H, 4-6 MeV/n  $^4$ He, 6-10 MeV/n  $^4$ He, 4-6 MeV/n CNO (combined), 6-12 MeV/n CNO, 4-6 MeV/n NeMgSi, 6-10 MeV/n NeMgSi, and 4-12 MeV/n Fe.

Level 3 data consist of full-sky anisotropy maps with B and the Sun direction shown (see sector intensities above), and the pitch-angle histograms derived from those maps.

HIT also is included in the I-ALiRT space weather data stream. The I-ALiRT data consists of six electron rates (three energies each in the roughly sunward and anti-sunward directions), three proton rates (one omnidirectional and two with a higher energy in the sunward and anti-sunward directions), and two omnidirectional helium rates.

#### **4.4 SWE**

The Solar Wind Electron (SWE) instrument (Skoug et al. 2025; Fig. 18) is a spherical section electrostatic analyzer that measures the distributions of solar wind thermal and suprathermal electrons. SWE primarily contributes to IMAP Science Objective 4, understanding particle injection and acceleration processes near the Sun (Sect. 2). SWE in-situ electron measurements provide observations of spatial structures and transients in solar wind plasma that contribute to particle acceleration and transport processes as well as providing context for IMAP ENA measurements. SWE measurements of suprathermal electrons in combination with magnetic field measurements from MAG enable determination of the electron pitch angle distribution, which provides information about the solar wind magnetic topology. While suprathermal electrons typically flow out from the Sun along the magnetic field, the presence of counter streaming pitch angle distributions, in which these electrons are observed flowing both inward and outward along the magnetic field, provides a key signature of coronal mass ejections, which can lead to geomagnetic storms. SWE also contributes to I-ALiRT, providing the first real time space weather measurements of suprathermal electrons.



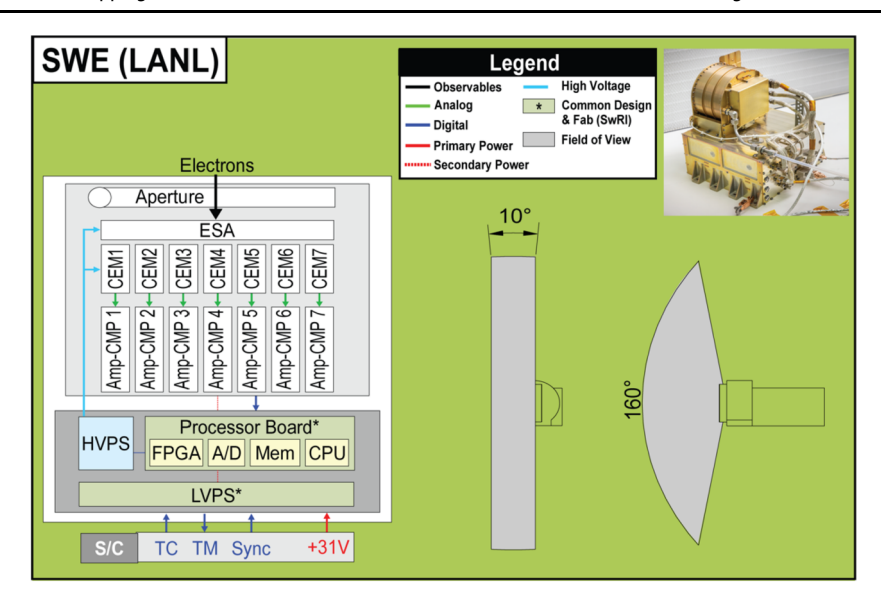


Fig. 18 IMAP-SWE instrument, including block diagram and field of view

SWE is a high-heritage instrument, based on the design flown as the Ulysses/SWOOPS (Bame et al. 1983, 1992), ACE/SWEPAM (McComas et al. 1998b), and Genesis/GEM (Barraclough et al. 2003) solar wind electron instruments. SWE consists of a sensor head (SH) mounted on top of an EBOX. The SWE electro-optics are a nearly exact copy of the heritage instruments, with updated electronics, detectors, and mechanical housing design. The SH includes the ESA, 7 CEM detectors to measure electrons entering the instrument from different angles, and front-end electronics to amplify the signal for transmission to the EBOX. A cross-section of the electro-optics is shown in Fig. 19. Electrons enter SWE through a small aperture. A positive high voltage on the inner ESA plate allows only electrons within a narrow range of energies and azimuthal angles to pass through the ESA and be detected by the CEMs. The ESA voltage is stepped to cover the full energy range. Electrons entering at different polar angles are detected in different CEM detectors, giving a fan-shaped field of view (Fig. 18). As the spacecraft spins, the FOV sweeps out >95% of  $4\pi$  sr. SWE uses the IMAP Common Electronics (ICE) electronics box (EBOX, as indicated by asterisks in Fig. 18). EBOX electronics include the LVPS, HVPS, and Command and Data Handling (CDH) board, and a backplane connecting these boards. The HVPS includes a CEM HV to bias the detectors, and an ESA HV which biases the ESA to transmit particles of different energies. The ESA HV steps up to 1200 V for measurement of particles up to 5 keV. The CEM HV is nominally set to 2300 V but can be adjusted in flight up to 4200 V if needed to keep the CEMs in saturation. Electrons are counted as a function of ESA step and spacecraft spin angle in each of the seven CEM detectors. The SWE key instrument performance parameters are summarized in Table 8.

SWE Level 2 data consist of electron phase space density or intensity over the full range of energies and angles. Full coverage of energies and spin angles is obtained over four space-craft spins (60 s), with a lower resolution measurement in both energy and angle obtained every 15 s. SWE Level 3 data include electron pitch angle distributions and moments of the thermal and suprathermal electrons. SWE i-ALiRT data use algorithms developed for the Genesis/GEM solar wind categorization (Neugebauer et al. 2003) to identify the presence



100 Page 36 of 82 D.J. McComas et al.

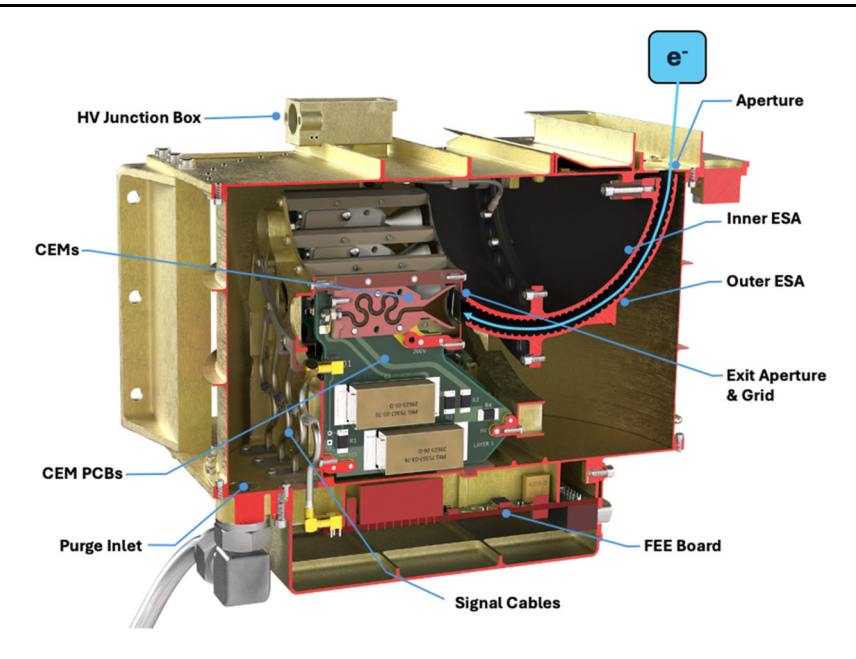


Fig. 19 SWE sensor head cross section, including an electron (e<sup>-</sup>) trajectory through the ESA to a CEM detector

 Table 8
 SWE instrument performance parameters

Parameter	Performance	
Instrument Type	Spherical Section Electrostatic Analyzer	
Species	Solar Wind electrons	
Energy Range	1 eV to 5 keV	
Energy Resolution ( $\Delta E/E$ )	0.14	
Time Resolution	60 s, with a lower-resolution measurement every 15 s	
Field of View	$160^{\circ} \times 360^{\circ}$ over a spacecraft spin	
GF (cm <sup>2</sup> sr eV/eV)	$(4-8) \times 10^{-4} \text{ cm}^2 \text{ sr eV/eV per CEM}$	
Mass	5.7 kg	
Volume	$26.5 \times 25.5 \times 28.5 \text{ cm}$	
Power	10.6 W	
Telemetry	800 bps	

or absence of counter streaming electrons in real time, contributing to the identification of solar wind structures such as ICMEs that can lead to space weather at Earth.

### 4.5 MAG

The IMAP magnetometer (MAG; Horbury et al. 2025; Fig. 20) is a conventional dual sensor fluxgate instrument, which measures the magnetic field local to the spacecraft. The large-scale structure of the magnetic field guides the propagation of energetic ions and electrons, while finer scale structure scatters them, and field-particle interactions can energize them.



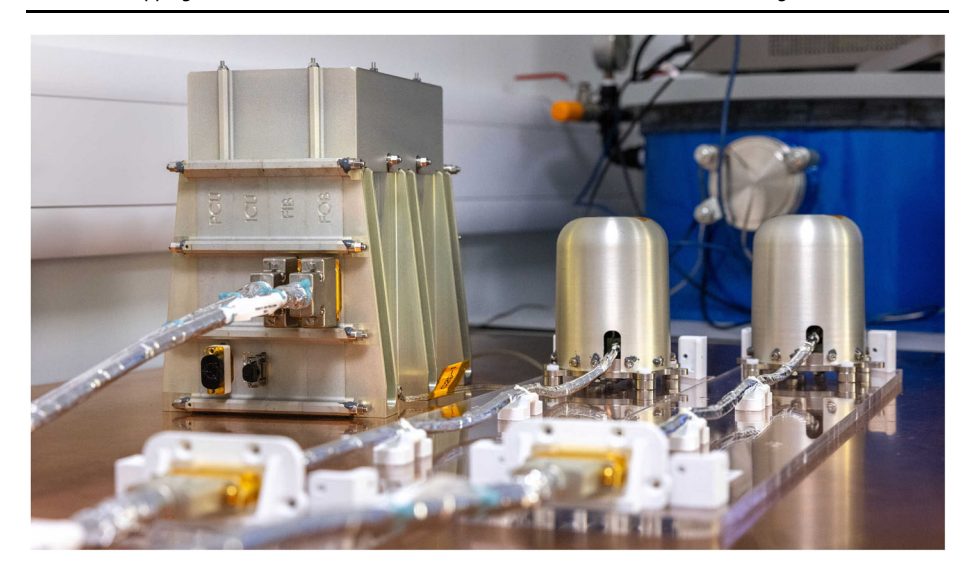


Fig. 20 The IMAP flight model magnetometer: electronics box on left, two sensors on right

Fine scale structure of the magnetic field at collisionless shocks is central to the reflection and acceleration of charged particles. An accurate measurement of the magnetic field, in combination with particle measurements from SWAPI, CoDICE, SWE and HIT is therefore central to IMAP Science Objective 4 (see Sect. 1).

The MAG instrument is different than that originally proposed for IMAP and is largely based on the Solar Orbiter magnetometer (Horbury et al. 2020), which has operated successfully for over 5 years. Significant modifications compared to the Solar Orbiter instrument include a change of the data interface from SpaceWire to UART, removal of sensor heaters (since the IMAP sensors are illuminated at all times), and the incorporation of some improvements to the power supply taken from the JUICE instrument design. The two sensors are connected to the electronics box, located within the spacecraft body, via a harness. The electronics box (Fig. 21) contains one power supply board, one front-FEE board for each sensor, and one instrument controller unit (ICU) board. The FEE boards contain the digital drive and sensor circuitry for each sensor (O'Brien et al. 2007) and communicate to the ICU via serial peripheral interface (SPI) links. The ICU runs the RTEMS operating system on a 25 MHz Leon3 processor running on a RTAX FPGA. It filters and reduces the data from each sensor using a tuned second order filter and delivers packetized data to the spacecraft via UART link, receives commanding, and monitors instrument health parameters such as voltages, currents and temperatures. As well as fixed boot software, three copies of the flight software are stored in MRAM and can be updated in flight if needed.

The two MAG sensors are mounted on a deployable boom, one at the tip around 3 m from the spacecraft body and one 75 cm inboard of that. Use of a long boom reduces the effect of spacecraft-generated fields on the measurements, while the two sensors combined enable direct characterization of the spacecraft-generated signals and the effective removal of them. The main scientific data products are based on measurements from the outboard sensor, while comparison of data between the two makes it possible to characterize the effect of magnetically "noisy" spacecraft operations such as thruster firings and remove them from the final products. An extensive magnetic cleanliness and control program was



100 Page 38 of 82 D.J. McComas et al.

Fig. 21 The MAG instrument is composed of two sensors on the deployable boom, connected to the electronics box in the spacecraft body. Each sensor is associated with a FEE board which drives the sensor and digitises the magnetic field measurements. These are transmitted to the Instrument Control Unit which filters and reduces the data before sending it to the spacecraft

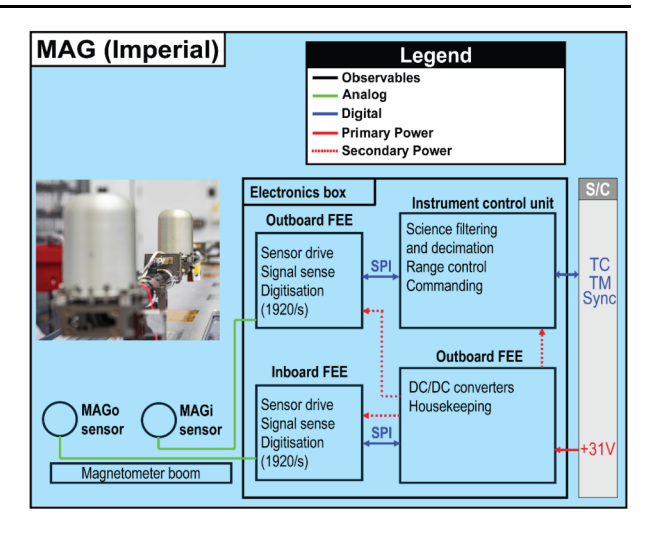


Table 9 MAG instrument performance parameters

Parameter	Performance	
Instrument Type	Dual sensor fluxgate magnetometer	
Normal mode cadence	2 vectors/s from both sensors	
Burst mode cadence	64 vectors/s outboard sensor; 8 vectors/s inboard	
Burst mode coverage (dE/E)	> 8 hours/day	
Digital resolution	4 pT	
Noise at 1 Hz	<10 pT	
Nominal range	±512 nT at 4 pT resolution	
Maximum range	$\pm 60,000$ nT at 1.8 nT resolution	
Mass	5 kg	
Power	7.75 W	
Telemetry	563 bps normal mode; 13,079 bps burst mode	

undertaken by the IMAP project, with both DC and AC characterization of the spacecraft and key subsystems including all scientific instruments.

The normal mode measurement rate is 2 vectors  $s^{-1}$  from each sensor, allowing good characterization of all magnetohydrodynamic (MHD) scale fluctuations and structures. Implementation of a novel lossless data compression algorithm has allowed for more than a factor of two improvement in data return compared to that originally proposed. Combined with other optimization of the telemetered stream this will provide  $\sim$ 8 hours per day of burst mode data at 64 vectors  $s^{-1}$  from the outboard sensor. This rate is sufficient to characterize ion cyclotron waves associated with pick-up ions, fluctuations upstream of collisionless shocks associated with reflected and accelerated ions, and the internal structure of the shocks themselves. All these phenomena are central to IMAP science.

The instrument performance is summarized in Table 9. MAG's resolution, at 4 pT, is similar to the noise level of the instrument at 1 Hz. This resolution is maintained for fields up to  $\pm 512$  nT, which is larger than any expected during the mission at L1. The MAG instrument does, however, auto-range into a series of larger, but less sensitive ranges if needed.



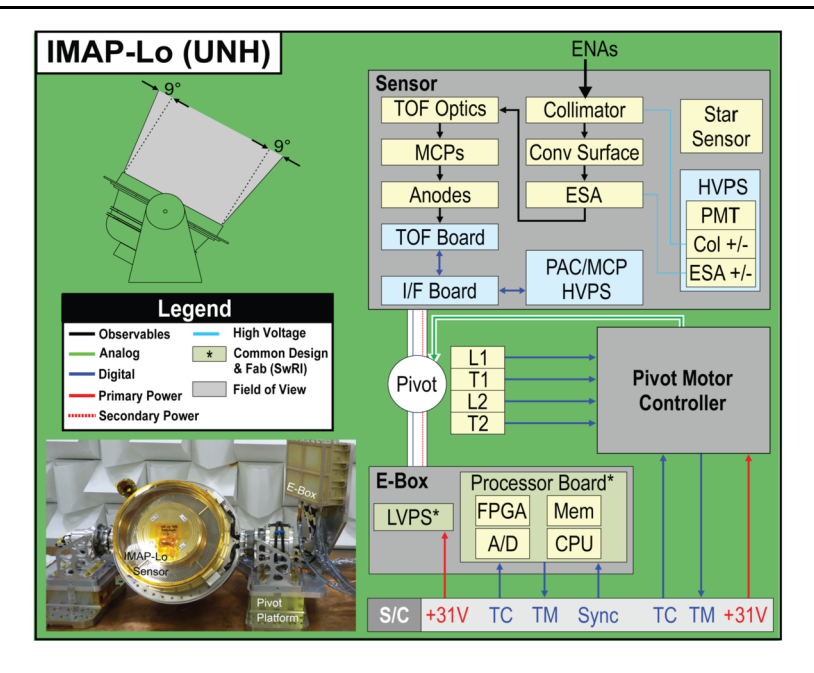


Fig. 22 IMAP-Lo instrument, including block diagram and FOV

The largest of these comfortably covers Earth fields, allowing for ground testing without the need for any magnetic shielding.

MAG scientific data is distributed as Level 2 products, with a continuous normal mode product at 2 vector s<sup>-1</sup> (reconstructed from the 64 vector s<sup>-1</sup> data when burst mode is operating), along with the burst mode product when it is available. MAG also generates a real time I-ALiRT data product, of one vector every 4 seconds from each sensor. Downlink of data from both sensors allow a simple real-time cleaning of magnetic contamination from the data without human intervention. Since the orientation of the interplanetary magnetic field upstream of the Earth is the most important parameter in determining energy input into the magnetosphere, MAG data is critical for space weather monitoring.

#### 4.6 IMAP-Lo

IMAP-Lo (Schwadron et al. 2025; Fig. 22) is a single-pixel neutral atom imager, mounted on a pivot platform. IMAP-Lo provides energy and spin-angle binned measurements of interstellar neutral atoms (ISN H, He, O, Ne, and D) tracked over >180° in ecliptic longitude. Utilizing a pivot platform, IMAP-Lo can articulate its field-of-view to break the measurement degeneracy and vastly improve the angular resolution of ISN flow parameters, which are tracked over much of the year. The large and greatly improved integration times are used to determine composition of the interstellar medium and provide critical new understanding of the secondary neutral atom populations produced in the heliosheath (Sect. 2.3). Besides the ISN measurements, IMAP-Lo provides global maps of ENA H and O binned with energy. IMAP-Lo ENA maps of the outer heliospheric boundaries (Sect. 2.2) extend down to 100 eV and below and up to 1 keV with a much lower background than IBEX-Lo. IMAP-Lo contributes to Science Objectives 1 – 3 (Sect. 1 and Tables 2 and 3 above): (O1) understanding of the composition of interstellar neutral atoms and the flow properties of the



local interstellar medium; (O2) understanding of the temporal and spatial evolution of the interstellar boundary region by mapping neutral atoms at relatively low energies down to 100 eV; and (O3) advancing our understanding of processes related to the interactions of the magnetic field of the Sun and the local interstellar medium mapping the IBEX ribbon down to low energies and mapping secondary interstellar neutral atom populations produced in the deflected and heated interstellar plasma of the heliosheath.

IMAP-Lo draws heritage from the IBEX-Lo instrument (Fuselier et al. 2009a) and was designed to provide accurate measurements of interstellar flow parameters, which set the outer boundary conditions of interstellar interactions, while simultaneously mapping the outer boundaries of the heliosphere at low energies. IBEX's direct H, D, He, O, and Ne ISN observations (Möbius et al. 2009, 2012; Rodríguez Moreno et al. 2013; Saul et al. 2012; Schwadron et al. 2015, 2016; Swaczyna et al. 2022a) provided new information with expanded species coverage, discovered secondary populations of ISN He (Kubiak et al. 2014, 2016) and ISN O (Park et al. 2016), greatly increased signal-to-background ratios. The IBEX-Lo ISN measurements show a direct relationship between the ISN flow longitude and speed via the neutral atom trajectory equation, resulting in a large uncertainty (referred to as the IBEX ISN measurement degeneracy) in the longitude or speed (Möbius et al. 2012; Bzowski et al. 2015; McComas et al. 2015) because of the limited longitude range of the IBEX observations (i.e. IBEX-Lo measurements are provided over a limited range of  $\sim 30^{\circ}$ in longitude). IMAP-Lo exploits the pivot platform to track the interstellar flow, allowing IMAP to finally break the measurement degeneracy and increase opportunities to measure ISN atoms throughout the year (Schwadron et al. 2022; Bzowski et al. 2022). The pivot platform also enables ENA mapping with significant enhancements in collection power (by a factor of  $2 \times$  to  $\ge 6 \times$ , Kubiak et al. 2023) in regions of concentrated latitudinal exposure, depending on the pivot platform orientation (i.e., boresight directions  $\alpha \geq 90^{\circ}$  to the spin direction, IMAP-Lo views regions up to maximum ecliptic latitudes =  $90^{\circ} - \alpha$ ).

IMAP-Lo has a much larger collection power than IBEX-Lo using increased geometric factors ( $\geq$ 4×) and its L1 position to significantly increase viewing time with lower backgrounds. In the design phase, there were three elements that promised increases in geometric factor (G): larger 9° × 9° field-of-view increased G by 1.9×, removal of the IBEX-Lo high-resolution sector increased G by 1.2×, and the implementation of the high throughput mode with improved energy acceptance, which increased G by 1.7×. Together, these factors increase G by ~3.9× compared to IBEX-Lo. Geometric factors derived from IMAP-Lo calibration are larger than estimated during design (the overall increase in G is ~6× that of IBEX-Lo). Additional increases in G were due to: (a) removal of P2-grids used in IBEX-Lo to shape the electrostatic field at the collimator exit; (b) TOF efficiencies increased due to the use of thinner 1  $\mu$ g cm<sup>-2</sup> foils; (c) the increased size of the conversion surface.

These improvements allow IMAP-Lo to enhance the weak heliospheric neutral signal while significantly reducing ion, electron, and UV background sources. Data products, including neutral atom differential energy fluxes, and interstellar neutral atom rates, are used to deduce interstellar flow properties, secondary distributions and relative abundances (e.g., ISN Ne/O, and D/H). Another key data product is the neutral atom direct event count lists, which characterizes measured TOF spectra and help determine the relative abundances and neutral atom fluxes.

Absolute pointing knowledge of IMAP-Lo to  $\leq 0.1^{\circ}$  accuracy is achieved by a co-located star sensor with the same boresight direction as the IMAP-Lo sensor. The design is identical to that of IBEX-Lo (Hlond et al. 2012; Fuselier et al. 2009a), except for the photomultiplier (PMT) and an edge filter for wavelengths in the red to reduce the sensitivity to Milky Way and Zodiacal Light background. The pivot platform orients the IMAP-Lo boresight up to



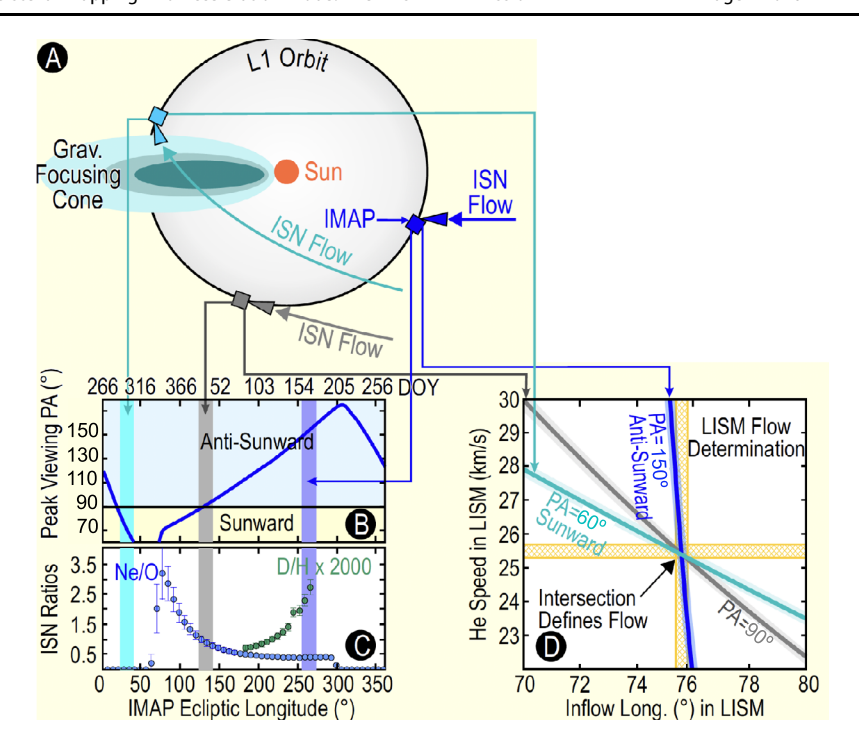


Fig. 23 IMAP-Lo tracks the interstellar flow to precisely determine the species-dependent flow speed, temperature, and direction of the LISM that surrounds, interacts with, and determines the outer boundaries of the global heliosphere. IMAP-Lo returns detailed abundances, defining the composition of the LISM. The ecliptic longitude (three cases shown along IMAP L1 orbit in top schematic), arrival direction relative to the Sun, and hyperbolic trajectory of the ISN bulk flow determine a characteristic relation between inflow longitude and speed at infinity. Panel B shows expected ISN flow direction relative to the Sun versus ecliptic longitude and IMAP Day of Year (DOY), including aberration due to orbital motion around the Sun, and panel C the expected Ne/O and D/H with statistical uncertainties for one orbit. IMAP-Lo uses the pivoting FOV (pivot angle, PA to spin-axis) to pinpoint the intersection in the relation between the ISN inflow speed and longitude to uniquely determine the LISM flow vector (panel D)

180° from the sun-pointed spin axis, enabling the boresight to follow the interstellar flow direction through more than 180 days of the year (see Fig. 23). This increases counting statistics for accurate determinations of LISM abundance ratios, Ne/O and D/H (Fig. 23, panels B and C). The varied orientation of the IMAP-Lo instrument breaks the IBEX-Lo ISN measurement degeneracy (panel D).

The IMAP spacecraft provides clear fields-of-view (Fig. 24) for both IMAP-Lo and the star sensor over pivot-angles from 60° to 180°. The cutout in the S/C deck allows for clear views at large pivot angles. The 60° position is the launch-lock position for the sensor, and the 90° position, where IBEX-Lo was mounted, is the nominal configuration used for mapping the heliosphere.

IMAP-Lo's key instrument performance parameters are summarized in Table 10. Neutral atoms enter through the collimator with a 9° FWHM FOV. Electrons <600 eV and ions <3 keV are eliminated by a cylindrical set of deflection electrodes just outside the collimator. The deflectors are nominally set to +4 kV on the inner electrode, and -3.5 kV on the outer electrode. After passing through the collimator, atoms strike the conversion surface made of diamond-like carbon coated on a Si wafer (Sokół et al. 2024), which converts some



100 Page 42 of 82 D.J. McComas et al.

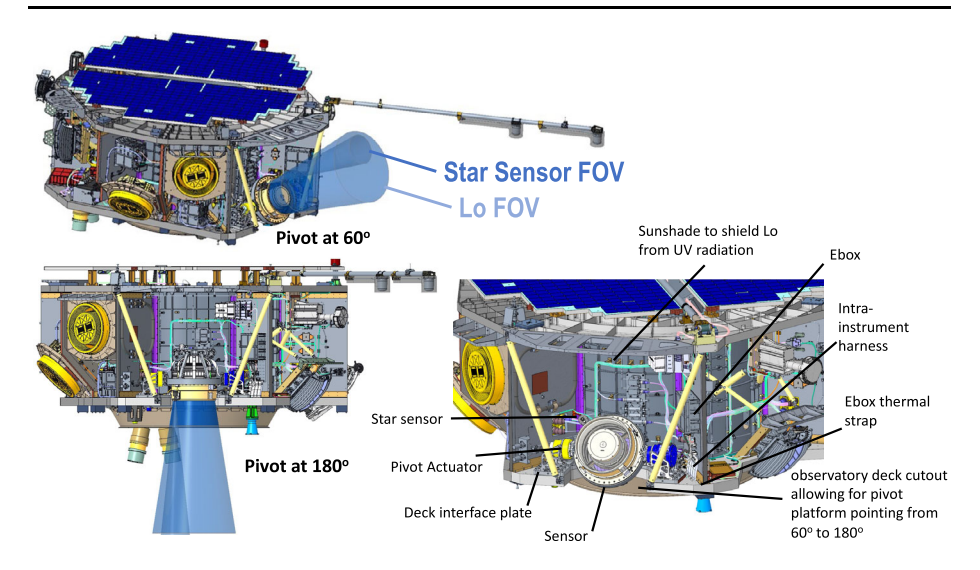


Fig. 24 (Left) IMAP-Lo and star sensor clear FOVs as a function of pivot angle (Right) IMAP-Lo mounted on the IMAP spacecraft

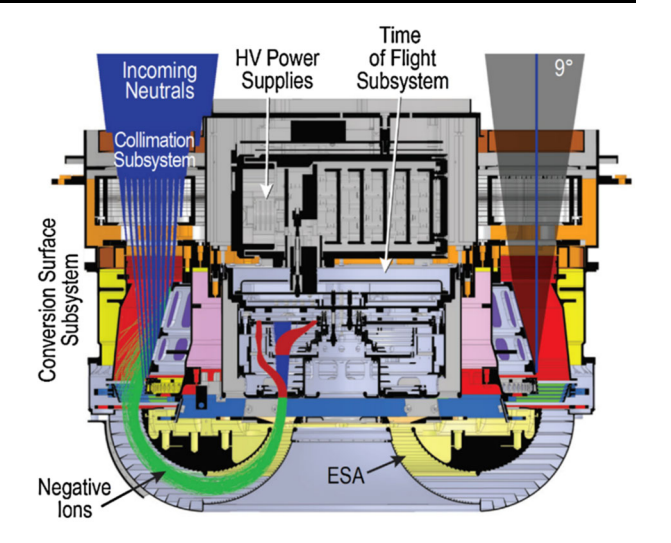
Table 10 IMAP-Lo instrument performance parameters

Parameter	Performance Single-Pixel ENA Imager	
Instrument Type		
Species	Energetic Neutral Atom H, Interstellar H, D, He, O, and Ne	
Energy Range	5 to 1000 eV	
Energy Resolution ( $\Delta E/E$ )	0.7 (HiRes Mode), 1.0 (HiThru Mode)	
Time Resolution	$\sim$ 7 minutes with 15 s spin period	
Number of Steps	7	
Field of View	$9^{\circ} \times 9^{\circ}$ , pivoted FOV $61^{\circ} - 180^{\circ}$ to spin-axis	
GF (cm <sup>2</sup> sr eV/eV)	HiRes H $1.1 \times 10^{-4}$ and HiThr H $2.7 \times 10^{-4}$ at $\sim 100$ eV	
Dynamic Range	$1 \times 10^{-3}$ /sec to 80/sec for triple TOF Counts	
Signal to Noise Ratio	ISN He $> 10,000$ , ISN H $> 1000$ , ISN O $> 100$	
	ISN Ne, $D > 10$ , ISN Secondary He $> 100$	
	ISN Secondary O > 10, Average ENA H S/N > 50	
Mass	Total: 44.573 kg; Sensor Mass with MLI: 17.068 kg	
Volume	Sensor on PPM w Harness: 65,750 cm <sup>3</sup> ; Ebox: 5300 cm <sup>3</sup>	
Power	Without PPM: 21.62 W; With PPM 38.11 W	
Telemetry	686 bps	

neutral atoms into negative ions (Wurz et al. 1995; Wurz 2000; Fuselier et al. 2009a; Möbius et al. 2009). Resulting negative ions are pre-accelerated into a toroidal ESA. Secondary- and photo-electrons are removed by a ring of magnets near the entrance of the ESA. The instrument provides two selectable energy passbands: Hi-Throughput mode (HiThr) has  $\Delta E/E \sim 1$ , and Hi-Resolution mode (HiRes) has  $\Delta E/E \sim 0.7$  similar to that of IBEX-Lo (Fuselier et al. 2009a). UV photons and scattered particles are rejected using a CuS black surface and



Fig. 25 IMAP-Lo cutaway drawing, overlaid with SIMION ray-tracing (left side) of ENAs (blue), negative ions after the conversion surface (green), neutrals and ions after passing through the Carbon foils in the TOF section (blue), and secondary electrons emitted at the foils (red)



3-bounce design. After exiting the ESA, negative ions are post-accelerated by  $+12~\rm kV$  into the cylindrical triple-coincidence TOF subsystem. The IMAP-Lo TOF subsystem allows the clear separation between light and heavy atoms and suppresses accidental background events using coincidence. The ions pass through the entrance foil (C-Foil<sub>a</sub>, 1  $\mu$ g cm<sup>-2</sup>), followed by passage through a second carbon foil (C-Foil<sub>c</sub>, 1  $\mu$ g cm<sup>-2</sup>), and end their trajectories by producing a stop signal on the MCP detector. During the passage of each foil, secondary electrons are released and steered towards two separate sections of the MCP. This configuration enables one triple coincidence and three double coincidence TOF measurements, which reduces dark count rates to <1 count day<sup>-1</sup> (Möbius et al. 2008; Wurz et al. 2009). Backgrounds of triple-coincidence rates are significantly reduced in comparison to IBEX-Lo. A cross-section of the ion-optics is shown Fig. 25.

The IMAP-Lo electronics box (IMAP-Lo Common Electronics, ICE) provides the interface to the high-voltage bulk supply, the TOF subsystem, the Pivot Platform Mechanism (PPM) and forms data products for transmission to the ground in telemetry. The Interface Board is the single point of contact to the spacecraft through the IMAP-Lo ICE. It handles all power conditioning for the sensor and star sensor, parses incoming commands to the sensor electronics, HV supplies and the star sensor, and directs data from the sensor electronics and star sensor to the ICE.

Direct Events, Monitor Rates and TOF Board Housekeeping are generated on the TOF Board within the HV TOF section, which is floated at 12 kV. The direct events, rates and housekeeping are transmitted to the Interface Board over a single 115.2 kbit/sec optical serial interface. The Interface Board can be thought of as a "bent pipe" where the TOF Board data is guided to the ICE via the Interface Board. Star Sensor data, Interface Board Housekeeping, and register data are digitized on the Interface Board and sent to the ICE, also at 115.2 kbits/sec.

#### 4.7 IMAP-Hi

The High Energy Neutral Atom Imager (IMAP-Hi) (Funsten et al. 2025; Fig. 26) measures energetic neutral atoms (ENAs) from plasma domains in the outer heliosphere over an energy range spanning its seed population (core and suprathermal solar wind). IMAP-Hi



100 Page 44 of 82 D.J. McComas et al.

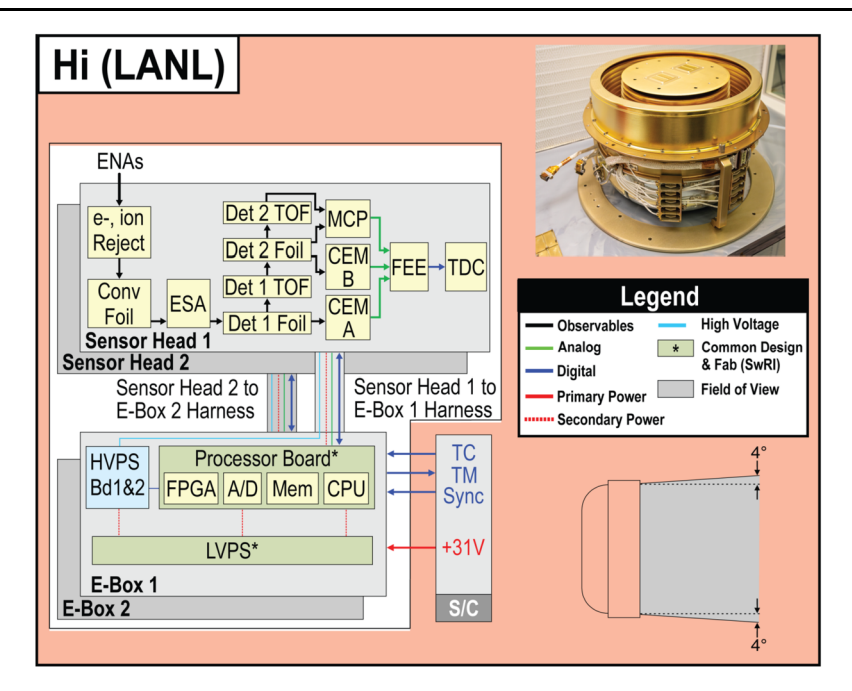


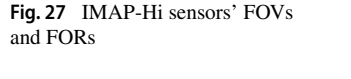
Fig. 26 The IMAP-Hi ENA imager sensor (one of two identical sensors), including block diagram and field of view

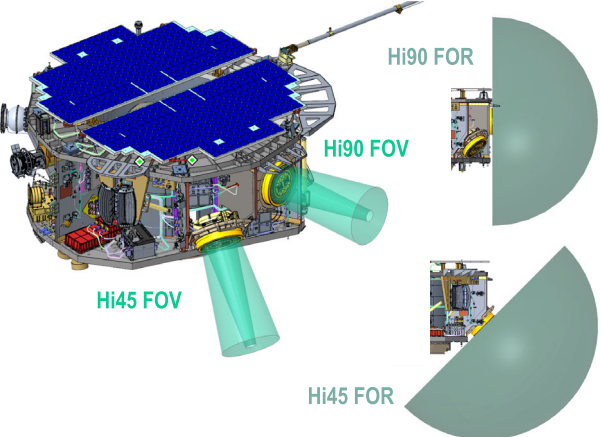
measures Hydrogen ENAs and produces global ENA flux maps over nine contiguous energy passbands spanning an energy range 0.41–15.6 keV FWHM. IMAP-Hi contributes to Science Objectives 2–3 (Sect. 1 and Tables 2 and 3 above): (O2) advance understanding of the temporal and spatial evolution of the boundary region in which the solar wind and the interstellar medium interact, and (O3) identify and advance the understanding of processes related to the interactions of the magnetic field of the Sun and the LISM. The lowest and highest energy passbands of IMAP-Hi overlap with the highest energy passbands of the IMAP-Lo ENA imager (Schwadron et al. 2025) and the lowest energy passbands of the IMAP-Ultra ENA imager (Gkioulidou et al. 2025), enabling ENA flux measurements over the sky that span a broad, contiguous energy range, enabling comprehensive global discovery and understanding of the interaction of the heliosphere and the interstellar medium.

IMAP-Hi consists of two identical single pixel cameras with 4.1° FWHM conical field-of-view (FOV), see Fig. 26. One sensor (Hi-90) is mounted perpendicular to the spin axis; the other (Hi-45) is oriented 45° relative to the spin axis in an anti-sunward direction (Fig. 27). Over each spin, each sensor samples a 4.1° wide circular swath of the sky. As the IMAP spacecraft re-points toward the Sun each day, the circular swaths advance by about 1° day<sup>-1</sup> in ecliptic latitude, such that Hi-90 acquires a full sky map every six months. Hi-90 samples the north and south ecliptic poles every spin but samples an equatorial point only every 6 months. Thus, Hi-45 enables more frequent viewing of latitudes below 45° and, crucially, is focused on lower latitude plasma structures (and their dynamics) such as the heliospheric nose, tail, flanks, and a majority of the IBEX ribbon (McComas et al. 2024).

IMAP-Hi incorporates extensive heritage from the IBEX-Hi ENA imager (Funsten et al. 2009a) but attains far superior angular resolution, energy resolution, energy range, and signal-to-noise ratio, simultaneously with a small increase in geometric factor and signif-







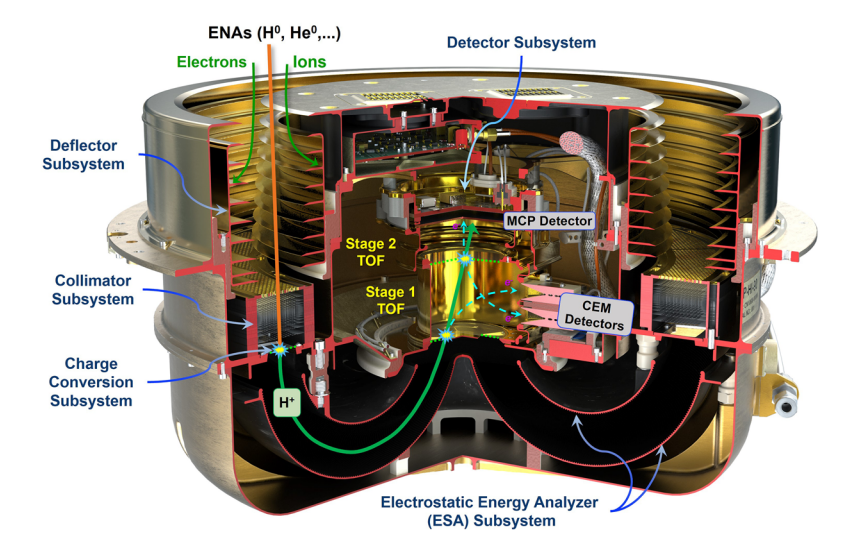


Fig. 28 Schematic of an ENA's path through the IMAP-Hi ENA imager

icant increase in low-background measurement time duty cycle. The measurement technique (Fig. 28) utilizes ultrathin carbon foils to convert ENAs into ions (Funsten et al. 1993; McComas et al. 2004) followed by an electrostatic energy analyzer of "bundt pan" geometry that projects a large area aperture onto a small, centralized detector subsystem. While IBEX-Hi uses coincidence from three detectors, IMAP-Hi incorporates TOF electronics as well as multi-hit detection of its MCP detector to measure TOF across for up to four detection events, providing superior background rejection for penetrating cosmic rays. The FEE receives analog signals from the three detectors, calculates TOF for detector event combinations that lie within pre-set windows, and outputs digital TOF values.

The charged particle rejection and collimator subsystems precede the carbon charge conversion foils to reject ambient charged particles and define the FOV, respectively. To reject ambient charged particles from reaching the carbon foil aperture, IMAP-Hi uses an electrostatic deflector subsystem instead of the more complicated IBEX-Hi electrode configuration



Table 11 IMAP-Hi performance parameters

Parameter	Performance	
Instrument Type	ENA Imager	
Number of Sensors	2 (Hi-45, Hi-90)	
Species	Optimized for H <sup>0</sup>	
Energy Range	0.41 to 15.6 keV (FWHM)	
Energy Resolution, $\Delta E_{\text{FWHM}}/E$	47%	
Number of Energy Steps	9 (contiguous across energy range)	
Pixel Field of View	4.1° FWHM	
Pixel Orientation	Hi-45: 45° relative to spin axis (anti-sunward)	
	Hi-90: 90° relative to spin axis	
Geometric Factor, $G_{\rm E}$	$0.0012 \text{ cm}^2 \text{ sr eV/eV } @ 1.1 \text{ keV}$	
	$0.0175 \text{ cm}^2 \text{ sr eV/eV} @ 12.7 \text{ keV}$	
Time Resolution	18 min per energy sweep (72 spins)	
Mass	35.0 kg	
Volume	Sensor: Ø46.0 cm $\times$ 25.4 cm, EBox: 22.4 cm $\times$ 26.0 cm $\times$ 17.6 cm	
Power	28.1 W	
Telemetry	1496 bps	

that separately rejects ambient electrons and ions but introduced an unanticipated source of background (Wurz et al. 2009). The deflector configuration also enables IMAP-Hi to more than double the maximum energy of the energy range. The collimator consists of a stack of identical plates with high-density hexagonal holes that are co-aligned across the stacked plates to provide a fixed FOV. The IMAP-Hi collimator uses slightly different geometry parameters to attain a 4.1° FOV (FWHM) that is approximately conical.

The EBox, which is separate from the sensor, is the electrical interface to the spacecraft and contains low voltage and high voltage power supplies as well as the command and data handling system. The digital TOF values from the FEE are processed into Direct Event (DE) data. Each detected ENA has a uniquely reported DE record with complete TOF information and information about the spin angle of the spacecraft at the time of measurement, the energy passband, and which sensor recorded the DE. DE data is also accumulated into histograms that are used to validate the DE telemetry stream. Single (non-coincidence) events are also regularly reported so that the absolute detector efficiency of each detector can be monitored over time (Funsten et al. 2005).

IMAP's orbit location around the Sun-Earth Lagrange L1 point provides unobstructed, pristine viewing of the outer heliosphere. This contrasts with the significant backgrounds in IBEX-Hi during orbital segments within the Earth's magnetopause and when viewing the Earth and Moon. The IMAP-Hi performance specifications are shown in Table 11.

### 4.8 IMAP-Ultra

The IMAP-Ultra (Gkioulidou et al. 2025) instrument consists of two identical ENA imagers (Fig. 29) using slit optics to cover  $\sim 3\pi$  sr of the full celestial sphere with each spin over the energy range 3–300 keV with 2° angular resolution for H above 30 keV. IMAP-Ultra builds on the heritage of Cassini/INCA (INCA) (Krimigis et al. 2004) and IMAGE/HENA (HENA) (Mitchell et al. 2000) and is almost an exact copy of the JUICE/JENI (JENI) (Mitchell et al.



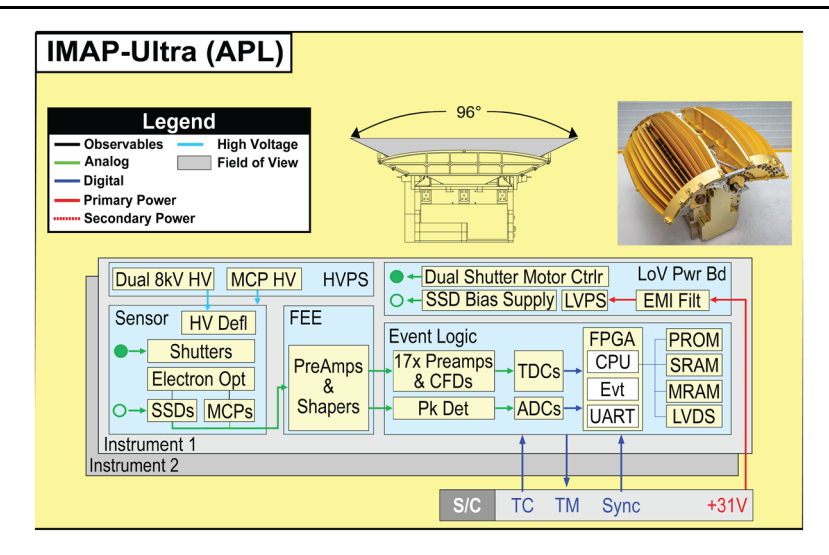


Fig. 29 IMAP-Ultra instrument, including block diagram and Field of Regard (FOR)

2016) instrument. The two IMAP-Ultra imagers, combined with the much higher duty cycle afforded by the IMAP mission design, allow for a collecting power averaging ~35 times that of INCA. IMAP-Ultra delivers ENA images across the suprathermal energy range with background rejection and angular resolution necessary to resolve heliospheric structures, such as the suggested Ribbon-to-Belt transition, which was left unresolved from the INCA and IBEX measurements (Sect. 2.2), as well as physical processes regulating the global heliosphere, such as particle acceleration taking place in the outer heliosphere (Sect. 2.1). Together with the IMAP-Hi and IMAP-Lo ENA imagers, IMAP-Ultra contributes to Science Objectives 2–4 (Sect. 1 and Tables 2 and 3 above).

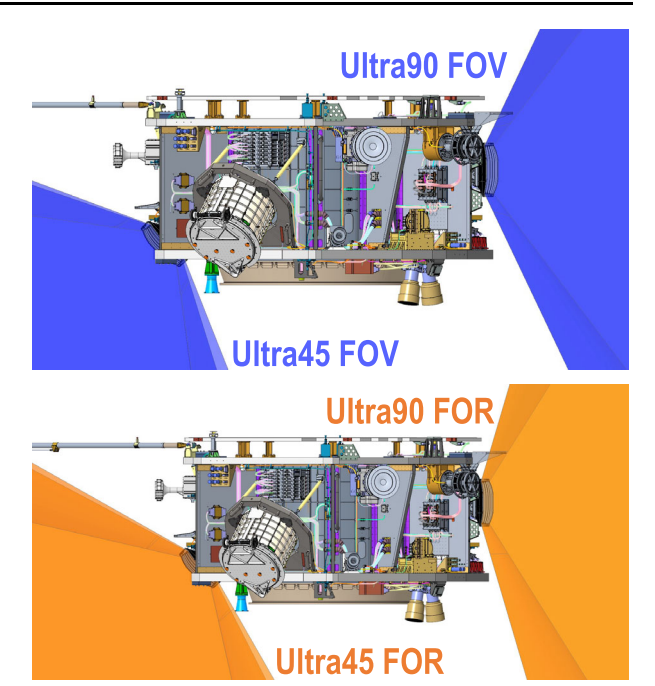
IMAP-Ultra comprises charged-particle deflection, variable apertures, a foil-based TOF microchannel plate imager (MCPs), and solid-state detector (SSD) energy subsystems. The two copies of IMAP-Ultra are mounted on the spacecraft with different orientations to optimize the viewing coverage. One IMAP-Ultra is mounted at 45° from the anti-sunward spin axis and the other is mounted at 90° from this spin axis. Ultra90 observes from 45° to 135° from the Sun, while Ultra45 observes the full anti-sunward hemisphere; together Ultra90 and Ultra45 cover  $\sim 3\pi$  sr over each spin (Fig. 30).

Each IMAP-Ultra imager has two identical entrances composed of a deflection system, variable aperture (VA), and start foil. Particles (Fig. 31a, purple trajectory) enter the deflection system, where the strong electric field between alternating grounded and HV (up to 8 kV) plates deflects charged particles into the serrated plate surfaces, effectively eliminating their forward scattering. This way the incident flux of ions and electrons is reduced below the nominal rejection energy (300 keV/q for 8 kV) by  $\sim 10^4$  and  $\sim 100$ , respectively, enabling clean (undeflected) ENA images. ENAs then pass through a stepper motor-driven VA, which provides a variety of aperture configurations, with different sensitivities and angular resolutions, with or without additional UV filtering (provided by a 5  $\mu$ g cm<sup>-2</sup> Si and polyimide foil). The ENAs enter the detector through the start foil ( $\sim 1~\mu$ g cm<sup>-2</sup> C foil that runs over the length of the entrance slit) producing secondary electrons. Shaped electrodes generate the electric fields (Fig. 31a, red potential contours) to accelerate and steer the secondary electrons (Fig. 31a, green trajectories) into the Start MCP, producing both 1D Start



100 Page 48 of 82 D.J. McComas et al.

Fig. 30 Ultra90 and Ultra45 mounted on the spacecraft. Blue shading depicts the FOV, and orange shading the FOR. The two sensors together cover  $\sim 3\pi$  sr of the sky per spin



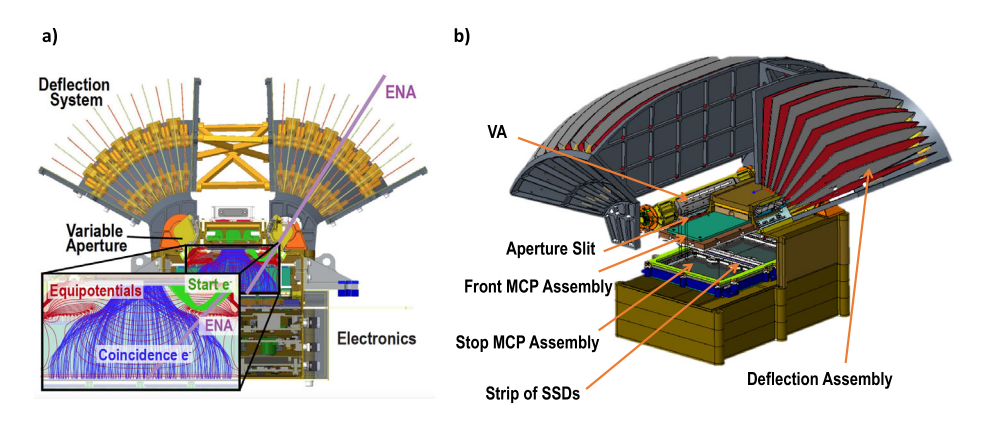


**Fig. 31** (a) IMAP-Ultra cross-sectional view showing trajectories of particles within the sensor; (b) IMAP-Ultra major elements: charged-particle deflection plates; front MCP assembly with two 1D start anodes servicing two entrance slits, and one 1D coincidence anode; variable aperture mechanisms servicing each entrance slit (detailed in inset); two stop MCPs imaged using 2D anodes; and a strip of SSD detectors between the two stop MCPs

position and Start timing. The particle continues through the sensor to the back plane, where it passes through an 8  $\mu$ g cm<sup>-2</sup> UV-filtering foil and strikes the Stop MCP, producing both 2D Stop position and Stop timing. Both Start and Stop anodes use time-delay to identify position to 1 mm spatial resolution, required for the finest angular resolution of 2°. The combined Start–Stop positions determine the ENA trajectory and combined with TOF, determine its velocity. The Stop MCP also records pulse height, which, with the TOF, yields a rough determination of particle species: light (e.g. H, He) or heavy (e.g., O, Ne, Fe). Sec-



Table 12 IMAP-Ultra instrument performance parameters for each sensor

Parameter	Performance	
Instrument Type	Slit-Based ENA Imager	
Number of Sensors	2 (Ultra-45, Ultra-90)	
Species	Neutrals, ions	
Energy Range	3–300 keV (H), 3 keV – 5 MeV (ions) (TOF-only, i.e. MCPs); 35–x (H), 60–x (He), 80–x (O) (TOFxE, i.e. SSDs), where x = 300 keV/c neutrals, 5 MeV ions; 30–700 keV (electrons, SSD-only)	
Energy Resolution ( $\Delta E/E$ )	12%–21% (intrinsic resolution).	
	Note: sky maps will be binned in $\sim$ 40% $\Delta$ E/E to optimize SNR.	
Angular Resolution	$\leq 6^{\circ}$ at $\geq 10$ keV H	
Field of View	MCPs: $\sim 96^{\circ} \times 120^{\circ}$	
	SSDs: $\sim 70^{\circ} \times 120^{\circ}$	
GF (cm <sup>2</sup> sr)	MCPs: $0.006$ (pinhole), $0.12-0.15$ (narrow slit), $0.6$ (wide slit) resolution	
	SSDs: 0.0006 (pinhole), 0.015 (narrow slit), 0.06 (wide slit)	
Signal to Noise Ratio	$\sim$ 20 (40 keV) – $\sim$ 180 (5 keV) for the low intensity regions in the sky	
Mass (per sensor)	7.66 kg	
Volume (per sensor)	$454 \text{ mm (L)} \times 359 \text{ mm (W)} \times 283 \text{ mm (H)}$	
Power (per sensor)	8.92 W	
Telemetry (per sensor)	1530 bps	

ondary electrons backscattered from the Stop MCP foil are accelerated and guided by the electrostatic potentials onto the coincidence region of the start-coincidence MCP (Fig. 31a, blue trajectories). The event logic requires that the coincidence pulse follow the stop pulse within a tight valid event coincidence time window (MCP TOF-only mode). A row of SSD detectors also located at the back plane, between the two stop MCPs, records the energy deposited for  $\geq$ 30 keV hydrogen particles that hit them. The energy deposited on an SSD, together with TOF derived from the Start time and an SSD Stop taken from the SSD portion of the coincidence anode, yields a so-called TOFxE measurement, sufficient to identify the particle species (H, He, O, Ne, or Fe).

Measurement requirements and instrument performance are summarized in Table 12. IMAP-Ultra angular resolution is energy dependent, and, over subsets of the FOV, it achieves the  $\leq 6^{\circ}$  angular resolution for  $\geq 10$  keV H (overlapping with IMAP-Hi), and down to  $2^{\circ}$  angular resolution above 30 keV. Full-sky maps of ENA H from 3 to 300 keV are produced over 3 months. As mentioned above, IMAP-Ultra eliminates UV background through tight coincidence timing and position logic. Triple coincidence logic reduces accidental coincidence rates to orders of magnitude below foreground counting rates. SNR calculations, using the efficiencies derived from the IMAP-Ultra calibration campaigns, and observed ENA spectra from IBEX and INCA indicate that for an input intensity of 0.2 cm $^{-2}$  s $^{-1}$  sr $^{-1}$  keV $^{-1}$  of 10 keV H $_{-}$  representative of the regions in the sky with the lowest heliospheric ENA intensity  $_{-}$  the SNR should be  $\sim 180$ , that is exceeding the IMAP requirement for that particular intensity and energy (i.e. SNR  $_{-}$  20). IMAP-Ultra also achieves favorable SNRs ( $\geq 10$ ) for ENA energies up to 40 keV (which is the required energy range).



100 Page 50 of 82 D.J. McComas et al.

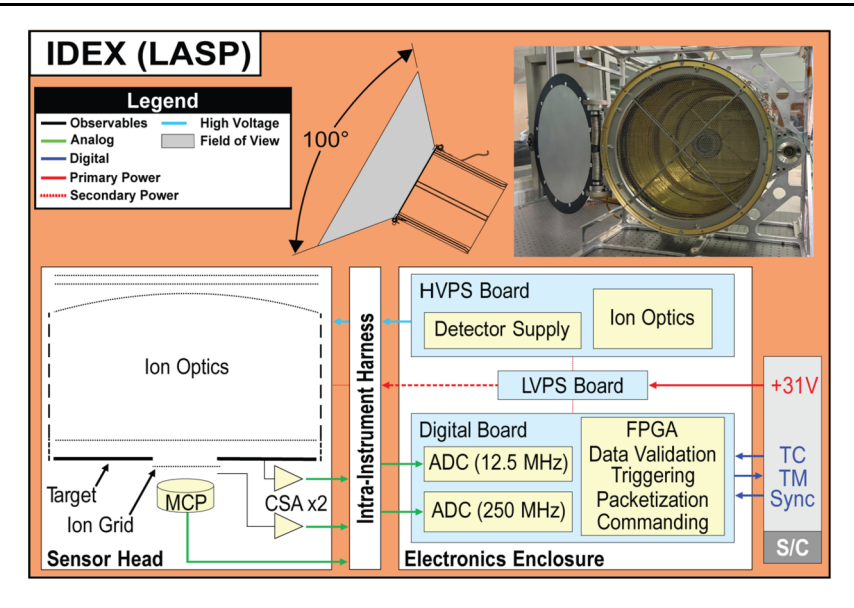


Fig. 32 IMAP's Interstellar Dust Experiment (IDEX) block diagram, and an image of its flight model

#### **4.9 IDEX**

The Interstellar Dust Experiment (IDEX; Horányi et al. 2025) is an impact ionization-time of flight mass spectrometer measuring the elemental and isotopic composition and the variability of the flux and size distributions of ISD and interplanetary dust particles (IDPs). ISD represents only about 1% of the mass in the interstellar medium. Still, it plays a critical role in its composition and energetics by enabling surface chemistry, absorbing stellar ultraviolet, and emitting infrared radiation (Draine 2011). IDEX observations link the interstellar gas phase composition measurements by IMAP-Lo and the PUI measurements by CoDICE and SWAPI with the composition of ISD particles. Hence, it contributes to IMAP Science Objective 1 (Sect. 1 and Tables 2 and 3 above), which is to improve our understanding of the composition and properties of the local interstellar medium.

IDEX is optimized for the detection and analysis of ISD particles, and its effective target area is sized for their low fluxes. IDEX also measures IDPs of cometary and asteroidal origin. The measurement principle is based on the impact ionization of the dust particles upon striking the target surface. Dust mass and impact velocity are determined from the characteristics of the impact charge, and composition is measured by analyzing the ions from the impact plasma. The IDEX detector and electronics are designed to cover the large dynamic range of the impact charges given by the expected mass and velocity ranges of the detected particles. The dust composition is measured by the TOF analysis of the atomic and molecular ions extracted from the impact plasma. The IDEX ion optics is derived from a series of prototype laboratory instruments with demonstrated performance (Rachev et al. 2004; Srama et al. 2004; Sternovsky et al. 2007, 2011, 2015). IDEX operates with a high mass resolution and dynamic range, and is capable of resolving the composition of the particles with a sensitivity better than 1% in relative abundance.

The design and operation principle of IDEX is similar to the recently developed Surface Dust Analyzer (SUDA) instrument for NASA's Europa Clipper Mission, and the IDEX subsystems derive heritage from those of SUDA (Kempf et al. 2025). Figure 32 shows IDEX's



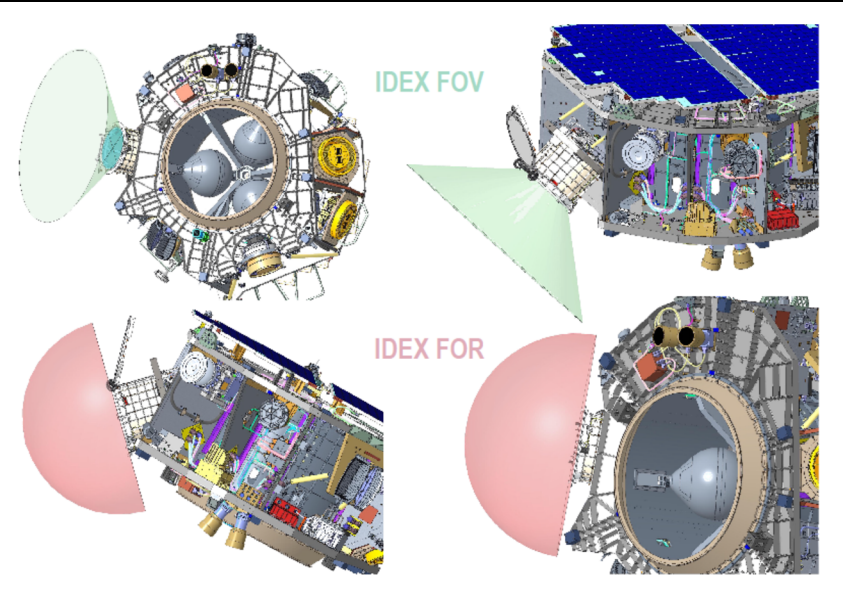


Fig. 33 IDEX's accommodation, FOV and FOR on IMAP

 Table 13
 IDEX instrument performance parameters

Parameter	Value	
Instrument Type	Impact Ionization Time of Flight Dust Composition Analyzer	
Effective target area	$638 \text{ cm}^2$	
FOV	50° (half angle) cone	
Dust mass	$2 \times 10^{-16} - 5 \times 10^{-14} \mathrm{kg}$	
Dust speed	30 – 55 km/s	
Composition mass range	1 – 286 amu	
TOF mass resolution	$m/\Delta m > 180 @ 56 amu$	
Mass	21.2 kg	
Volume	Cylindrical volume (door closed) D: 22 in and H: 24 in	
Power	16.4 W (Science) 8.9 W (Idle) 57.2 W (Decontamination)	
Telemetry	257 bps (350 events per week plus housekeeping packets)	

block diagram, and an image of the flight model of the instrument. The instrument consists of the Sensor Head and the Electronics Box. The latter houses the LVPS, the HVPS, and the PB. IDEX has a one-time deployable door that protects the instrument from particulate and molecular contamination, given its large and open aperture design. The instrument is mounted at 135° from the +z (Sun pointing) spin axis and thus the Sun, the solar UV radiation and solar wind ions are excluded from entering the aperture. IDEX is designed to maximize the detection of ISD particles on IMAP's spinning platform and is expected to detect about 100 ISD particles per year averaged over the solar cycle (fewer near maximum and more near minimum). The instrument's large target area and field-of-view enables scanning the entire anti-Sun hemisphere with each spin of the spacecraft (Fig. 33). IDEX's key instrument parameters are summarized in Table 13.



100 Page 52 of 82 D.J. McComas et al.

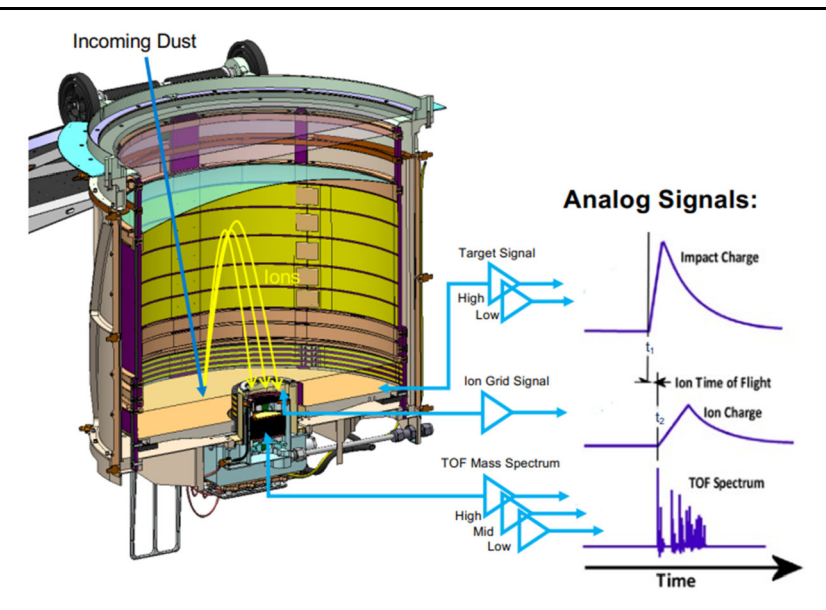


Fig. 34 Cut-away schematic view of IDEX shows its principle of operation

Figure 34 shows the cut-away schematic view of IDEX and its principle of operation. Individual dust particles enter the instrument and pass through a set of high open area grid electrodes and impact the target. Upon impact, the particle generates a partially ionized plasma plume on a positively biased target (+2.5 kV). The target recollects the electrons and anions from the impact plasma, and this charge is measured using a charge sensitive amplifier (CSA). The cations are accelerated away from the target and follow ballistic trajectories within the ion optics region. The reflectron-type ion optics design consists of a set of biased ring electrodes and a curved grid electrode, which focus the ions onto the central detector. An additional grid electrode in front of the detector is connected to a CSA and measures the integrated ion flux. This signal is also used for monitoring the gain of the detector throughout the mission. The ion detector measuring the compositional mass spectrum is a discrete dynode electron multiplier that enables operation over a large range of impact plasma charges. IDEX is an event-driven instrument, where the detector and/or the target signals are used to trigger data acquisition. Each dust impact event generates a record with a timestamp and six waveforms, which include the target signal measured with two different gains, the ion grid signal, and the TOF signal recorded with three different gains. Combined, the target and ion grid signals, and the three TOF waveforms cover a large dynamic range that enables the detection and analysis of particles over the expected mass and velocity ranges. The recorded high-resolution TOF spectra allows determination of the elemental composition of the impacting particle, provides information on their chemical composition and mineralogical makeup, and can identify the presence of organic compounds.

To measure the composition of ISD and IDP with high fidelity, IDEX follows strict contamination-controlled procedures. IDEX's gold target and its ion detector are sensitive to particulate and molecular contamination. IDEX has a one-time deployable door that minimizes the risk of such contamination during transport, integration, launch, and spacecraft outgassing in the early stages of commissioning. IDEX remains under continuous GN2 purge that is maintained until launch. IDEX also implemented a witness plate program to monitor its cleanliness through all phases of development, environmental testing, tests and



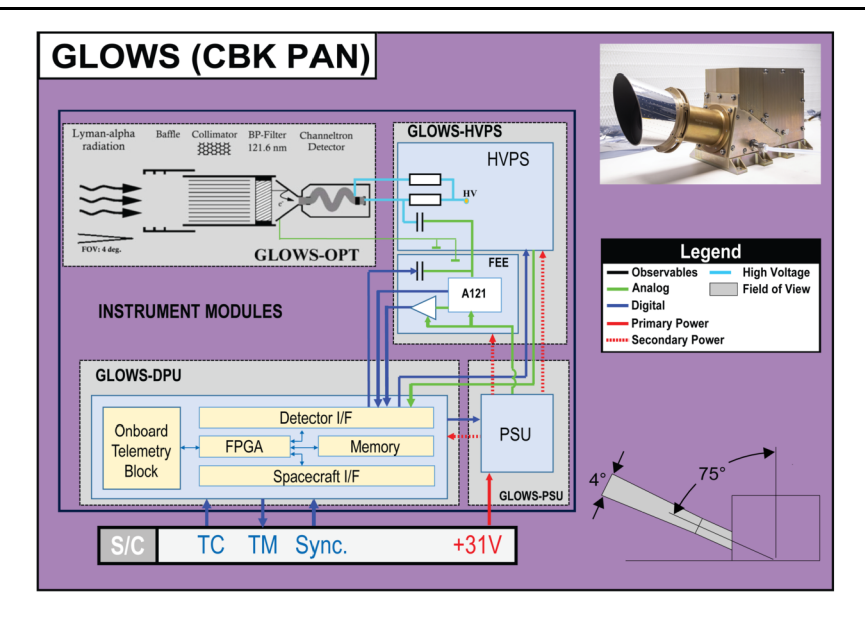


Fig. 35 Overall GLOWS instrument design and major subsystems

calibrations using a dust accelerator facility, transport, and integration. The last of these plates were removed during the last opportunity to access IDEX before launch. The plates were gold plated simultaneously with the target itself and were examined before and after removal from IDEX using TOF secondary ion mass spectrometry measurements. In addition, to minimize the possible cumulative effects from spacecraft outgassing and dust impacts, IDEX has a built-in bakeout capability for decontaminating the target surface. The bakeout procedure is exercised periodically in space to remove the volatile residue that may condense on the target.

#### **4.10 GLOWS**

GLOWS (Bzowski et al. 2025; Fig. 35; Table 14) is a Lyman- $\alpha$  ( $\sim$ 121.5 Å for H) photometer that measures daily light curves of the heliospheric hydrogen backscatter glow along Suncentered rings in the sky, enabling the instrument to address IMAP Science Objectives 1 and 2 (Sect. 1 and Tables 2 and 3 above). The "helioglow" is an emission of ISN H atoms inside the heliosphere, excited by the Lyman- $\alpha$  radiation from the Sun. Analysis of these light curves provides heliolatitudinal profiles of the ionization rate of ISN H. These latter profiles are subsequently decomposed into the profiles of photoionization and charge-exchange rates of ISN H, and the latter of these into profiles of 3-D solar wind speed and density. These profiles are used to calculate survival probabilities of ENAs observed by IMAP. The distribution of the density of interstellar hydrogen within a few au from the Sun is governed by solar radiation pressure and ionization by charge exchange with solar wind protons and photoionization. The rate of the charge exchange reaction varies with the proton density and collision speed with interstellar H atoms. The density and speed of the solar wind are functions of heliolatitude (McComas et al. 1998a), which vary over the solar cycle and longer timescales (McComas et al. 2008b; Sokół et al. 2013; Porowski et al. 2022). Thus, the density of ISN H is latitudinally structured, which is reflected in the latitudinal distribution of



Table 14 GLOWS performance parameters

Parameter	Performance	
Instrument type	Lyman-α single-pixel photometer	
Species observed	Hydrogen helioglow Sun-centered light curves	
Waveband	$120.5~\mathrm{nm}\pm4.2~\mathrm{nm}$	
Scanning circle radius	75°	
Sensitivity	3.37 cps/Rayleigh	
Total mass	3.70 kg	
Dimensions	$380 \text{ mm (L)} \times 165 \text{ mm (H)} \times 132 \text{ mm (W)}$	
Total power	5.1 W	
Usable HV range	1500 – 2500 V	
Total downlink rate	1200 bps	
Sampling resolution	3600 bins	
Science light curve resolution	4°	

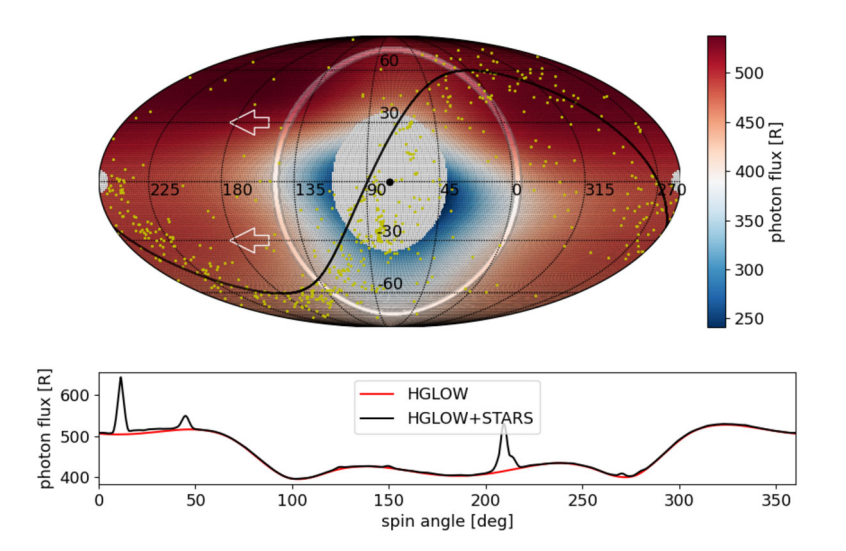


**Fig. 36** GLOWS scanning circle superimposed on a sky map of simulated helioglow (Kubiak et al. 2021) and extraheliospheric sources (upper panel) and the resulting light curve (lower panel). The scanning circle is illustrated as a bright narrow band, centered 4° off the Sun. The black line represents the galactic equator. The red line in the lower panel shows the helioglow, and the black line the contributions from the helioglow and extraheliospheric sources combined

the helioglow. Other sources of the signal measured by GLOWS include EUV-bright celestial objects (mostly stars and the Milky Way), and transient phenomena (including comets, Jupiter, and Saturn).

GLOWS draws from the heritage of the LAD instrument (Nass et al. 2006) on the NASA TWINS mission (McComas et al. 2009c). Main drivers for the GLOWS design were: 1) maximizing the amplitude of the helioglow modulation due to the solar wind structure relative to the backgrounds, and 2) appropriate suppression of stray light from the outside of the desired field of view. Maximization of the solar wind-modulation amplitude is achieved by selection of the radius of the scanning circle, optimized at 75° (Fig. 36), and the application



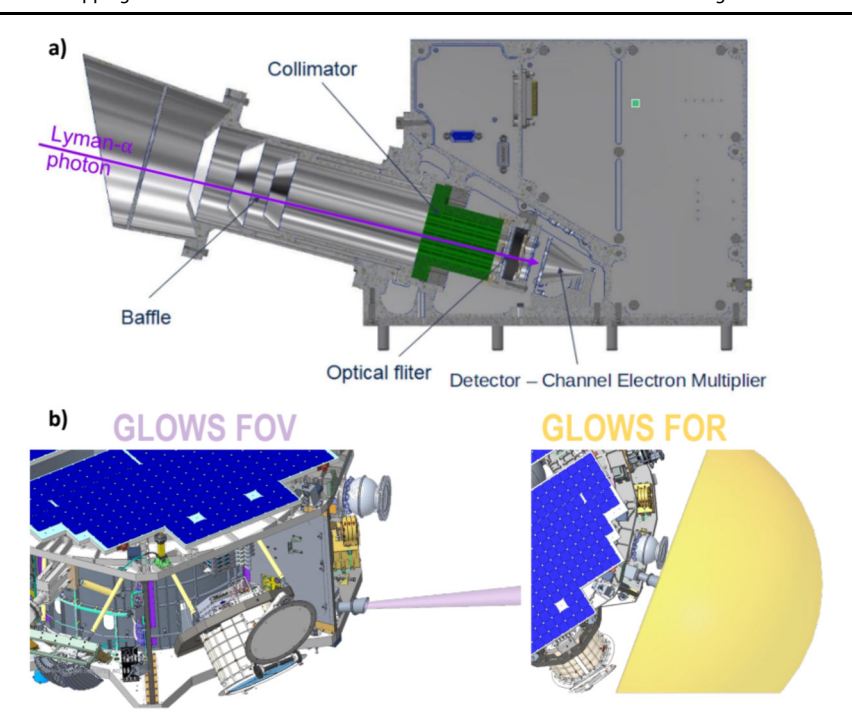


Fig. 37 Diagram of the GLOWS optical entrance system and the CEM detector (top) and of the field of view (lower left) and field of regard (lower right)

of a narrow-band interference filter at the bottom of the collimator. This is possible because the helioglow is practically monochromatic and the stars and Milky Way have broad spectra, so it is possible to filter out most of the emissions from the latter with much less suppression of the former. The spectral width of the filter convolved with the spectral efficiency of the light-sensitive detector provides the spectral width of the GLOWS entrance system of 8.5 nm, centered at 120.5 nm wavelength. This results in suppression of the sky background to the level comparable to the expected statistical scatter of the daily light curves. An exception is a band within several degrees around the Galactic equator, which is masked in the analysis. Simultaneously, calibration stars are still visible against the helioglow. Suppression of the aforementioned stray light is achieved by appropriate design of the optical entrance system, composed of the collimator, which defines the baseline circular field of view of 4.2° FWHM, and the baffle with a sunshield, which cuts out stray light.

Successful retrieval of the solar wind profiles does not require a precise photometric calibration of the instrument but does require tracking changes of the instrument's sensitivity during the mission. Calibration tracking is accomplished by observation of Lyman- $\alpha$  bright stars. Each of the relevant stars is observed twice during the year. The instrument radius and light curve binning scheme have been chosen so that the stars pass across the FOV during intervals of several consecutive days. This enables assessment of their absolute brightness even though the stars are not expected to pass precisely through the center of the FOV.

GLOWS is a photon counting instrument (Fig. 37). The light-sensitive element is a CEM, which converts a single photon into a large cascade of electrons. These cascades are accelerated and multiplied by high voltage applied to the CEM, which is provided by the GLOWS



HVPS. A charge impulse is detected by the FEE and converted into a DE. This DE is handed over to the DPU, which attaches a time stamp to each DE.

These DEs are histogrammed into IMAP spin angle bins. GLOWS uses 3600 bins – this resolution was selected to facilitate identification and masking or subtraction of stars in the light curves. Binning direct events requires precise information on the IMAP rotation phase. Observations are performed in 8-spin blocks. Thus, GLOWS provides a light curve approximately every 2 minutes. This facilitates rejection of background intervals in the ground processing should they be detected during a given spin axis pointing. These 8-spin histograms are put into the telemetry as the main science data product. In the ground data pipeline, they are filtered against bad times and masked to eliminate the unwanted contribution from stars and the Milky Way. After masking, the light curves are stacked into daily-averaged light curves and re-binned into 90 bins covering the full scanning circle.

Subsequently, daily light curves are processed to retrieve latitudinal profiles of the ionization rate of ISN H. Retrieval of the ionization rate profiles is performed using a machine-learning method developed by Porowski and Bzowski (2024). These rates are valid for atoms traveling at low speeds relative to the Sun, characteristic of interstellar gas. The daily ionization rates are subsequently filtered and averaged by Carrington rotation (CR) periods. The CR-averaged ionization rates are decomposed into the photoionization rate using measurements of the F10.7 radio flux (Tapping 2013; Sokół et al. 2020) and charge exchange rate in the stationary atom approximation.

The charge exchange profile is decomposed into the profiles of solar wind speed and density, using the assumption that the total energy flux of the solar wind is latitudinally invariant (Le Chat et al. 2012). A long-time average of this invariant is obtained from the OMNI2 data collection and directly with SWAPI in-situ observations on IMAP (Rankin et al. 2025). Decomposition into the speed and density is obtained by numerical solution of the charge-exchange equation, with the charge exchange cross section adopted from Swaczyna et al. (2025). The Carrington period-averaged profiles of the solar wind speed and density are another data product of GLOWS.

As the last phase of the processing, the profiles of the solar wind speed and density, as well as the photoionization rates are used to calculate survival probabilities for ENAs observed by IMAP. The probabilities are calculated in the IMAP inertial reference frame. The calculations are performed for the scanning circles of IMAP-Lo, IMAP-Hi45 and IMAP-Hi90 at a coordinated, logarithmically-spaced energy grid. Additionally, survival probability maps are calculated on a HealPix grid (Górski et al. 2005) for the portions of the sky viewed during a given spin axis pointing by IMAP-Ultra. Calculation of survival probabilities is performed based on the theory developed by Bzowski (2008) the calculation system is an adaptation of that successfully used for IBEX.

# 5 Spacecraft and Mission Design

To achieve the desired L1 orbit, IMAP launched on a SpaceX Falcon 9 launch vehicle into a near-escape trajectory towards L1 (C3  $\leq$  -0.50 km<sup>2</sup> s<sup>-2</sup>) from Cape Canaveral Space Force Station. The launch vehicle achieved a low earth parking orbit and remained there until reaching the proper location for the transfer trajectory insertion (TTI) maneuver. The coast duration of the parking orbit varies seasonally as well as with the choice of ascending or descending node TTI. During coast periods when the Sun was present, the launch vehicle pointed the +Z-axis of the IMAP spacecraft within 22° of the Sun to ensure IDEX and



100

IMAP-Lo did not have Sun exposure and maintained proper thermal management. Eclipse periods were powered by an onboard battery.

TTI was performed on the night side near local midnight. IMAP separated from the launch vehicle when the spacecraft was out of eclipse. Prior to separation, the launch vehicle pointed IMAP to the target release attitude (nominally 1.9° trailing the Sun), spin up to 4 rpm, and released IMAP. Post launch vehicle separation, a timer turned on the RF solid state power amplifier (SSPA) as soon as IMAP was far enough from the launch vehicle to safely transmit. Earth communication was established as soon as possible following SSPA power-on; this is immediate for most launch opportunities. Due to the required TTI conditions for an L1 transfer, the Swedish Space Corporation (SSC) is usually available prior to Deep Space Network (DSN). In either case, the first available network establishes initial communication.

After IMAP reached a safe distance, the launch vehicle then de-spun and maneuvered away from IMAP to ensure subsequent safe deployment of the two secondary payloads. Launch Phase ended once initial DSN contact was established on the medium gain antenna (MGA) and the spacecraft was promoted to operational mode. Due to the spacecraft-to-Earth geometry at separation and the location of the SSC stations relative to DSN, initial DSN contact on the MGA could have been as much as 125 minutes after separation depending on the actual launch date.

An initial trajectory correction maneuver (TCM) was carried out ∼36 hours after TTI to "clean up" any launch vehicle trajectory dispersions. Additional TCMs are performed as required prior to insertion into L1 orbit. During the  $\sim$ 3.6-month transfer both the spacecraft and instruments are commissioned and ready to begin science operations upon insertion into L1 orbit. The Lissajous Orbit Insertion (LOI) maneuver takes ~30 hours to achieve the desired Lissajous orbit. The trajectory from launch through the end of the baseline mission phase is illustrated in Fig. 38.

During normal operations, IMAP's spin axis (angular momentum vector) nominally points towards the incoming solar wind, approximately 4° ahead of the Sun relative to the Earth-Sun line. The angular momentum vector is inertially fixed, so it appears to slew from  $\sim 3.5^{\circ}$  to  $\sim 4.5^{\circ}$  ahead of the Sun each day, and each day the spacecraft uses the attitude control system (ACS) to repoint back to 3.5°. The repoint maneuvers are executed onboard via a time-tagged command with pointing parameters from an ACS table that is updated weekly. This pointing strategy optimizes the orientation of the solar wind measurements while minimizing solar wind backgrounds known from IBEX ENA observations. Because IMAP is a spinning spacecraft,  $\Delta V$  maneuvers are required to be performed in two components, an axial component and a radial component. The majority of TCMs are performed without adjusting the spacecraft attitude to align with the desired  $\Delta V$  vector for the maneuver. Because LOI is such a large burn, we treat it as a special case where spacecraft attitude is adjusted before and during the maneuver; this procedure saves as much as 10 m s<sup>-1</sup> of  $\Delta V$ . All spacecraft attitude adjustments are performed by the axial thrusters, in contrast to LOI  $\Delta V$ , which is performed on the radial thrusters. The burn sequence is segmented to never burn on both the axial and radial thrusters simultaneously. The angular momentum vector during the LOI maneuver remains within 22° of the Sun due to power, thermal, and instruments constraints.

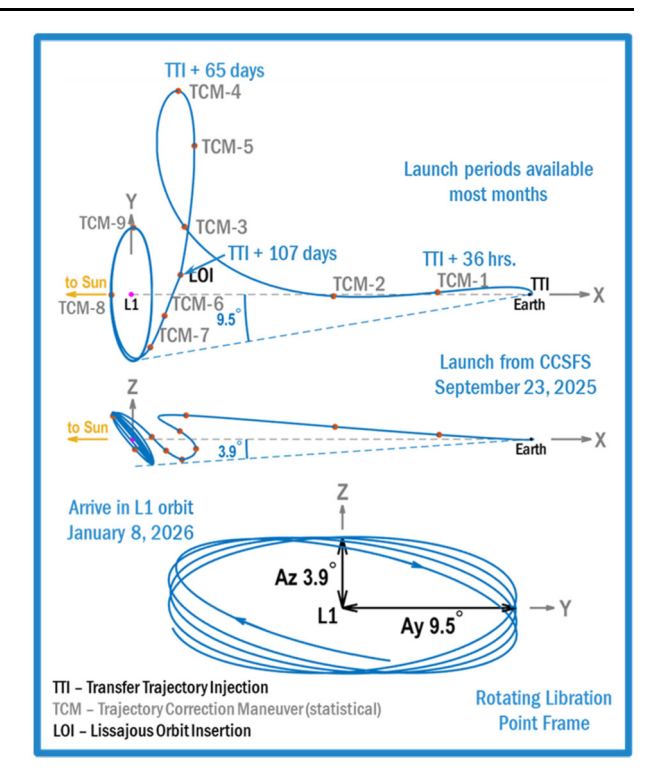
The IMAP observatory is shown in its deployed configuration in Fig. 39, and spacecraft components and instruments are indicated in Fig. 40. Instruments are mounted with their FOVs to take advantage of the observatory's nearly sun-pointed spin axis, as described in the instrument sections above.

The IMAP spacecraft leverages experience from recent and ongoing missions with a simple high-heritage design to provide a low-risk posture. The spacecraft accommodates the



100 Page 58 of 82 D.J. McComas et al.

Fig. 38 Nominal IMAP trajectory from launch through end of the Baseline Mission



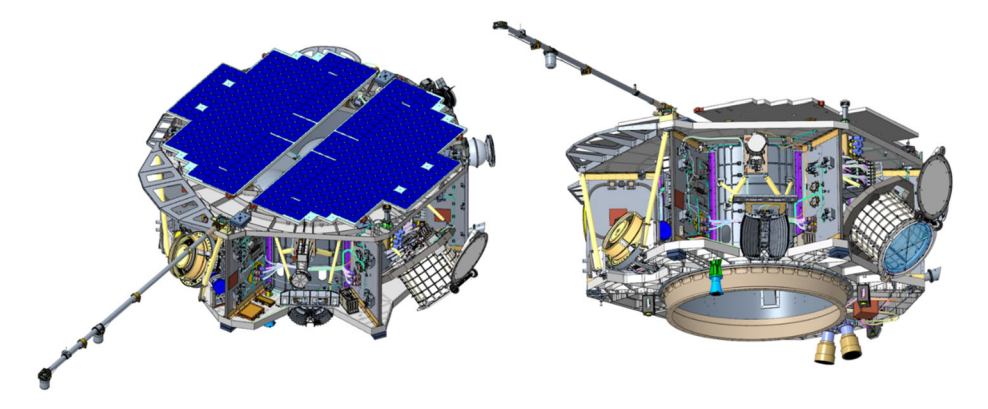


Fig. 39 IMAP shown in deployed configuration (thermal blankets removed)

IMAP instrument suite, providing the required mechanical, thermal, power, and data (command and telemetry) resources for the instruments while meeting the pointing requirements necessary for the instruments to achieve all their Science Objectives.

Figure 41 provides the observatory electrical block diagram. The instruments, described above, along with the spacecraft subsystems, are color-coded and show the various components and indicate the major power and data interfaces. The electrical architecture heavily leverages Parker Solar Probe (PSP; Fox et al. 2016) spacecraft subsystems, with minimal de-



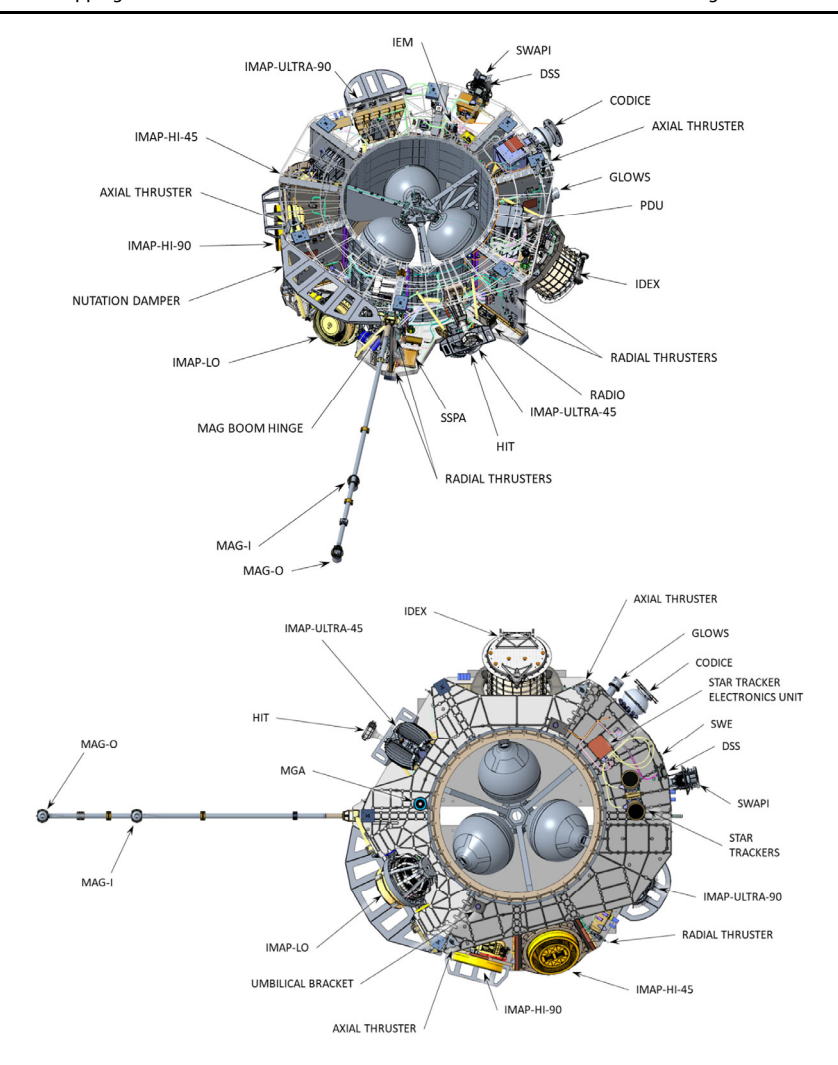


Fig. 40 IMAP instruments and spacecraft components as seen from the sunward side (top) and anti-sunward side (bottom) with the sunward surface mounted solar array removed to expose the various subsystems

sign changes, increasing build-to-print capability and allowing for potential re-use of available flight hardware.

The IMAP mechanical structure includes an aluminum central cylinder and top and bottom decks, aluminum honeycomb radial panels, open bays for the instruments, and accommodates a single deployable 2.5 m magnetometer boom. The layout provides clear FOVs for all instruments, thrusters, star tracker heads, and Sun sensor heads, as well as physical accommodation for all components and the required orientation of the instruments to collect their science measurements. Thermal control is maintained with MLI and thermostatically controlled heaters.

The attitude control subsystem includes simple onboard repointing capability, passive nutation damping with ring dampers, and maintains the observatory spin stabilization at  $\sim$ 4 rpm. TCMs to achieve L1 orbit insertion, station-keeping maneuvers to maintain the desired



100 Page 60 of 82 D.J. McComas et al.

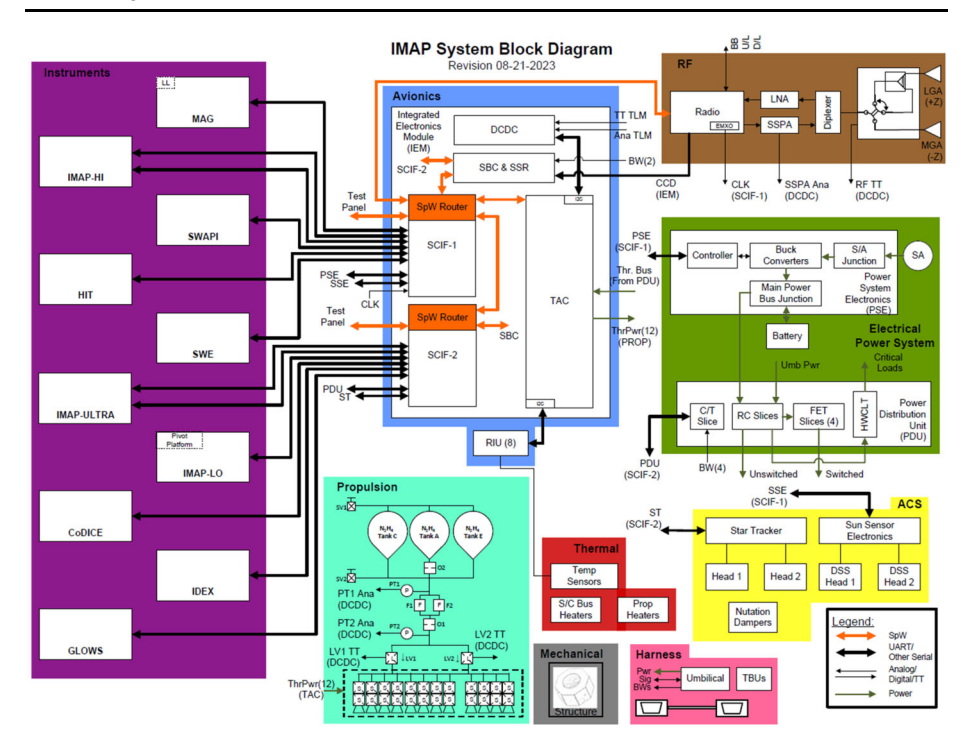


Fig. 41 IMAP Observatory electrical block diagram

orbit, and daily repointing maneuvers to follow the  $\sim 1^\circ$  day<sup>-1</sup> motion of the Earth and Sun are accommodated with a monopropellant hydrazine blow-down propulsion system with twelve 4 N thrusters and three conospherical tanks, using heritage from the ACE mission.

Power is provided through a 3.6 m<sup>2</sup> body-mounted solar array with 16 strings of triple junction GaAs based cells (36 cells per string), with a peak power tracking topology via the PSP heritage power system electronics. A 25 A-hr lithium-ion battery, which was build-to-print from the PSP battery, supports the observatory power requirements around launch. Throughout the rest of the IMAP mission, no battery is needed as the spacecraft remains power positive with its Sun-pointed solar array.

The telecommunications subsystem utilizes a Frontier Radio architecture with PSP heritage configured for X-band uplink and downlink with an 8 W SSPA. A fixed forward low gain antenna (LGA) and aft MGA support all IMAP communications. An LGA/MGA combination is used for the launch phase to support broadcasting initial separation. The configuration is then switched to the MGA-only for the remainder of the mission. The downlink capability accommodates both nominal transmission of spacecraft and instrument data to DSN during scheduled contact periods and otherwise continuous broadcast of lower rate I-ALiRT data.

The avionics subsystem provides the environment for the flight software (FSW). It contains a LEON3FT processor, non-volatile memory (to store the flight software images), RAM, a 256 Gbit flash recorder, SpaceWire network, and two spacecraft interface cards (SCIFs). The FSW architecture is heritage from PSP and based on the Goddard Space Flight Center (GSFC) core Flight Executive (cFE). It supports the observatory C&DH needs with heritage components from the PSP mission modified as necessary for IMAP. The PSP sin-



gle board computer (SBC) has been upgraded with new FPGA firmware and the operating system has been upgraded to improve processor utilization margin. Although mission data is required to be downlinked weekly, this recorder can store more than 20 weeks of science and housekeeping data.

Functions of the spacecraft C&DH Computer Software Configuration Item (CSCI) include uploading commands for the observatory using the CCSDS File Delivery Protocol (CFDP), executing those commands, collecting and storing spacecraft, instrument science and housekeeping data to the SSR, sending real-time spacecraft housekeeping and playback SSR data to the ground system, providing a time-based commanding capability, and providing an onboard autonomy engine with the ability to execute commands in response to fault conditions. The FSW uses a file system to manage data storage to and playback from a non-volatile flash device and uses the CFDP to downlink files to the ground system. In addition, the C&DH CSCI supports the assembly and broadcast of the I-ALiRT data.

IMAP Autonomy maximizes science availability and operational capability between ground contacts by utilizing a tiered fault response to contain localized faults. Since IMAP is spin-stabilized and operated in a continuous and fairly benign deep space environment at L1, the overall fault management architecture is simple and robust. IMAP Autonomy is a rule-based monitor  $\rightarrow$  response system where faults are detected and corrective actions taken. The majority of potential fault conditions are local and non-critical, and Autonomy responds while maintaining the observatory in Operational Mode. Critical faults are those that jeopardize observatory power production, power storage, or communications and require a time-sensitive transition to Safe Mode. As a clever multi-purpose use, a small amount of fault management information is included in the I-ALiRT packet to provide real-time fault status even when outside of nominal DSN contacts. A status bit for each instrument if the instrument is operational, and spacecraft status is provided in the form of the last autonomy rule fired and the total count of all fired rules. FSW merges the real-time space weather science packets with the autonomy and instrument status information into I-ALiRT packets that are transmitted at 2083 bps. The 2083 bps communication rate for I-ALiRT matches the spacecraft's emergency communication downlink rate, which is swapped in when the spacecraft is in Safe Mode. The I-ALiRT stations forward the downlinked frames to the SOC either way and the SOC relays Safe Mode data to the MOC, providing near-immediate notification of safe mode to the MOC.

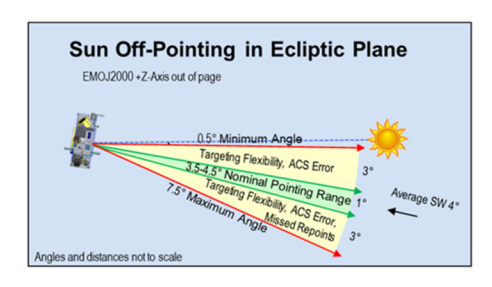
ACS functionality within the spacecraft C&DH CSCI computes spin phase using star tracker data and calculates and distributes the spacecraft clock time. Other ACS functionality implements  $\Delta V$  maneuvers based on ground software calculations and resultant spacecraft commands to control thruster burns. Repointing is performed using star tracker attitude knowledge and time-tagged commands to provide desired pointing vector and burn commands.

IMAP implements attitude control using its multi-head star tracker for attitude determination and the hydrazine thrusters to adjust spin-axis. This repointing occurs nominally at the same time every day and targets the angular momentum vector as described above. Repointing starts by setting a flag for the instruments in the Command ITF spacecraft Time and Status message. The time-tagged command sequence generated by mission operations sets the flag to one hour in advance of the event. The repointing thruster firings take less than two minutes, depending on the number of spins needed to complete the maneuver. After completion of thruster firings, the catalyst bed heaters are turned off and the event flag is set back to 0. This entire sequence is planned outside of ground contacts with occasional time tag command updates provided during normal contacts.

IMAP is designed to provide operational flexibility to target some variation in Sun offpointing, changes in repointing frequency, real-world dynamics, and ACS implementation



100 Page 62 of 82 D.J. McComas et al.



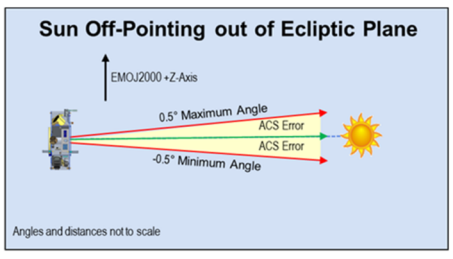


Fig. 42 IMAP spin-axis off-pointing range

errors. The range of allowable Sun off-pointing during science operations of the spin-axis in the ecliptic and out of the ecliptic plane is shown in Fig. 42.

The observatory budgets for up to 0.25° of coning due to misalignments between the principal axis of maximum moment of inertia and the spacecraft +Z axis and 0.25° of maximum nutation that may occur after the completion of a repointing event. Passive nutation dampers are included even though IMAP is designed to meet all of its measurement requirements immediately after the repointing event is completed and with the maximum budgeted nutation angle. Both coning and nutation were factored in the estimates of the observatory Z-axis maximum off-pointing to the Sun and Earth for solar array and RF design.

Because L1 is a gravitational saddle point between the Earth and the Sun, some station-keeping is required to maintain the desired orbit. The IMAP orbit design corrects for typical perturbations that slowly pull the spacecraft out of its Lissajous orbit. These small maneuvers may occur as frequently as every 1.5 months but require only  $\sim$ 4 m s<sup>-1</sup> annually. Each maneuver is performed while in ground contact with  $\sim$ 1 hour of catalyst bed warm-up and typically less than two minutes of thrust to complete the maneuver.

IMAP has budgeted station-keeping propellant for 5 years of operation (2 years baseline and an additional 3 years minimum for the first extended mission). In addition, extra propellant is carried for worst-case launch vehicle dispersions, which can be used to significantly extend the mission even longer for almost any actual launch performance. In addition, lessons learned from ACE show that periods of recurring low sun-Earth pointing angle are infrequent (once every several years), each possible outage only lasts for several days, and in the case of ACE did not impact communications due to robust RF link margins, also exist on IMAP. These, along with filling the propellant tanks beyond the required value with our remaining mass margin, and having a nominal launch, together ensure that IMAP can support several decades of extended science mission.

# 6 Operations, Data, CAVA, and Real-Time Space Weather

IMAP integrated operations are overseen by the Science and Mission Operations Lead (SMOL). Integrated operations are carried out through the MOC and the SOC. The MOC manages spacecraft operations, interfaces with the ground antenna networks, and acts as a "bent pipe," which forwards payload commands and data back and forth between the spacecraft and the SOC. The SOC is functionally split into two groups, the Payload Operations Center (POC) and the Science Data Center (SDC).

The POC manages payload operations, monitors the health and safety of the instruments, provides housekeeping quick look plots, and archives all downlinked products pulled from the IMAP Data Server. The POC works with the instrument teams to plan, constraint-check,



and command all payload operations. It coordinates payload response to anomalies and maintains a history of payload anomalies starting from observatory integration. The SDC provides a centralized data system for all Level 0 – Level 3 science data processing, distribution, and archiving. It also maintains data processing software, data products, and ancillary data. Finally, CAVA provides our science analyzing platform for combining and analyzing IMAP data across all instruments and being able to efficiently pursue IMAP's integrative science analysis and studies.

#### 6.1 Science Data

IMAP's innovative approach to building a unified payload data processing pipeline, which was verified before launch, enables the science team and the larger science community to publish data quickly without the inefficiencies and delays seen in other missions. Before launch, the instrument teams and integrated mission groups, like the "imaging working group," provided algorithms, documentation, and calibration information to the SDC, who used these inputs to write the Level 0 – Level 2 data processing software. These same groups worked with Menlo Innovations, who wrote the Level 3 and the CAVA data processing software (see below). The instrument teams, integrated mission groups, SDC, and Menlo Innovations collaborated to verify the data pipeline and validate the data products before launch.

The IMAP science data flow is shown in Fig. 43. All IMAP telemetry and data is downlinked via NASA's DSN to the MOC and placed on the IMAP Data Server. Following each contact, the POC automatically pulls the instrument data and a subset of spacecraft telemetry and ancillary data, making it immediately available to both the instrument teams and the SDC pipeline. The SDC processes Level 0 – Level 3 science data, which includes data calibration, initial (automated) validation, and preliminary analysis. The processed science data and ancillary data are available to the instrument teams through the team website and the CAVA platform.

I-ALiRT data follows a different data path. When IMAP is not in DSN contact, the space-craft continuously broadcasts space weather data, which is collected by international partner antenna sites and transmitted directly to the SOC. The SDC is responsible for the near-real-time (less than 5-minute latency) processing of this continuous stream of I-ALiRT data immediately upon receipt. Importantly, the SDC also distributes IMAP data to the science community via a public website and delivers the Level 0 – Level 3 data products, ancillary data, software, and documentation to the Space Physics Data Facility (SPDF) for long-term archival.

IMAP Science Data Levels are defined as follows. Level 0 data are binary CCSDS packets containing unprocessed data with communications artifacts removed. Level 1A data are fully decommutated but uncalibrated full resolution, time-referenced raw data and extracted housekeeping telemetry. Level 1B data have engineering and initial instrument-level science calibrations applied and are annotated with ancillary information (e.g., ephemeris, attitude, etc.). Level 2 data have been processed into physical units by combining calibration, ancillary, and other data. These represent the lowest level of research-grade scientific data and are at the same temporal and/or spatial resolution as the Level 1 data. Finally, Level 3 data have been resampled spatially or temporally and may have been combined with measurements from other instruments to produce a merged data set (e.g., pitch angles and combined ENA maps).

The SDC carries out our science data processing and distribution (Fig. 44). Once the POC pulls files from the MOC data server, they are immediately available to the SDC data



100 Page 64 of 82 D.J. McComas et al.

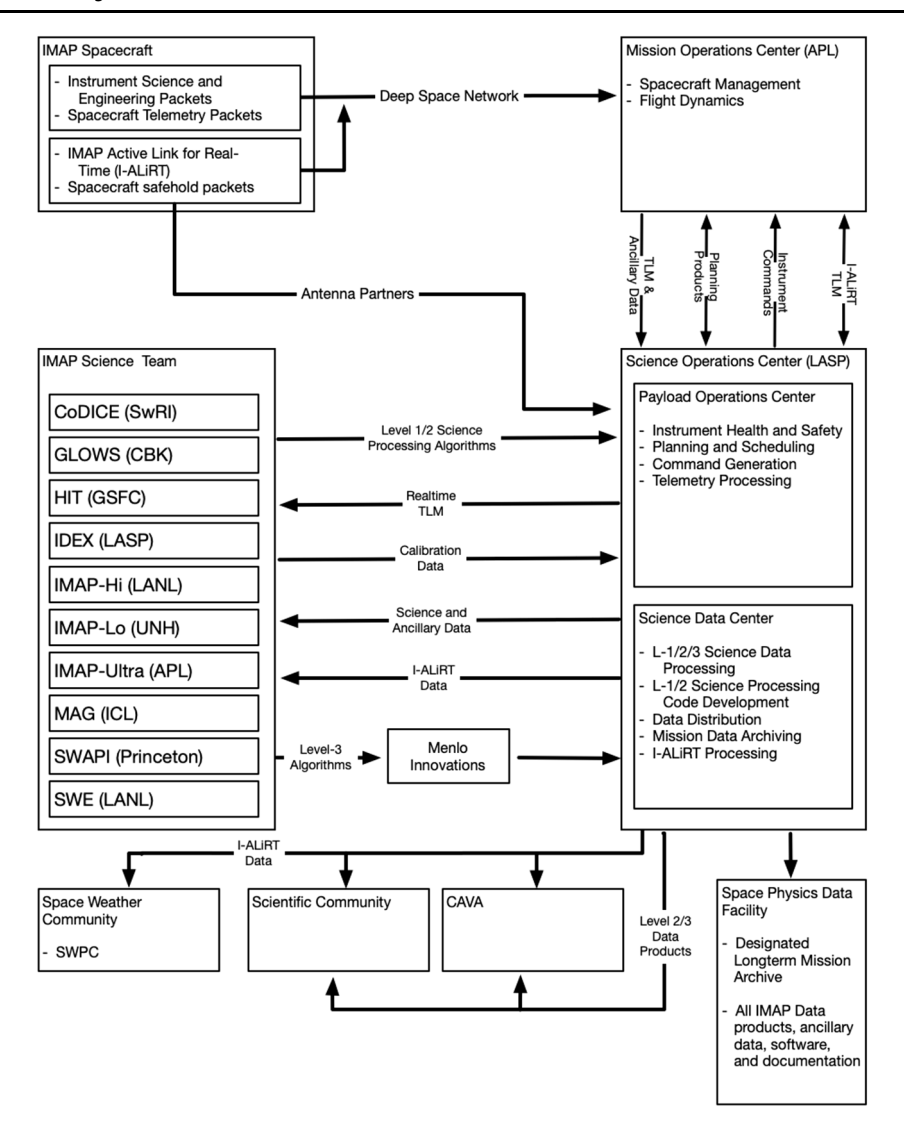


Fig. 43 IMAP science data flow

pipeline, which processes the Level 0 into Level 1 data products. Higher-level data products are automatically processed as soon as all necessary inputs are available to the processing pipeline. This processing includes data calibration, validation and preliminary analysis.

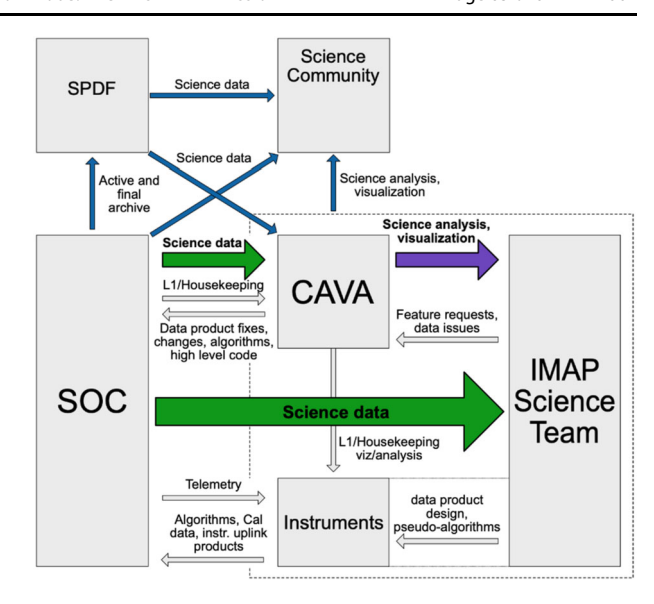
The SOC also includes a real-time data processing pipeline consisting of three parts:

1) pre-processing software to extract the data during DSN tracks, 2) software to execute algorithms provided by the instrument teams to generate data products, and 3) software to publish the products to the IMAP Science Gateway.

The SDC has a cloud-based architecture deployed in Amazon Web Services (AWS), and maintains version-controlled software to ensure that changes in the processing pipeline and associated data products are tracked and transparent to scientific users. If any changes in the processing system generate different data values for the same time period, the version of that



Fig. 44 IMAP science data processing and distribution flow



data product is incremented and a new DOI registered. This includes changes to software or calibration data that affect science data and/or version changes for an upstream data product. For clarity and consistency, version numbers are included in data product file names.

The SDC maintains an active archive of all IMAP data levels and provides direct access to the IMAP Science Team and broader science community. The SPDF is the long-term data archive for IMAP data and will make IMAP data available through their Coordinated Data Analysis Web (CDAWeb) site. All IMAP data products follow the current Common Data Format (CDF) standards to ensure consistency across missions. The SDC dedicates significant attention to following these standards to ensure each data file contains the necessary information for knowledgeable data analysis, ideally using IMAP SDC or CAVA plotting tools.

The SDC also maintains the IMAP Project Science Office Calibration and Measurement Algorithms Document (CMAD, see Supplementary File) and sends the IDEX data to the Planetary Data System (PDS) for parallel archiving. IMAP is compliant with the NASA Heliophysics Science Data Management Policy and shares all science, software, and associated data with the Heliophysics community as quickly as practical.

#### 6.2 CAVA

CAVA, the Combined Analysis, Visualization, and Access tool, is a software tool for the interactive analysis and visualization of science data from IMAP. To support the sort of multi-instrument, integrative science that the IMAP mission is designed to do, the IMAP team developed the comprehensive visualization and analysis tool CAVA in Python, which is deployed as a desktop application. The result is an interactive tool that leverages the IMAP datasets to efficiently advance the frontiers of Heliophysics.

The goal of CAVA is to enable the entire IMAP mission team to access, analyze, and visualize IMAP's ten instrument datasets without ever needing to write significant code or directly understand the exact file formats in which the IMAP data is stored. By building a new tool designed specifically for the IMAP mission, this also provides the opportunity to focus on user experience and optimize for tool usability, performance, and maintainability.



100 Page 66 of 82 D.J. McComas et al.

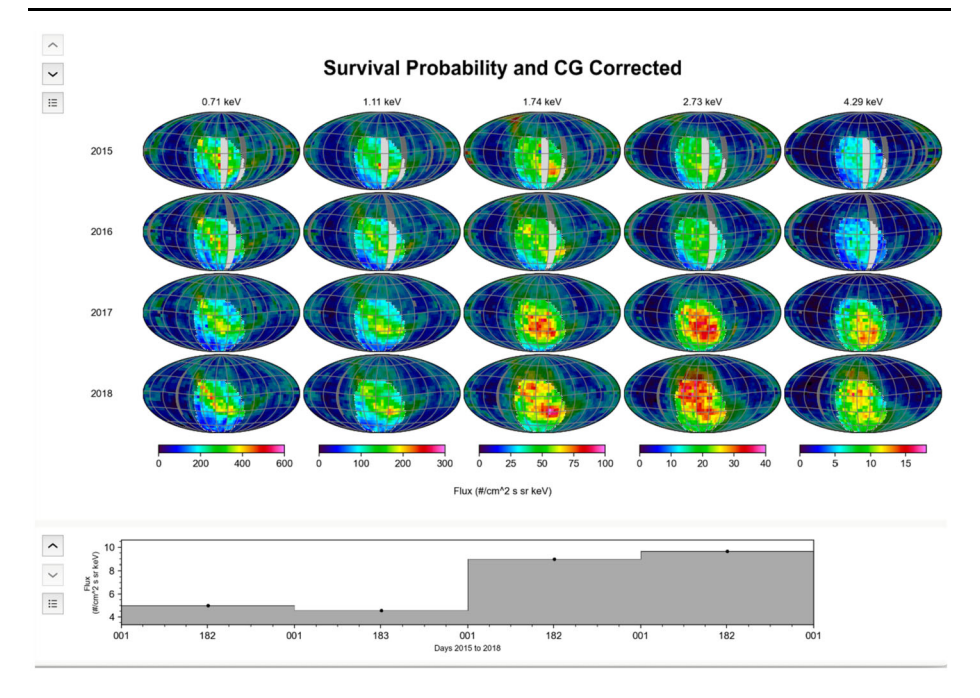


**Fig. 45** CAVA example showing the display of heritage IBEX dataset maps from 2015 to 2018. Time series at the bottom shows the average intensity in the manually selected region (brighter pixels in the maps) over time

Prior multi-instrument missions have typically launched without comprehensive visualization tools to analyze the scientific data collected. For those missions, analyzing multiple instrument datasets required significant familiarity with individual instrument data files and associated instrument-specific formatting of relevant data products, as well as the expertise to develop very specific and individualized analysis codes. That process also typically required directly interacting with experts from separate teams that designed the instruments and made the data products. Such a setup provided a highly specific and non-standardized avenue for anyone on the mission (or outside) to attempt to synthesize multiple instrument datasets for a more integrated picture of the observations.

Some missions have made important progress to unlock their data for the team and provided access to analysis tools that are more generically designed for heliophysics data. However, to date, the mission-wide software packages require either a significant level of detailed input from the user to direct the software to a specific mission dataset or require a minimum level of terminal-based coding on the user end to create visualizations.

When the CAVA tool is opened, users are immediately able to interact with IMAP data. Through a small number of selections, users decide if they want to visualize time-series data or map data and determine which datasets to view. All visualizations are interactive, in that the users can dynamically zoom and modify color bars by a series of clicks. Figure 45 shows an example of CAVA visualizing four years of IBEX maps, the heritage dataset used to prepare CAVA to visualize IMAP maps. In addition to visualizing data, CAVA provides advanced analysis capabilities. For example, in Fig. 45, a region toward the heliospheric nose has been manually drawn (lighter highlighted areas) and a time series of the average intensity has been extracted, shown in the bottom panel. As shown here and previously published, the heliosphere experienced a strong jump in ENA production due to a solar wind



pressure pulse reaching the outer heliosphere (McComas et al. 2018a). Previously, extracting time series from ENA map data has been a challenging and manually coded procedure. With CAVA, a user simply draws a region in the map and requests CAVA to extract a time-series from this. In this way, CAVA will unlock functionality to the entire IMAP team, which was previously reserved only for highly proficient software developers.

To develop CAVA, the CAVA software team practices Agile software development (Beck et al. 2001). The Agile methodology prescribes how software projects are managed, executed, and delivered. Key philosophies of Agile software development include user-driven designs, iterative software design, iterative development and release, and transparency in project planning. Under the umbrella of Agile principles, the CAVA software development team favors informal and immediate communication over the detailed and specific work products required by many traditional design methods. This approach allows the team to cope with change by delivering software early and often and by absorbing feedback into the development culture and ultimately into the code.

Usability and functionality are key to the success and adoption of software applications. The CAVA software team employs user research and observation to identify user needs prior to releasing the software, thus maximizing the utility of the software. Traditional software design and development follows a linear timeline, where the software is not released to users until the majority of features have been completed. The risk in that approach is that significant resources are invested before users can validate and provide feedback on the utility and usability of the software. The CAVA software development team instead employs an iterative approach where features are released and tested with users on a weekly basis. This enables the team to change features quickly to meet the evolving needs of users.

In the three years preceding IMAP launch, the CAVA software development team regularly met with IMAP science team members and tested the current versions of the software with these team members in very specific goal-oriented scenarios. By asking team members to attempt to use CAVA to perform relevant scientific analyses and observing where they had difficulties with CAVA, the software team could continuously incorporate user feedback to provide user experiences tuned to IMAP science needs. CAVA has already been used to make publication-quality figures for IBEX map data (McComas et al. 2024). By continuously refining the tool based on real scientific user feedback and using relevant heritage datasets, CAVA is immediately ready to produce publication quality scientific analyses at IMAP's launch.

## 6.3 I-ALIRT

IMAP's I-ALiRT system provides critical real-time space weather data (Lee et al. 2025). These include continuing ACE-like observations, as well as new real-time observations for testing new space weather forecasting techniques. As shown in Table 15, I-ALiRT provides ACE-like IMF, SW ions, suprathermal ions, and energetic protons space weather data products. For the magnetic field and all of the ion measurements, the cadence is significantly faster than on ACE. This is important because higher-cadence data provides more precise timing of space weather phenomena and helps to identify and eliminate erroneous samples. This latter improvement increases the overall reliability of predictions, especially for operating real-time space weather models that are directly driven by real-time data.

In addition, IMAP provides several completely new I-ALiRT observations, which were not available in the ACE real-time data. In particular, we provide in real-time both solar wind and Strahl electron observations and high-energy electron rates from large solar events that arrive well before the damaging protons and ions, allowing for a completely new advance



100 Page 68 of 82 D.J. McComas et al.

Product	IMAP source	ACE RTSW cadence	IMAP I-ALiRT cadence
Mag Field Vectors and Angles	MAG	60 s	4 s
SW Ion Moments	SWAPI	64 s	12 s
Suprathermal Ion Intensities	CoDICE	5 min	1 min
Energetic Proton Rates	HIT	5 min	1 min

None

None

None

1 min

1 min

4 min

SWE

HIT

CoDICE

Table 15 IMAP I-ALIRT real-time space weather data compared to ACE

Suprathermal Electron Rates and

Bi-Directional Flow Directions High-Energy Electron Rates

SW Charge-State Ratios

warning capability (Posner 2007). The real-time estimates of solar wind ion charge state ratios for C+6/C+5, O+7/O+6, and Fe charge states, as well as C/O, Mg/O and Fe/O ratios are provided. In addition, real-time information about the detection of counter-streaming electrons and their time-variability is included in the I-ALiRT space weather data stream. These, together with IMF and solar wind electron and ion data help enable proper identification of various solar wind structures, such as CMEs. Finally, we note that the SWFO-L1 rideshare launched with IMAP is also a space weather observatory. It has significant overlap with IMAP (solar wind electrons and ions, magnetic field, and some suprathermal particles) and some unique observations (e.g., a coronagraph), but does not have as high a cadence of observations for some measurements and is missing some of IMAP's observations, including ion charge states and very energetic ions and electrons.

I-ALiRT provide continuous real-time products through two paths. First, between the times when we are downloading our science data through DSN, IMAP continuously broadcasts I-ALiRT data, which can be picked up by antennas around the globe, as was done on prior missions (e.g., Zwickl et al. 1998; Biesecker et al. 2008), and transferred to the SOC. Alternately, during DSN contacts, the I-ALiRT data is included with the high-rate science data downlink. At these times, the IMAP MOC passes the I-ALiRT data along to the SOC in real-time.

Regardless of the path, the IMAP SOC continuously processes the I-ALiRT data and posts our space weather data products to the world-wide web for space weather users to retrieve and use. IMAP I-ALiRT products have a latency of no more than five minutes from the end of when a measurement is received by the SOC until it is available in our posted operational database. While a maximum five-minute latency is assured for times when IMAP is in contact through the DSN, IMAP has no control of the latency through NASA's various antenna partners, or even if they will collect and forward our I-ALiRT data.

### 7 Conclusions

IMAP is a remarkable mission of discovery, exploration, and deep scientific understanding, as well as providing unique and revolutionary real-time Space Weather observations. As a groundbreaking, fully instrumented space physics observatory, IMAP is the first to measure in-situ particles and fields at ~1 au that subsequently interact with the VLISM at the edges of our heliosphere, and then directly observe their effects in those distant regions through remote ENA imaging. Through this combination, along with synergistic observations of interstellar dust and the interstellar wind's helioglow, IMAP is uniquely positioned to resolve



the critical, coupled science objectives of particle acceleration and their effects on the heliosphere's interaction with the VLISM... and so much more.

Management of IMAP is also unique, with a team of outstanding scientists, engineers, technicians, administrative specialists, and others from 25 institutions, spanning 6 countries and 12 US states. These institutions include many universities, NASA centers, National Laboratories, Non-Profits, and Corporations. Most importantly, the IMAP contributors have come together and worked as a high-performance, and largely "badgeless," mission team. Throughout the development phase, work was moved between individuals and institutions as capabilities somewhere were shifted from somewhere else in the team as needed.

The IMAP team has also focused on giving young team members opportunities to grow and develop through the course of the mission, and many of our instrument and spacecraft subsystem leaders have been in those leadership roles for the very first time in this mission. One of the specific ways we did this was through our innovative Heliophysics Future Leaders (HFL) program, where we engaged select early career science team members and gave them additional mentoring along with some specific leadership training to help promote leaders in Heliophysics for the future. The program was highly successful and ran to completion with various HFL members becoming current leaders in the mission – not just future ones – as they were promoted to 1) instrument lead (IMAP-ULTRA) and then was further promoted to Project Scientist, 2) instrument lead (SWAPI), 3) two instrument deputy leads (IMAP-Lo and HIT), 4) the lead for the overall CAVA development, and 5) the deputy lead for our I-ALiRT system.

NASA also selected a Student Collaboration (StC), which was funded through a grant independent from the IMAP project. The StC can augment the IMAP science return and has already provided hands-on research experience for students and contributed to expanding participation and skills of undergraduate students in space science and engineering. This was achieved through a collaborative hardware program involving three universities that resulted in students designing, building, assembling, integrating, testing, calibrating and delivering to NASA for launch "3UCubed," a 3U-sized CubeSat with student-built instruments. Post-launch through the NASA CubeSat Launch Initiative, the students participate in joint data analysis of measurements from IMAP and the CubeSat.

Finally, we have been engaging with the broader Heliophysics community throughout the development of the mission. We have hosted annual joint IBEX/IMAP Science Team meetings, which were open to the entire community. We have given numerous talks and presentations at various meetings, workshops, and conferences throughout development and have a vibrant Communications program to engage the general public and keep everyone up to date on our mission work as IMAP goes about *Exploring Our Solar Neighborhood and its Space Weather*. Our mission web site is imap.princeton.edu and we regularly push out information and communications broadly through Facebook.com/IMAPMission and Instagram@IMAPSpaceMission... please Like, Follow, and Share us!

This paper is the citable reference for the overall IMAP mission, as well as the CMAD (Supplementary File), which will continue to evolve throughout the mission.

# Appendix: IMAP Terminology and Acronym List

**Note on Terminology** There is significant confusion about and multiple definitions/names for various regions of the outer heliosphere and local interstellar medium. In this paper, throughout the rest of the IMAP collection of papers, and generally for IMAP science going forward, we adopt the following definitions (moving from farthest outside inward):



100 Page 70 of 82 D.J. McComas et al.

**Interstellar Medium (ISM)**: the interstellar space surrounding the Sun nearby stars, including complex internal structure with regions of different physical conditions, including interstellar clouds, Local Bubbles, cold clouds, etc.

**Local Interstellar Medium (LISM)**: the more local portion of the ISM, through which the Sun moves, but beyond any influence of the heliosphere.

**Very Local Interstellar Medium (VLISM)**: the region of interstellar medium just around and influenced by the heliosphere ( $\sim$ 1000 au). This region typically defines outer boundary conditions for modeling. (Note: older terminology sometimes called this the "outer heliosheath" – we do not use that terminology).

**Heliosheath**: region between termination shock and heliopause. (Note: older terminology sometimes called this the "inner heliosheath" – we do not use that terminology).

#### Acronyms

ACE Advanced Composition Explorer

ACR Anomalous cosmic ray ACS Attitude control system

AO Announcement of Opportunity

APD Avalanche Photodiode

C&DH/CDH Command and data handling
CAVA Combined Analysis, Visualization, and Access

CDAWeb Coordinated Data Analysis Web

CDF Common Data Format
CEM Channel Electron Multiplier
CFDP CCSDS File Delivery Protocol

cFE Core Flight Executive

CIR Corotating interaction region

CMAD Calibration and Measurement Algorithms Document

CMEs Coronal Mass Ejections

CoDICE Combined Dual Ion Composition Experiment

COIN Coincidence

CSA Charge Sensitive Amplifier

CSCI Computer Software Configuration Item

DE Direct Event

DOI Digital Object Identifier

DOY Day of Year

DPU Digital processing unit
DSN Deep Space Network
Ebox Electronics box

ENA Energetic neutral atom
EP Energetic Particle
ESA Electrostatic Analyzer
FEE Front-end electronics
FOR Field of regard
FOV Field-of-view
FSW Flight Software

FWHM Full Width at Half Maximum

G Geometric factor
GCR Galactic cosmic ray
GDF Globally distributed flux



GLOWS Ly-a Helioglow Imager

GMIRs Global merged interaction regions
GSFC Goddard Space Flight Center
HFL Heliophysics Future Leaders

HiRes Hi-Resolution Mode

HIT High Energy Telescope Instrument

HiThr Hi-Throughput Mode

HSO Heliophysics Systems Observatory

HV High voltage

HVPS High Voltage Power Supply
I-ALIRT IMAP Active Link for Real-Time
IBEX Interstellar Boundary Explorer
ICE IMAP Common Electronics
ICU Instrument controller board
IDEX Interstellar Dust Experiment

IDP Interplanetary dust

IDPU Instrument Data Processing Unit

IMAP Interstellar Mapping and Acceleration Probe

IMF Interplanetary Magnetic Field INCA Ion and Neutral Camera

ISD Interstellar dust ISM Interstellar Medium ISN Interstellar neutral

JHUAPL Johns Hopkins University Applied Physics Lab

LANL Los Alamos National Laboratory

LASP Laboratory for Atmospheric and Space Physics

LET Low-Energy Telescope
LGA Low gain antenna
LISM Local interstellar medium
LOI Lissajous Orbit Insertion
LVPS Low Voltage Power Supply
MAG Magnetic Field Instrument

MAG Magnetic Field Instrument
MCP Microchannel plate imager
MGA Medium gain antenna
MHD Magnetohydrodynamic
MOC Mission Operations Center

NOAA National Oceanic and Atmospheric Administration

PB Processor Board

PCEM Primary channel electron multiplier

PDS Planetary Data System

PHASICs Pulse Height Analyzer ASICS

PMT Photomultiplier

POC Payload Operations Center PPM Pivot Platform Mechanism

PSP Parker Solar Probe

PUI Pickup ion

RPA Retarding potential analyzer
RPM Revolutions Per Minute
SBC Single board computer



100 Page 72 of 82 D.J. McComas et al.

SC or S/C Spacecraft

SCEM Secondary channel electron multiplier

SCIF Spacecraft interface card SDC Science Data Center SEP Solar energetic particles

SH Sensor Head

SMOL Science and Mission Operations Lead

SOCScience Operations CenterSPDFSpace Physics Data FacilitySPISerial peripheral interfaceSSCSwedish Space Corporation

SSD Solid-state detector

SSPA Solid-state power amplifier

ST Suprathermal

STEREO Solar Terrestrial Relations Observatory

STP Solar Terrestrial Probes SUDA Surface Dust Analyzer

SW Solar Wind

SWAP Solar Wind Around Pluto Instrument SWAPI Solar Wind and Pickup Ion Instrument

SWE Solar Wind Electron (or used to reference the SWE Instrument)

SWFO-L1 NOAA's Space Weather Follow mission to L1

T&M Theory and Modeling

TCM Trajectory correction maneuver

TOF Time-of-Flight TS Termination Shock

TTI Transfer trajectory insertion

UART Universal asynchronous receiver/transmitter

VA Variable aperture

VDF Velocity distribution function VLISM Very local interstellar medium

 $\label{lem:supplementary logorithm} \textbf{Supplementary Information} \ \ The online version contains supplementary material available at <a href="https://doi.org/10.1007/s11214-025-01224-z">https://doi.org/10.1007/s11214-025-01224-z</a>.$ 

**Acknowledgements** This mission would literally not have been possible without the truly outstanding efforts, contributions, and dedication of well over eight hundred team members and participants (list below). We are humbled to have had the privilege to work with this team and are delighted to acknowledge and thank all of these important contributors. This work is supported by the IMAP mission as a part of NASA's STP mission line (80GSFC19C0027). The contribution from GLOWS is supported by Polish Ministry for Science under contract MEiN-2021-2-DIR. The contribution by the University of Bern is supported by the ESA PRODEX Experiment Agreement Nr. 4000129386. The authors have no conflicts of interest to declare that are relevant to the content of this article.

Y. Abul-Huda, N. Ahmed, A. Ahmed, J. Albin, M. Alimaganbetov, F. Allegrini, T. Allen, G. Almodovar, B. Alterman, P. Althaus, C. Amaya, K. Anderson, J. Anderson, N. Angold, M. Antoniak, H. Atanasoff, J. Atchison, M. Athey, R. Aumiller, E. Ayari, A. Badger, P. (Penni) Baez, G. Baker, D. N. Baker, R. Bandyopadhyay. J. Baran, T. Barcinskiń, L. Bartolone, C. Battista, S. Begley, N. Behrooz, K. Ver, M. Bharatia, S. Bibelhauser, D. Biesecker, B. Bisci, P. Bland, T. Bloomer, J. Bogdanski, L. Boggs, P. Boie, C. Bollendonk, D. Bonner, J. Bonney-Ray, H. Borowski, D. Bort, A. Botting, M. Bourque, S. Bowen, J. Bower, B. Brainer, S. Bramer, N. Brennan, T. Brenner, C. Britt, S. Brock, J. Brody, E. Brookens, L. Brown, P. Brown, N. Brunner, A. Bruno, L. Brunson, M. Bryant, M. Brysch, S. Bucior, B. Buckland, P. Buedel, W. Bujwan, R. Bull, J. Burgum, L. Burke, A. Busbey, J. Bush, S. Bushman, A. Byerly, M. Bzowski, K. Cade, S. Callahan, S. Calloway, R. Cantu, G. Cardarelli, D. Carl, S. Carlson, S. Caroots, C. Carpenter, B. Carpenter, B. Carr, M. Castaño, D.



100

Caughran, J. Charan, G. Chavez, P. Chen, J. Chen, G. Chiu, S. Cho, T. Choedon, M. Choi, N. Chrissotimos, E. Christian, S. Christopherson, N. Ciaio, J. Cinotti, D. Clancy, G. Clark, J. Clemens, C. Cline, L. Coakley, I. Cohen, C. Cohen, E. Coleman, C. Collura, M. Commons, S. Conkey, C. Cook, S. Cooper, E. Cooper, M. Cooter, S. Cortinas, C. Costello, M. Cox, J. Cox, T. Cox, A. Crabtree, S. Craft, B. Craig, A. Crew, A. Crifasi, T. Crowfoot, M. Cully, A. Cummings, H. Curtis, N. Dalal, S. Dalla, A. Dalton, R. Darragh, M. Dauberman, M. Daukszo, K. Davis, M. A. Dayeh, A. De Los Santos, A. de Mattos, G. de Nolfo, T. (TJ) Deaton, J. DeBoer, C. Delmar, M. Delmont, M. Deluca, B. DeMajistre, J. Dennison, M. Desai, S. (Steve) DeVogel, P. Dharmavaram, E. Diamonte, T. Diaz, R. Dobyns, E. Doll, J. Dominico, M. Donegan, A. Doner, K. Doubleday, C. Drabenstadt, R. Drexler, A. Driskell, M. Drobik, A. Dubill, G. Duerr, B. Duffy, J. Dunbar, G. F. Dunn, A. Dupont, E. Dustin, N. Dutton, A. East, A. Eisape, P. Eisenreich, J. Eisig, V. Elizondo, H. Elliott, M. Elliott, S. Ellis, L. Ellis, D. Emmell, D. Eng, M. Epperly, J. Ercol, J. Escobar, B. Ethridge, N. Evans, D. Everett, A. Faber, K. Fairchild, H.J. Fahr, A. Fanelli, J. Farnan, E. Fattig, E. Fauchon-Jones, B. Fennimore, B. Fenton, P. Fernandes, M. Ferris, M. Fetzer, T. Fields, M. Finlayson, M. Finnegan, J. Finnigan, J. Firer, J. Fischer, M. Fisher, G. Fletcher, A. (Mae) Flores, S. Flynn, T. Fok, D. Folta, J. Fontanese, J. Ford, K. Ford, M. Fowle, K. Fox, N. Fox, T. Frankenfield, D. Frankford, P. Frisch, C. Frost, D. Fuller, H. Funsten, J. Furman, M. Furrow, S. Fuselier, G. Futch, G. Gajoch, A. Galli, T. Galvin, M. Galvin, V. Ganley, K. Gantz, F. Gao, M. Gardner, M. Gardner, M. Gargano, B. Garnett, R. Garnica, B. Garrison, C. Garza, J. Gasser, S. Gaumer, D. E. George, A. George, A. Gerger, J. Gerhardus, P. Ghosh, J. Giacalone, J. Gilbert, M. Gile, C. Gingrich, A. Githens, M. Gkioulidou, M. Goans, H. Golczynski, K. Goldee, F. Gonzales, Z. Gonzalez-Medley, A. Gorman, A. Gottwald, N. Gould, K. Grabczewski, W. Granger, M. Granoff, M. Graziano, J. Green, C. Greenaway, K. Gregory, D. Griffin, J. Griffith, G. Griffith, J. Griffiths, D. Grosh, J. Grove, G. Grubbs, F. Guo, R. Gurnee, S. Gurst, A. Guthrie, J. Hahn, D. Hahne, N. Hall, R. Hall, W. Hall, D. Hals, S. Hamilton, K. Handler, R. Hänggi, J. Hanley, M. Haque, D. Harmon, J. Harper, P. Harrington-Duff, B. Harris, M. Harrow, S. Hart, B. Harter, T. Hartka, M. Hartnett, D. Harvey, C. Haskins, J. Hayes, S. Hedman, J. Heerikhuisen, S. Hefter, K. Hegarty, B. Heggestad, S. Heirtzler, D. Heirtzler, T. Hellickson, R. Hemphill, C. Hersman, E. Hertzberg, W. Hess-Sparrow, A. Higginson, P. Hill, M. Hill, B. Hill, P. Hoeper, M. Hoff, M. Hoffmeyer, B. Holden, L. Holguin, C. Hollenhorst, A. Holtzman, G. Holtzman, D. Hooks, M. Horanyi, T. Horbury, I. Householder, S. Hoyt, P. Huang, R. Huber, C. Huber, A. Huebenthal, A. Hume, H. Hunter, J. Hutcheson, G. Iona, P. Isenberg, P. Janzen, K. Jasiński, S. Jaskulek, J. Jason, K. Jensen, D. Jeong, M. Jeunon, L. Jilek, T. Jones, M. Jones, T. Jones, M. Jones, J. Jones, D. H. Jones, C. Joyce, T. K, J. Kalirai, S. (Shri) Kanekal, D. Kataria, S. Katz, G. Kayl, P. Kaźmierczak, J. Kelley, S. Kellogg, R. Kelly, V. Kelly, J. Kelman, T. Kendric, S. Kerem, N. Kerman, S. Kha, M. Khalid, L. Ying Khoo, F. Khoury, S. Kijewski, J. Kilheffer, R. Kinder, J. Kindracki, B. King, M. Kippen, P. Kirpes, L. Kistler, E. Kitler, E. Klages, S. Knappmiller, P. Kollmann, A. Kootz, K. Korreck, A. Kostovny, R. Kosturek, J. Kovarovic, I. Kowalska-Leszczyńska, T. Kowalski, B. Krok, T. Krueger, B. Krueger, C. Krug, C. Krupiarz, C. Ku, M.A. Kubiak, S. Kubota, H. Kucharek, F. Kujawa, J. Labin, G. Lafferty, A. Lafin, B. Lafon, L. Lahtinen, W. Lam, S. Lanctot, R. Lang, S. Lange, T. Langley, B. Larsen, K. Larsen, N. Laslo, B. Lathrop, M. LeBlanc, M. Lee, C. Lee, J. Lehtonen, P. Lemmen, N. Lemon, N. Lenzi, T. Leopold, R. Leske, G. Letchworth, J. Letzer, I. Liceaga-Indart, J. Likar, J. Lin, S. Ling, C. Lippe, K, Liu, G. Livadiotis, J. Livengood, S. Livi, C. Lomax, S. P. Longworth, K. Looney, M. Lopez-Suarez, M. Love, G. Lucas, E. Luedeman, N. Lugaz, J. Luhmann, S. Lundfelt, J. Luster, K. MacKay, D. Mackey, J. Mackey, S. MacMaster, J. Madry, C. Maldonado, A. Manica, M. Mantey, E. Manuel, A. Maranto, T. Marbois, C. Mariano, M. Martin, A. Martin, J. Martinez, V. Martinez, T. Martyniak, M. Mason, K. Mathews, D. Matlin, M. Matos, J. Mattern, W. Matthaeus, L. Matthew, R. Mauler Hayes, J. Mazur, C. McCarty, P. McCauley, B. McClellan, D. McComas, I. McCormick, J. McKeever, C. McLeod, H. McNamara, N. Meckel, J. Mellert, R. Mikula, G. Miller, C. Miller, M. Miller, J. Minty, C. Miranda, C. Miranda, A. Mirońska, D. Mitchell, M. Mitchell, J. Grant Mitchell, T. Moccia, R. Mocini, E. Moebius, D. Moessner, H. Mohr, B. Molina, C. Monaco, C. Monaghan, W. Montgomerie, J. Mooney, J. Mooney, Z. Moorhead-Rosenberg, G. Moraga, J. D. Morales, M. Morden, M. Morris, J. Morrissey, J. Moser, L. Mosier Weir, K. Mostowy, J. Mukherjee, L. Munoz, R. Murphy, I. Murphy, D. Myers, D. Myers, M. Nance, U. Nass, H. Navid, J. Neher, K. Nelson, T. Nelson, G. Newcomb, K. Newsome, H. Nguyen, J. Nichols, J. Niehof, R. Nolan, T. Nolan, K. Norman, M. Nowak, J. Nuth, S. Oberg, H. O'Brien, E. Ochs, B. O'Connor, K. Ogasawara, M. Ogindo, H. Oluseyi, C. Ong, K. Ord, P. Orleański, A. Orr, O. Ortega, N. Osiander, P. Osica, C. Pankratz, S. Parikh, L. Park, A. Parker, C. Parker, K. Pavlas, A. Pearl, B. Perez, B. Perkins, I. Perreault, M. Perry, K. Persson, S. Persyn, R. Peterson, V. Petrovich, C. Pham, J. Pham, B. Phillips, D. Piazza, A. Pickerill, G. Pineda-Escobar, T. Plummer, B. Poduval, J. Polanco, J. Półtorak, A. Pontoni, V. Poovathoor, S. Pope, C. Porowski, A. Posner, R. Powers, D. Praseuth-Gwilt, M. Preston, W. Probasco, E. Provornikova, E. Pulaha, B. Qiu, K. Queen, J. Quilty, Y. Quire, A. Rader, J. (Tyler) Radomsky, F. Rahmanifard, T. Rajkowski, T. Ramirez, J. Ramirez, D. Ramsay, J. Rankin, W. Reaves, M. Reck, J. Reider, S. Reinhardt, D. Reisenfeld, D. Reiter, C. Reno, S. Renzetti, S. Reynolds, M. Reynolds, E. Reynolds, D. Rhode, C. Rhodes, J. Richardson, J. Richman, T. Ridgeway, E. Rivera Sepulveda, S. Rizo Patron, K. Roarty, H. Robb, A. Roberts, M. Roch, D. Rodriguez, M. Rodriguez, L. Rodriguez, T. Roemer, K. Rogan, T. Rogers, A. (Charles) Rohde, V. Rojas, L. Rojek, E. Rollend, N. Rome, T. Rose, C. Rose, E. Rosenberg, P. Rosendall, J. Rothkaehl, L. Roufberg, S.



100 Page 74 of 82 D.J. McComas et al.

Roy, G. Rubin, T. Rudnicki, M. Ruffolo, D. Ruggles, J. Ruiz, J. Rushforth, C. Russell, S. Rutan, S. Ryan, C. Salerno, M. Salerno, C. Sanchez, H. Sandin, B. Sandoval, L. Sandoval, G. Saurage, R. Savage, B. Savage, J. (Jeff) Sayler, T. Scarapti, J. Schellhase, J. Scherrer, C. Schiferl, T. Schlabach Wells, C. Schlemm, T. Schultz, N. Schwadron, M. Schwinger, C. Sebastian, M. Secunda, L. Segal, M. Segler, H. Seifert, K. Seith, D. Seitz, D. Sepan, A. Shah, S. Shapiro, A. Sharma, T. Sharma, S. Shaver, M. Shaw-Lecerf, J. Sheehi, M. Shen, D. (Del) Sherman, G. Shiblie, M. Shifman, A. Shin, A. Shmyk, B. Lal Shrestha, F. Siddique, A. Sikorski, M. Silber, N. Sindjui, L. Sinduji, R. Singh, M. Sinnott, R. Skoug, M. Smith, R. Smith, R. Smith, C. Smith, E. Smith, S. Smith, D. Smith, E. Smith, J. Sokol, N. Souitat, L. Christine Spalsbury, H. Spence, M. Spezio, J. Staren, M. Starkey, C. Starkey, M. Steadham, J. Steinberg, B. Stepp, Z. Sternovsky, S. Stevens, C. Stiles, B. Stilwell, J. Stinchcomb, R. Stonehirsch, S. Storms, M. Strumik, D. Suffern, P. Swaczyna, J. Szalay, E. Talaat, F. Talayera, C. Tandy, C. Taormino, M. Tapley, T. Tatoli, J. Teifert, R. Tennis, S. Thompson, S. Thompson, R. Tillman, W. Toczynski, E. Toomey, P. Torres, B. Torres Agosto, M. Touchette, J. Trevino, N. Trinh, T. Tropf, S. Tucker, C. Tucker, J. Tumlinson, T. Tunstall, M. Turek, L. Turner, D. Turner, G. Turnley, N. Tuttle, P. Twombly, K. Tyagi, N. Tzeng, C. Vantiem, L. Varanyak, D. Vassiliadis, J. Velarde, G. (Jerry) Veloz, D. Venhaus, S. Vernon, R. Verrill, C. Vigil, V. Vigil, K. Vodusek, S. Vogler, P. Wachulak, B. Wade, S. Wade, B. Wagner, B. Wallis, C. Walsh, M. Wardzińska, S. Warkala, L. Warren, R. Wawrzaszek, C. Weaver, J. Weber, S. Weidner, D. Weir, A. Wester, J. Westlake, J. White, R. White, D. White, C. Whiteley, M. Wiedenbeck, M. Wieder, K. Wielgos, E. Wilber, C. Wilkerson, J. Wilkes, J. Will, P. Wilson, B. Wilson, W. Wilson, M. Windhausen, R. Wing, M. Winkler, R. Winslow, L. Wisniewski, K. Wojciechowska, K. Wolff, L. Wray, K. S. Wrobel, L. Wu, P. Wurz, M. Wysslig-Horn, J. Yager, B. Yang, J. Yen, J. Yin, Y. Yoon, J. Yurek, G. Zank, E. Zambrzycka-Kościelnicka, T. Zawistowski, S. Zehner, D. Zhang, E. Zirnstein.

Of course, it is impossible to generate such a list, without missing a least a few important names – for those of you who we have missed, we are truly sorry and thank you also!

We also want to give special thanks to Eric Diamonte, who helped with the detailed editing of this paper and well as the overall collection of IMAP papers. Finally, we make a special acknowledgement to our recently deceased friend and colleague, Dr. Priscilla Frisch, who was a Co-I on IBEX where she made seminal scientific contributions, and IMAP where she will be sorely missed.

#### **Declarations**

**Competing Interests** The authors declare no competing interests.

Open Access This article is licensed under a Creative Commons Attribution-NonCommercial-NoDerivatives 4.0 International License, which permits any non-commercial use, sharing, distribution and reproduction in any medium or format, as long as you give appropriate credit to the original author(s) and the source, provide a link to the Creative Commons licence, and indicate if you modified the licensed material. You do not have permission under this licence to share adapted material derived from this article or parts of it. The images or other third party material in this article are included in the article's Creative Commons licence, unless indicated otherwise in a credit line to the material. If material is not included in the article's Creative Commons licence and your intended use is not permitted by statutory regulation or exceeds the permitted use, you will need to obtain permission directly from the copyright holder. To view a copy of this licence, visit <a href="https://creativecommons.org/licenses/by-nc-nd/4.0/">https://creativecommons.org/licenses/by-nc-nd/4.0/</a>.

#### References

Airapetian VS, Glocer A, Gronoff G, et al (2016) Prebiotic chemistry and atmospheric warming of early Earth by an active young Sun. Nat Geosci 9(6):452–455. https://doi.org/10.1038/ngeo2719

Allegrini F, Desai MI, Mason GM, et al (2008) Evidence for mass-per-charge-dependent acceleration of a multiple-component seed population by CME-driven interplanetary shocks near 1 AU. Astrophys J 682(1):690–696. https://doi.org/10.1086/587163

Armstrong TP, Pesses ME, Decker RB (1985) Shock drift acceleration. In: Tsurutani BT, Stone RG (eds) Collisionless shocks in the heliosphere: reviews of current research. Geophysical monograph, vol 35. AGU, Washington, DC, pp 271–285. https://doi.org/10.1029/GM035p0271

Asplund M, Amarsi AM, Grevesse N (2021) The chemical make-up of the Sun: a 2020 vision. Astron Astrophys 653:A141. https://doi.org/10.1051/0004-6361/202140445

Axford WI, Leer E, Skadron G (1977) The acceleration of cosmic rays by shock waves. In: Proceedings of the 15th International Cosmic Ray Conference, vol 11, pp 132–137



- Baker DN (2002) Space science. How to cope with space weather. Science 297(5586):1486–1487. https://doi.org/10.1126/science.1074956
- Baker DN, Kanekal SG (2008) Solar cycle changes, geomagnetic variations, and energetic particle properties in the inner magnetosphere. J Atmos Sol-Terr Phys 70(2–4):195–206. https://doi.org/10.1016/j.jastp. 2007.08.031
- Bame SJ, Glore JP, McComas DJ, et al (1983) The ISPM solar-wind plasma experiment. In: Wentzel KP, Marsden RG, Battrick B (eds) The International Solar Polar Mission: its scientific investigations. ESA Special Publication, vol SP-1050. ESA, Noordwijk, pp 47–73
- Bame SJ, McComas DJ, Barraclough BL, et al (1992) The Ulysses solar wind plasma experiment. Astron Astrophys Suppl Ser 92(2):237–265
- Baranov VB, Malama YG (1993) Model of the solar wind interaction with the local interstellar medium: numerical solution of self-consistent problem. J Geophys Res 98(A9):15157–15163. https://doi.org/10.1029/93JA01171
- Barraclough BL, Dors EE, Abeyta RA, et al (2003) The plasma ion and electron instruments for the Genesis mission. Space Sci Rev 105:627. https://doi.org/10.1023/A:1024426112422
- Beck K, Beedle M, van Bennekum A, et al (2001) The Agile Manifesto. Agile Alliance. http://agilemanifesto.org/
- Bell AR (1978) The acceleration of cosmic rays in shock fronts. Mon Not R Astron Soc 182(2):147–156. https://doi.org/10.1093/mnras/182.2.147
- Biesecker DA, Webb DF, St. Cyr OC (2008) STEREO space weather and the space weather beacon. Space Sci Rev 136:45. https://doi.org/10.1007/s11214-007-9165-7
- Blandford RD, Ostriker JP (1978) Particle acceleration by astrophysical shocks. Astrophys J 221:L29–L32. https://doi.org/10.1086/182658
- Boschini MJ, Della Torre S, Gervasi M, et al (2019) The HelMod model in the works for inner and outer heliosphere: from AMS to Voyager probes observations. Am Sociol Rev 64(12):2459–2476. https://doi.org/10.1016/j.asr.2019.04.007
- Bruno R, Carbone V (2013) The solar wind as a turbulence laboratory. Living Rev Sol Phys 10:2. https://doi.org/10.12942/lrsp-2013-2
- Bzowski M (2008) Survival probability and energy modification of hydrogen energetic neutral atoms on their way from the termination shock to Earth orbit. Astron Astrophys 488:1057–1068. https://doi.org/10.1051/0004-6361:200809393.
- Bzowski M, Swaczyna P, Kubiak MA, et al (2015) Interstellar neutral helium in the heliosphere from IBEX observations. III. Mach number of the flow, velocity vector, and temperature from the first six years of measurements. Astrophys J Suppl Ser 220:28. https://doi.org/10.1088/0067-0049/220/2/28
- Bzowski M, Czechowski A, Frisch PC, et al (2019) Interstellar neutral helium in the heliosphere from IBEX observations. VI. The He<sup>+</sup> density and the ionization state in the very local interstellar matter. Astrophys J 882:60. https://doi.org/10.3847/1538-4357/ab3462
- Bzowski M, Kubiak MA, Möbius E, Schwadron NA (2022) Breaking correlation in the inflow parameters of interstellar neutral gas in direct-sampling observations. Astrophys J 938:148. https://doi.org/10.3847/1538-4357/ac8df4
- Bzowski M, Wawrzaszek R, Strumik M, et al (2025). GLObal solar Wind Structure (GLOWS). Space Sci Rev 221. https://doi.org/10.1007/s11214-025-01230-1
- Chotoo K, Schwadron NA, Mason GM, et al (2000) The suprathermal seed population for corotating interaction region ions at 1 AU deduced from composition and spectra of H+, He++, and He+ observed on wind. J Geophys Res Space Phys 105(A10):23107–23122. https://doi.org/10.1029/1998JA000015
- Christian ER, Mitchell JG, Bruno A, et al (2025) The High-energy Ion Telescope (HIT) for the Interstellar Mapping and Acceleration Probe (IMAP) Mission. Space Sci Rev. Submitted
- Coc A, Vangioni E (2017) Primordial nucleosynthesis. Int J Mod Phys E 26(08):1741002. https://doi.org/10. 1142/S0218301317410026
- Cohen CMS, Li G, Mason GM, et al (2021) Solar energetic particles. In: Raouafi NE, Vourlidas A (eds) Solar physics and solar wind. Space physics and aeronomy collection, vol 1. Geophysical monograph, vol 258. AGU / Wiley, Hoboken, pp 133–178. https://doi.org/10.1002/9781119815600.ch4
- Cohen CMS, Alterman BL, Baker DN (2025) IMAP's role in understanding particle injection and energization throughout the heliosphere. Space Sci Rev. Submitted
- Copi CJ, Schramm DN, Turner MS (1995) Assessing Big-Bang nucleosynthesis. Phys Rev Lett 75(22):3981–3984. https://doi.org/10.1103/PhysRevLett.75.3981
- Desai MI (2017) Compact Dual Ion Composition Instrument. US Patent 9,613,789 B1, Apr 4 2017
- Desai MI, Mason GM, Dwyer JR, et al (2001) Acceleration of <sup>3</sup>He nuclei at interplanetary shocks. Astrophys J Lett 553:L89–L92. https://doi.org/10.1086/320503
- Desai MI, Mason GM, Dwyer JR, et al (2003) Evidence for a suprathermal seed population of heavy ions accelerated by interplanetary shocks near 1 AU. Astrophys J 588(2):1149–1162. https://doi.org/10.1086/374310



100 Page 76 of 82 D.J. McComas et al.

Desai MI, Mason GM, Gold RE, et al (2006) Heavy-ion elemental abundances in large solar energetic particle events and their implications for the seed population. Astrophys J 649(1):470–489. https://doi.org/10.1086/505649

- Desai MI, Ogasawara K, Ebert RW, et al (2015) An integrated time-of-flight versus residual energy subsystem for a compact dual ion composition experiment for space plasmas. Rev Sci Instrum 86(5):054501. https://doi.org/10.1063/1.4921706
- Desai MI, Ogasawara K, Ebert RW, et al (2016) Compact dual ion composition experiment for space plasmas CoDICE. J Geophys Res Space Phys 121:6632–6638. https://doi.org/10.1002/2016JA022387
- Dialynas K, Krimigis SM, Mitchell DG, et al (2013) A three-coordinate system (ecliptic, galactic, ISMF) spectral analysis of heliospheric ENA emissions using Cassini/INCA measurements. Astrophys J 778:40. https://doi.org/10.1088/0004-637X/778/1/40
- Dialynas K, Krimigis SM, Mitchell DG, et al (2017) The bubble-like shape of the heliosphere observed by Voyager and Cassini. Nat Astron 1:0115. https://doi.org/10.1038/s41550-017-0115
- Draine BT (2011) Physics of the interstellar and intergalactic medium. Princeton series in astrophysics, vol 19. Princeton University Press, Princeton
- Eastwood JP, Nakamura R, Turc L, et al (2017) The scientific foundations of forecasting magnetospheric space weather. Space Sci Rev 212:1221–1252. https://doi.org/10.1007/s11214-017-0399-8
- Fox NJ, Velli MC, Bale SD, et al (2016) The Solar Probe Plus mission: humanity's first visit to our star. Space Sci Rev 204:7–48. https://doi.org/10.1007/s11214-015-0211-6
- Funsten HO, McComas DJ, Barraclough BL (1993) Ultrathin foils used for low energy neutral atom imaging of planetary magnetospheres. Opt Eng 32(12):3090. https://doi.org/10.1117/12.149187
- Funsten HO, Harper RW, McComas DJ (2005) Absolute detection efficiency of space-based ion mass spectrometers and neutral atom imagers. Rev Sci Instrum 76:053301. https://doi.org/10.1063/1.1889465
- Funsten HO, Allegrini F, Bochsler P, et al (2009a) The Interstellar Boundary Explorer high energy (IBEX-Hi) neutral atom imager. Space Sci Rev 146:75. https://doi.org/10.1007/s11214-009-9504-y
- Funsten HO, Allegrini F, Crew GB, et al (2009b) Structures and spectral variations of the outer heliosphere in IBEX energetic neutral atom maps. Science 326:964–966. https://doi.org/10.1126/science.1180927
- Funsten HO, Allegrini FA, Reisenfeld DB, et al (2025) The Interstellar Mapping and Acceleration Probe High Energy (IMAP-Hi) Neutral Atom Imager. Space Sci Rev. Submitted
- Fuselier SA, Allegrini F, Funsten HO, et al (2009b) Width and variation of the ENA flux ribbon observed by the Interstellar Boundary Explorer. Science 326:962–964. https://doi.org/10.1126/science.1180981
- Fuselier SA, Bochsler P, Chornay D, et al (2009a) The IBEX-Lo sensor. Space Sci Rev 146:117–147. https://doi.org/10.1007/s11214-009-9495-8
- Fuselier SA, Allegrini F, Bzowski M, et al (2012) Heliospheric neutral atom spectra between 0.01 and 6 keV from IBEX. Astrophys J 754:14. https://doi.org/10.1088/0004-637X/754/1/14
- Galli A, Wurz P, Fuselier SA, et al (2014) Imaging the heliosphere using neutral atoms from solar wind energy down to 15 eV. Astrophys J 796:9. https://doi.org/10.1088/0004-637X/796/1/9
- Galli A, Baliukin I, Kornbleuth M, et al (2023) The discrepancy between observed and predicted heliospheric energetic neutral atoms below solar wind energy. Astrophys J Lett 954:L24. https://doi.org/10.3847/2041-8213/aced9b
- Giacalone J, Jokipii JR (2015) A new model for the heliosphere's "IBEX ribbon". Astrophys J Lett 812:L9. https://doi.org/10.1088/2041-8205/812/1/L9
- Giacalone J, Burgess D, Schwartz SJ, Ellison DC (1993) Ion injection and acceleration at parallel shocks: comparisons of self-consistent plasma simulations with existing theories. Astrophys J 402:550–559. https://doi.org/10.1086/172157
- Giacalone J, Fahr H, Fichtner H, et al (2022) Anomalous cosmic rays and heliospheric energetic particles. Space Sci Rev 218:22. https://doi.org/10.1007/s11214-022-00890-7
- Gkioulidou M, Opher M, Kornbleuth M, et al (2022) On the energization of pickup ions downstream of the heliospheric termination shock by comparing 0.52-55 keV observed energetic neutral atom spectra to ones inferred from proton hybrid simulations. Astrophys J Lett 931(2):L21. https://doi.org/10.3847/2041-8213/ac6beb
- Gkioulidou M, Clark GB, Mitchell DG, et al (2025) The IMAP-Ultra Energetic Neutral Atom (ENA) Imager. Space Sci Rev. Submitted
- Gloeckler G, Geiss J (2001) Heliospheric and interstellar phenomena deduced from pickup ion observations. Space Sci Rev 97:169–181. https://doi.org/10.1023/A:1011867320416
- Górski KM, Hivon E, Banday AJ, et al (2005) HEALPix: a framework for high-resolution discretization and fast analysis of data distributed on the sphere. Astrophys J 622:759–771. https://doi.org/10.1086/427976
- Gosling JT (1993) The solar flare myth. J Geophys Res Space Phys 98(A11):18937–18949. https://doi.org/ 10.1029/93JA01896



- Gosling JT, Asbridge JR, Bame SJ, et al (1981) Interplanetary ions during an energetic storm particle event: the distribution function from solar wind thermal energies to 1.6 MeV. J Geophys Res 86:547–554. https://doi.org/10.1029/JA086iA02p00547
- Gruntman M, Roelof EC, Mitchell DG, et al (2001) Energetic neutral atom imaging of the heliospheric boundary region. J Geophys Res 106:767–781. https://doi.org/10.1029/2000JA000328
- Grzedzielski S, Bzowski M, Czechowski A, et al (2010) A possible generation mechanism for the IBEX ribbon from outside the heliosphere. Astrophys J Lett 715:L84. https://doi.org/10.1088/2041-8205/715/2/L84
- Grzedzielski S, Swaczyna P, Bzowski M (2013) Heavy coronal ions in the heliosphere. II. Expected fluxes of energetic neutral He atoms from the heliosheath. Astron Astrophys 549:A76. https://doi.org/10.1051/ 0004-6361/201220104
- Heerikhuisen J, Pogorelov NV, Zank GP (2010) Pick-up ions in the outer heliosheath: a possible mechanism for the Interstellar Boundary Explorer ribbon. Astrophys J Lett 708:L126–L130. https://doi.org/10.1088/ 2041-8205/708/2/L126
- Hegarty KP, Kubota S, Cully M, et al (2025) The IMAP Observatory Overview. Space Sci Rev. Submitted Hlond M, Bzowski M, Möbius E, et al (2012) Precision pointing of IBEX-Lo observations. Astrophys J Suppl Ser 198:9. https://doi.org/10.1088/0067-0049/198/2/9
- Horányi M, Tucker S, Sternovsky Z, et al (2025) Interstellar Dust Experiment (IDEX) onboard NASA's Interstellar Mapping and Acceleration Probe (IMAP). Space Sci Rev 221. https://doi.org/10.1007/s11214-025-01230-1
- Horbury TS, O'Brien H, Carrasco Blazquez I, et al (2020) The Solar Orbiter magnetometer. Astron Astrophys 642:A9. https://doi.org/10.1051/0004-6361/201937257
- Horbury TS, O'Brien H, Greenaway C, et al (2025) The IMAP magnetometer. Space Sci Rev. Submitted Izmodenov VV, Alexashov DB (2020) Magnitude and direction of the local interstellar magnetic field inferred from Voyager 1 and 2 interstellar data and gloval heliospheric model. Astron Astrophys 633:L12. https:// doi.org/10.1051/0004-6361/201937058
- Jokipii JR (1986) Particle acceleration at a termination shock 1. Application to the solar wind and the anomalous component. J Geophys Res 91:2929. https://doi.org/10.1029/JA091iA03p02929
- Kempf S, Tucker S, Altobelli N, et al (2025) SUDA: A SUrface Dust Analyser for compositional mapping of the Galilean moon Europa. Space Sci Rev 221(1):10. https://doi.org/10.1007/s11214-025-01134-0
- Klecker B (1995) The anomalous component of cosmic rays in the 3-D heliosphere. Space Sci Rev 72:419–430. https://doi.org/10.1007/BF00768815
- Klein K-L, Dalla S (2017) Acceleration and propagation of solar energetic particles. Space Sci Rev 212:1107–1136. https://doi.org/10.1007/s11214-017-0382-4
- Kornbleuth M, Opher M, Dialynas K, et al (2023) Probing the length of the heliospheric tail with Energetic Neutral Atoms (ENAs) from 0.52 to 80 keV. Astrophys J Lett 945(1):L15. https://doi.org/10.3847/2041-8213/acbc73
- Krimigis SM, Mitchell DG, Hamilton DC, et al (2004) Magnetosphere Imaging Instrument (MIMI) on the Cassini mission to Saturn/Titan. Space Sci Rev 114:233–329. https://doi.org/10.1007/s11214-004-1410-8
- Krimigis SM, Mitchell DG, Roelof EC, et al (2009) Imaging the interaction of the heliosphere with the interstellar medium from Saturn with Cassini. Science 326:971–973. https://doi.org/10.1126/science. 1181079
- Krymsky GF (1977) A regular mechanism for the acceleration of charges particles on the front of a shock wave. Dokl Akad Nauk SSSR 234:1306–1308
- Kubiak MA, Bzowski M, Sokół JM, et al (2014) Warm breeze from the starboard bow: a new population of neutral helium in the heliosphere. Astrophys J Suppl Ser 213:29. https://doi.org/10.1088/0067-0049/ 212/2/29
- Kubiak MA, Swaczyna P, Bzowski M, et al (2016) Interstellar neutral helium in the heliosphere from IBEX observations. IV. Flow vector, Mach number, and abundance of the warm breeze. Astrophys J Suppl Ser 223:25. https://doi.org/10.3847/0067-0049/223/2/25
- Kubiak MA, Bzowski M, Kowalska-Leszczynska I, Strumik M (2021) WawHelioGlow: a model of the heliospheric backscatter glow. I. Model definition. Astrophys J Suppl Ser 254:16. https://doi.org/10.3847/1538-4365/abeb79
- Kubiak MA, Bzowski M, Swaczyna P, et al (2023) Science opportunities for IMAP-Lo observations of interstellar neutral helium, neon, and oxygen during maximum of solar activity. Astrophys J Suppl Ser 269:23. https://doi.org/10.3847/1538-4365/acf83b
- Kucharek H, Möbius E, Li W, et al (2003) On the source and acceleration of energetic He+: a long-term observation with ACE/SEPICA. J Geophys Res Space Phys 108(A10):8040. https://doi.org/10.1029/ 2003JA009938



100 Page 78 of 82 D.J. McComas et al.

Le Chat G, Issautier K, Meyer-Vernet N (2012) The solar wind energy flux. Sol Phys 279:197–205. https://doi.org/10.1007/s11207-012-9967-y

- Lee CO, Christian ER, Sandoval L, et al (2025) Space Weather Science to Enhance Forecasting with the NASA IMAP Active Link for Real-Time (I-ALiRT) System. Space Sci Rev. Submitted
- Livi S, Desai MI, Ogasawara K, et al (2025) For the Compact Dual Ion Composition Experiment: CoDICE. Space Sci Rev. Submitted
- Lodders K (2010) Solar System abundances of the elements. In: Goswami A, Reddy B (eds) Principles and perspectives in cosmochemistry. Astrophysics and space science proceedings. Springer, Berlin, pp 379–417. https://doi.org/10.1007/978-3-642-10352-0\_8
- Manuel R, Ferreira SES, Potgieter MS (2015) The effect of a dynamic inner heliosheath thickness on cosmic-ray modulation. Astrophys J 799:223. https://doi.org/10.1088/0004-637X/799/2/223
- McComas DJ, Bame SJ, Barker P, et al (1998b) Solar Wind Electron Proton Alpha Monitor (SWEPAM) for the advanced composition explorer. Space Sci Rev 86:563–612. https://doi.org/10.1023/A: 1005040232597
- McComas DJ, Bame SJ, Barraclough BL, et al (1998a) Ulysses' return to the slow solar wind. Geophys Res Lett 25:1–4. https://doi.org/10.1029/97GL03444
- McComas DJ, Allegrini F, Pollock CJ, et al (2004) Ultrathin (~10 nm) carbon foils in space instrumentation. Rev Sci Instrum 75:4863–4870. https://doi.org/10.1063/1.1809265
- McComas DJ, Allegrini F, Bagenal F, et al (2007) Diverse plasma populations and structures in Jupiter's magnetotail. Science 318:217–220. https://doi.org/10.1126/science.1147393
- McComas DJ, Allegrini F, Bagenal F, et al (2008a) The Solar Wind Around Pluto (SWAP) instrument aboard new horizons. Space Sci Rev 140:261–313. https://doi.org/10.1007/s11214-007-9205-3
- McComas DJ, Ebert RW, Elliott HA, et al (2008b) Weaker solar wind from the polar coronal holes and the whole Sun. Geophys Res Lett 35:L18103. https://doi.org/10.1029/2008GL034896
- McComas DJ, Allegrini F, Baldonado J, et al (2009c) The Two Wide-angle Imaging Neutral-atom Spectrometers (TWINS) NASA mission-of-opportunity. Space Sci Rev 142:157–231. https://doi.org/10.1007/s11214-008-9467-4
- McComas DJ, Allegrini F, Bochsler P, et al (2009a) IBEX-Interstellar Boundary Explorer. Space Sci Rev 146:11–33. https://doi.org/10.1007/s11214-009-9499-4
- McComas DJ, Allegrini F, Bochsler P, et al (2009b) Global observations of the interstellar interaction from the Interstellar Boundary Explorer (IBEX). Science 326:959–962. https://doi.org/10.1126/science.1180906
- McComas DJ, Allegrini F, Bzowski M, et al (2014) IBEX: the first five years (2009-2013). Astrophys J Suppl Ser 213:20. https://doi.org/10.1088/0067-0049/213/2/20
- McComas DM, Bzowski M, Fuselier SA, et al (2015) Local interstellar medium: six years of direct sampling by IBEX. Astrophys J Suppl Ser 220(22):1–11. https://doi.org/10.1088/0067-0049/220/2/22
- McComas DJ, Elliott HA, Weidner S, et al (2016) Pluto's interaction with the solar wind. J Geophys Res Space Phys 121(5):4232–4246. https://doi.org/10.1002/2016JA022599
- McComas DJ, Zirnstein EJ, Bzowski M, et al (2017) Seven years of imaging the global heliosphere with IBEX. Astrophys J Suppl Ser 229:41. https://doi.org/10.3847/1538-4365/aa66d8
- McComas DJ, Christian ER, Schwadron NA, et al (2018b) Interstellar Mapping and Acceleration Probe (IMAP): a new NASA mission. Space Sci Rev 214:116. https://doi.org/10.1007/s11214-018-0550-1
- McComas DJ, Dayeh MA, Funsten HO, et al (2018a) Heliosphere responds to a large solar wind intensification: decisive observations from IBEX. Astrophys J Lett 856:L10. https://doi.org/10.3847/2041-8213/ aab611
- McComas DJ, Dayeh M, Funsten H, et al (2019) Expanding global features in the outer heliosphere. Astrophys J 872(2):127–138. https://doi.org/10.3847/1538-4357/aafc2c
- McComas DJ, Bzowski M, Dayeh MA, et al (2020) Solar cycle of imaging the global heliosphere: Interstellar Boundary Explorer (IBEX) observations from 2009–2019. Astrophys J Suppl Ser 248:26. https://doi.org/10.3847/1538-4365/ab8dc2
- McComas DJ, Swaczyna P, Szalay JR, et al (2021) Interstellar pickup ion observations halfway to the termination shock. Astrophys J Suppl Ser 254:19. https://doi.org/10.3847/1538-4365/abee76
- McComas DJ, Alimaganbetov M, Beesley L, et al (2024) Fourteen years of energetic neutral atom observations from IBEX. Astrophys J Suppl Ser 270:2. https://doi.org/10.3847/1538-4365/ad0a69
- McComas DJ, Shrestha BL, Livadiotis G, et al (2025) Interstellar pickup ion observations to 60 au. Astrophys J 980:154. https://doi.org/10.3847/1538-4357/ada6b1
- Mewaldt RA, Mason GM, Gloeckler G, et al (2001) Long-term fluences of energetic particles in the heliosphere. AIP Conf Proc 598:165–170. https://doi.org/10.1063/1.1433995
- Mewaldt RA, Cohen CMS, Cook RW, et al (2008) The Low-Energy Telescope (LET) and SEP central electronics for the STEREO mission. Space Sci Rev 136:285–362. https://doi.org/10.1007/s11214-007-9288-x



- Mitchell DG, Jaskulek SE, Schlemm CE, et al (2000) High Energy Neutral Atom (HENA) imager for the IMAGE mission. Space Sci Rev 91:67–112. https://doi.org/10.1023/A:1005207308094
- Mitchell DG, Brandt PC, Westlake JH, et al (2016) Energetic particle imagining: the evolution of techniques in imaging high-energy neutral atom emissions. J Geophys Res 121:8804–8820. https://doi.org/10.1002/ 2016JA022586
- Möbius E, Fuselier S, Granoff M, et al (2008) Time-of-flight detector system of the IBEX-Lo sensor with low background performance for heliospheric ENA detection. In: Caballero R et al (eds) Proceedings of the 30th International Cosmic Ray Conference, vol 1. UNAM, Mexico City, pp 841–844
- Möbius E, Bochsler P, Bzowski M, et al (2009) Direct observations of interstellar H, He, and O by the Interstellar Boundary Explorer. Science 326:969. https://doi.org/10.1126/science.1180971
- Möbius E, Bochsler P, Bzowski M, et al (2012) Interstellar gas flow parameters derived from Interstellar Boundary Explorer-Lo observations in 2009 and 2010: analytical analysis. Astrophys J Suppl Ser 198:11. https://doi.org/10.1088/0067-0049/198/2/11
- NASA (2014) 2014 NASA Science Plan, Doc. No. NP-2014-01-964-HQ, National Aeronautics and Space Administration Headquarters, Washington, DC
- Nass HU, Zoennchen JH, Lay G, Fahr HJ (2006) The TWINS-LAD mission: observations of terrestrial Lyman-α fluxes. Astrophys Space Sci Trans 2:27–31. https://doi.org/10.5194/astra-2-27-2006
- National Research Council (2013) National research council, solar and space physics: a science for a technological society. The National Academies Press, Washington. https://doi.org/10.17226/13060
- Neugebauer M, Steinberg JT, Tokar RL, et al (2003) Genesis on-board determination of the solar wind flow regime. Space Sci Rev 105:661–679. https://doi.org/10.1023/A:1024478129261
- O'Brien H, Brown P, Beek T, et al (2007) A radiation tolerant digital fluxgate magnetometer. Meas Sci Technol 18:3645. https://doi.org/10.1088/0957-0233/18/11/050
- Opher M, Loeb A, Drake J, Toth G (2020) A small and round heliosphere suggested by magnetohydrodynamic modelling of pick-up ions. Nat Astron 4:675–683. https://doi.org/10.1038/s41550-020-1036-0
- Park JW, Kucharek H, Möbius E, et al (2016) IBEX observations of secondary interstellar helium and oxygen distributions. Astrophys J 833:130. https://doi.org/10.3847/1538-4357/833/2/130
- Parker EN (1961) The stellar-wind regions. Astrophys J 134:20. https://doi.org/10.1086/147124
- Pogorelov NV, Heerikhuisen J, Roytershteyn V, et al (2017) Three-dimensional features of the outer heliosphere due to coupling between the interstellar and heliospheric magnetic field. V. The bow wave, heliospheric boundary layer, instabilities, and magnetic reconnection. Astrophys J 845(1):9. https://doi.org/10.3847/1538-4357/aa7d4f
- Porowski C, Bzowski M (2024) WawHelioIonMP: a semiempirical tool for the determination of latitudinal variation in the ionization rate of interstellar hydrogen and the solar wind. Astrophys J 967:57. https://doi.org/10.3847/1538-4357/ad3c3d
- Porowski C, Bzowski M, Tokumaru M (2022) A new 3D solar wind speed and density model based on interplanetary scintillation. Astrophys J 259:2. https://doi.org/10.3847/1538-4365/ac35d7
- Posner A (2007) Up to 1-hour forecasting of radiation hazards from solar energetic ion events with relativistic electronics. Space Weather 5:S05001. https://doi.org/10.1029/2006SW000268
- Pulkinnen A, Rastatter L, Kuznetsova M, et al (2013) Community-wide validation of geospace model ground magnetic field perturbation predictions to support model transition to operations. Space Weather 11:369–385. https://doi.org/10.1002/swe.20056
- Rachev M, Srama R, Srowig A, Grün E (2004) Large area mass analyzer. Nucl Instrum Methods Phys Res, Sect A 535:162–164. https://doi.org/10.1016/j.nima.2004.07.121
- Rankin JS, McComas DJ, Alimaganbetov M, et al (2025) The Solar Wind and Pickup Ion Instrument (SWAPI) on NASA's Interstellar Mapping and Acceleration Probe. Space Sci Rev 221. https://doi.org/ 10.1007/s11214-025-01229-8
- Reeves GD, Spence HE, Henderson MG, et al (2011) Electron acceleration in the heart of the Van Allen radiation belts. Science 341:991–994. https://doi.org/10.1126/science.1237743
- Reisenfeld DB, Bzowski M, Funsten HO, et al (2021) A three-dimensional map of the heliosphere from IBEX. Astrophys J Suppl Ser 254(2):40. https://doi.org/10.3847/1538-4365/abf658
- Reisenfeld DB, Allegrini FA, Christian ER, et al (2025) Exploring the Outer Heliosphere through ENA Observations from IMAP. Space Sci Rev. Submitted
- Reno C, Lafferty G, Lucas G, et al (2025) Science and Mission Operations of the Interstellar Mapping and Acceleration Probe (IMAP) Mission. Space Sci Rev. Submitted
- Rhode RA, Muller RA (2005) Cycles in fossil diversity. Nature 434:208. https://doi.org/10.1038/nature03339
  Rodríguez Moreno DF, Wurz P, Saul L, et al (2013) Evidence of direct detection of interstellar deuterium in the local interstellar medium by IBEX. Astron Astrophys 557:A125. https://doi.org/10.1051/0004-6361/201321420
- Saul L, Wurz P, Rodriguez D, et al (2012) Local interstellar neutral hydrogen sampled in-situ by IBEX. Astrophys J Suppl Ser 198:14. https://doi.org/10.1088/0067-0049/198/2/14



100 Page 80 of 82 D.J. McComas et al.

Scherer K, Fichtner H, Stawicki O (2002) The influence of the interstellar medium on the environment of the Earth. J Atmos Sol-Terr Phys 64:795–804. https://doi.org/10.1016/S1364-6826(02)00078-0

- Schwadron NA, Bzowski M, Crew GB, et al (2009) Comparison of Interstellar Boundary Explorer observations with 3d global heliospheric models. Science 326:966–968. https://doi.org/10.1126/science. 1180986
- Schwadron NA, Spence HE, Came R (2011) Does the space environment affect the ecosphere? Eos Trans AGU 92:297. https://doi.org/10.1029/2011EO360001
- Schwadron NA, Adams FC, Christian ER, et al (2014b) Global anisotropies in TeV cosmic rays related to the sun's local galactic environment from IBEX. Science 343:988–990. https://doi.org/10.1126/science. 1245026
- Schwadron NA, Blake JB, Case AW, et al (2014a) Does the worsening galactic cosmic radiation environment observed by CRaTER preclude future manned deep space exploration? Space Weather 12:622–632. https://doi.org/10.1002/2014SW001084
- Schwadron NA, Möbius E, Leonard T, et al (2015) Determination of interstellar He parameters using five years of data from the IBEX: beyond closed form approximations. Astrophys J Suppl Ser 220:25. https://doi.org/10.1088/0067-0049/220/2/25
- Schwadron NA, Möbius E, McComas DJ, et al (2016) Determination of interstellar O parameters using the first two years of data from the Interstellar Boundary Explorer. Astrophys J 828:82. https://doi.org/10.3847/0004-637X/828/2/81
- Schwadron NA, Möbius E, McComas DJ, et al (2022) Interstellar neutral He parameters from crossing parameter tubes with the Interstellar Mapping and Acceleration Probe informed by 10 yr of Interstellar Boundary Explorer observations. Astrophys J Suppl Ser 258:7. https://doi.org/10.3847/1538-4365/ac2fs9
- Schwadron N, Shen M, Amaya C, et al (2025) The IMAP-Lo instrument. Space Sci Rev 221. https://doi.org/ 10.1007/s11214-025-01234-x
- Shaviv NJ, Veizer J (2003) Celestial driver of Phanerozoic climate? GSA Today 13:4–10. https://doi.org/10. 1130/1052-5173(2003)013<0004:CDOPC>2.0.CO;2
- Skoug RM, Schultz TB, Venhaus DM, et al (2025) The Solar Wind Electron (SWE) Instrument for the Interstellar Mapping and Acceleration Probe Mission. Space Sci Rev. Submitted
- Sokół JM, Bzowski M, Tokumaru M, et al (2013) Heliolatitude and time variations of solar wind structure from in-situ measurements and interplanetary scintillation observations. Sol Phys 285:167–200. https://doi.org/10.1007/s11207-012-9993-9
- Sokół JM, McComas DJ, Bzowski M, Tokumaru M (2020) Sun-heliosphere observation-based ionization rates model. Astrophys J 897:179. https://doi.org/10.3847/1538-4357/ab99a4
- Sokół JM, Lin J, Fuselier SA, et al (2024) Diamond-like carbon conversion surfaces for space applications. J Appl Phys 135:185301. https://doi.org/10.1063/5.0203686
- Srama R, Ahrens TJ, Altobelli N, et al (2004) The Cassini cosmic dust analyzer. Space Sci Rev 114:465–518. https://doi.org/10.1007/s11214-004-1435-z
- Sternovsky Z, Amyx K, Bano G, et al (2007) The Large Area Mass Analyzer (LAMA) for in-situ chemical analysis of interstellar dust particles. In: Krueger H, Graps A (eds) Dust in planetary systems. ESA Special Publication, vol 643, pp 205–208
- Sternovsky Z, Gr"un E, Drake K, et al (2011) Novel instrument for dust astronomy: dust telescope. In: 2011 aerospace conference. IEEE, pp 1–8. https://doi.org/10.1109/aero.2011.5747300
- Sternovsky Z, Gemer A, Grün E, et al (2015) Hyperdust: an advanced in-situ detection and chemical analysis of microparticles in space. In: 2015 IEEE Aerospace Conference. IEEE, pp 1–10. https://doi.org/10. 1109/AERO.2015.7119085
- Stone E, Frandsen A, Mewaldt R, et al (1998) The Advanced Composition Explorer. Space Sci Rev 86:1–22. https://doi.org/10.1023/A:1005082526237
- Swaczyna P, Bzowski M (2017) Modeling emission of heavy energetic neutral atoms from the heliosphere. Astrophys J 846:128. https://doi.org/10.3847/1538-4357/aa862b
- Swaczyna P, Grzedzielski S, Bzowski M (2014) Assessment of energetic neutral He atom intensities expected from the IBEX ribbon. Astrophys J 782:106. https://doi.org/10.1088/0004-637X/782/2/106
- Swaczyna P, Grzedzielski S, Bzowski M (2017) Helium energetic neutral atoms from the heliosphere: perspectives for future observations. Astrophys J 840:75. https://doi.org/10.3847/1538-4357/aa6d5b
- Swaczyna P, Kubiak MA, Bzowski M, et al (2022a) Very local interstellar medium revealed by complete solar cycle of interstellar neutral helium observations with IBEX. Astrophys J Suppl Ser 259:42. https:// doi.org/10.3847/1538-4365/ac4bde
- Swaczyna P, Schwadron NA, Möbius E, et al (2022b) Mixing interstellar clouds surrounding the Sun. Astrophys J Lett 937:L32. https://doi.org/10.3847/2041-8213/ac9120
- Swaczyna P, Bzowski M, Kubiak MA (2025) Production and loss processes of hydrogen energetic neutral atoms in the heliosphere from 5 eV to 500 keV. Astrophys J Suppl Ser 277:17. https://doi.org/10.48550/arXiv.2411.13174



- Szalay JR, Provornikova E, Ayari E, et al (2025) Direct Samples of Interstellar and Interplanetary Material with IMAP. Space Sci Rev. Submitted
- Tan LC, Mason GM, Klecker B, Hovestadt D (1989) Seed population for about 1 MeV per nucleon heavy ions accelerated by interplanetary shocks. Astrophys J 345:572–583. https://doi.org/10.1086/167931
- Tapping KF (2013) The 10.7 cm solar radio flux (F10.7). Space Weather 11:1–13. https://doi.org/10.1002/swe.20064
- Todd P (1994) Cosmic radiation and evolution of life on Earth: roles of environment, adaptation, and selection. Adv Space Res 14:305–313. https://doi.org/10.1016/0273-1177(94)90483-9
- Trotta D, Valentini F, Burgess D, Servidio S (2021) Phase space transport in the interaction between shocks and plasma turbulence. Proc Natl Acad Sci 118(21):e2026764118. https://doi.org/10.1073/pnas. 2026764118
- Tsurutani BT, Lin RP (1985) Acceleration of greater than 47 keV ions and greater than 2 keV electrons by interplanetary shocks at 1 AU. J Geophys Res 90:1–11. https://doi.org/10.1029/JA090iA01p00001
- Tsurutani BT, Gonzalez WD, Gonzalez ALC, et al (2006) Corotating solar wind streams and recurrent geomagnetic activity: a review. J Geophys Res 111:A07S01. https://doi.org/10.1029/2005JA011273
- Turner MS (2022) The road to precision cosmology. Annu Rev Nucl Part Sci 72:1–35. https://doi.org/10. 1146/annurev-nucl-111119-041046
- Verscharen D, Klein KG, Maruca BA (2019) The multi-scale nature of the solar wind. Living Rev Sol Phys 16:5. https://doi.org/10.1007/s41116-019-0021-0
- Westlake JH, Mitchell DG, Gkioulidou M, et al (2020) Heliospheric maps from Cassini INCA early in the cruise to Saturn. Astrophys J 902:L45. https://doi.org/10.3847/2041-8213/abbd9e
- Weygand JM, Matthaeus WH, Dasso S, et al (2011) Correlation and Taylor scale variability in the interplanetary magnetic field fluctuations as a function of solar wind speed. J Geophys Res 116:A08102. https:// doi.org/10.1029/2011JA016621
- Wurz P (2000) Detection of energetic neutral particles. In: Scherer K, Fichtner H, Marsch E (eds) The outer heliosphere: beyond the planets. Copernicus Gesellschaft e.V.: Katlenburg-Lindau, Germany, pp 251–288. ISBN 3-9804862-3-0
- Wurz P, Aellig MR, Bochsler PA, et al (1995) Neutral atom imaging mass spectrograph. Opt Eng 34(8):2365. https://doi.org/10.1117/12.205660
- Wurz P, Fuselier SA, Möbius E, et al (2009) IBEX backgrounds and signal-to-noise ratio. Space Sci Rev 146:173–206. https://doi.org/10.1007/s11214-009-9515-8
- Zank GP (2015) Faltering steps into the galaxy: the boundary regions of the heliosphere. Annu Rev Astron Astrophys 53:449–500. https://doi.org/10.1146/annurev-astro-082214-122254
- Zank GP, Frisch PC (1999) Consequences of a change in the galactic environment of the sun. Astrophys J 518:965. https://doi.org/10.1086/307320
- Zank GP, Heerikhuisen J, Pogorelov V, et al (2010) Microstructure of the heliospheric termination shock: implications for energetic neutral atom observations. Astrophys J 708(2):1092. https://doi.org/10.1088/0004-637X/708/2/1092
- Zirnstein EJ, Heerikhuisen J, Zank GP, et al (2014) Charge-exchange coupling between pickup ions across the heliopause and its effect on energetic neutral hydrogen flux. Astrophys J 783(2):129. https://doi.org/10.1088/0004-637X/783/2/129
- Zirnstein EJ, Heerikhuisen J, McComas DJ (2015) Structure of the Interstellar Boundary Explorer ribbon from secondary charge-exchange at the solar–interstellar interface. Astrophys J 804:L22. https://doi.org/10.1088/2041-8205/804/1/L22
- Zirnstein EJ, Heerikhuisen J, McComas DJ, et al (2018) Simulation of the solar wind dynamic pressure increase in 2014 and its effect on energetic neutral atom fluxes from the heliosphere. Astrophys J 859:104. https://doi.org/10.3847/1538-4357/aac016
- Zirnstein EJ, Giacalone J, Kumar R, et al (2020) Turbulence in the local interstellar medium and the IBEX ribbon. Astrophys J 888:29. https://doi.org/10.3847/1538-4357/ab594d
- Zirnstein EJ, Kim TK, Dayeh MA, et al (2022) Explanation of heliospheric energetic neutral atom fluxes observed by the Interstellar Boundary Explorer. Astrophys J Lett 937:L38. https://doi.org/10.3847/2041-8213/ac92e2
- Zucker C, Goodman AA, Alves J, et al (2022) Star formation near the Sun is driven by expansion of the Local Bubble. Nature 601:334–337. https://doi.org/10.1038/s41586-021-04286-5
- Zwickl RD, Doggett KA, Sahm S, et al (1998) The NOAA Real-Time Solar-Wind (RTSW) system using ACE data. Space Sci Rev 86:633–648. https://doi.org/10.1023/A:1005044300738

**Publisher's Note** Springer Nature remains neutral with regard to jurisdictional claims in published maps and institutional affiliations.



100 Page 82 of 82 D.J. McComas et al.

#### **Authors and Affiliations**

D.J. McComas<sup>1</sup> • E.R. Christian<sup>2</sup> · N.A. Schwadron<sup>3</sup> · M. Gkioulidou<sup>4</sup> · F. Allegrini<sup>5,6</sup> · D.N. Baker<sup>7</sup> · M. Bzowski<sup>8</sup> · G. Clark<sup>4</sup> · C.M.S. Cohen<sup>9</sup> · I. Cohen<sup>4</sup> · C. Collura<sup>4</sup> · M.J. Cully<sup>4</sup> · S. Dalla<sup>10</sup> · M.I. Desai<sup>5,6</sup> · A. Driesman<sup>4</sup> · D. Eng<sup>4</sup> · N.J. Fox<sup>11</sup> · H.O. Funsten<sup>12</sup> · S.A. Fuselier<sup>5,6</sup> · A. Galli<sup>13</sup> · J. Giacalone<sup>14</sup> · J. Hahn<sup>4</sup> · K.P. Hegarty<sup>4</sup> · T. Horbury<sup>15</sup> · M. Horanyi<sup>7</sup> · L.M. Kistler<sup>3</sup> · M.A. Kubiak<sup>5</sup> · S. Kubota<sup>4</sup> · S. Livi<sup>5</sup> · N. Lugaz<sup>3</sup> · C.O. Lee<sup>16</sup> · J. Luhmann<sup>16</sup> · W. Matthaeus<sup>17</sup> · D.G. Mitchell<sup>4</sup> · J.G. Mitchell<sup>2</sup> · E. Moebius<sup>3</sup> · S. Pope<sup>5</sup> · E. Provornikova<sup>4</sup> · J.S. Rankin<sup>1</sup> · D.B. Reisenfeld<sup>12</sup> · C. Reno<sup>1</sup> · J.D. Richardson<sup>18</sup> · C.T. Russell<sup>19</sup> · M.M. Shaw-Lecerf<sup>1</sup> · J. Scherrer<sup>4</sup> · R.M. Skoug<sup>12</sup> · M.M. Shen<sup>1</sup> · H.E. Spence<sup>3</sup> · Z. Sternovsky<sup>7</sup> · M. Strumik<sup>8</sup> · J.R. Szalay<sup>1</sup> · M. Tapley<sup>5</sup> · M. Tokumaru<sup>20</sup> · D.L. Turner<sup>4</sup> · S. Weidner<sup>1</sup> · J. Westlake<sup>11</sup> · P. Wurz<sup>11</sup> · G.P. Zank<sup>21,22</sup>

 □ D.J. McComas dmccomas@princeton.edu

- Department of Astrophysical Sciences, Princeton University, Princeton, NJ 08544, USA
- <sup>2</sup> Heliophysics Science Division, NASA Goddard Space Flight Center, Greenbelt, MD 20771, USA
- Space Science Center, University of New Hampshire, Durham, NH 03824, USA
- Johns Hopkins University Applied Physics Laboratory, Laurel, MD 20723, USA
- Southwest Research Institute, San Antonio, TX 78228, USA
- Department of Physics and Astronomy, University of Texas at San Antonio, San Antonio, TX 78249, USA
- Laboratory for Atmospheric and Space Physics, University of Colorado Boulder, Boulder, CO 80303, USA
- Space Research Centre, Polish Academy of Sciences (CBK PAN), Bartycka 18A, Warsaw, Poland
- Galifornia Institute of Technology, Pasadena, CA 91125, USA
- <sup>10</sup> University of Lancashire, Preston PR1 2HE, UK
- Science Mission Directorate, NASA Headquarters, Washington D.C. 20546, USA
- Los Alamos National Laboratory, Los Alamos, NM 87545, USA
- Space Research & Planetary Sciences, Physics Institute, University of Bern, Bern, Switzerland
- Department of Planetary Sciences, University of Arizona, Tucson, AZ 85721, USA
- 15 Imperial College London, South Kensington, London SW7 2AZ, UK
- Space Sciences Laboratory, University of California, Berkeley, CA 94720, USA
- Department of Physics and Astronomy, University of Delaware, Newark, DE 19716, USA
- Kavli Center for Astrophysics and Space Science, Massachusetts Institute of Technology, Cambridge, MA 02139, USA
- Department of Earth, Planetary, and Space Sciences, University of California, Los Angeles, CA 90095, USA
- Nagoya University, Nagoya 464-8601, Japan
- Department of Space Science, University of Alabama in Huntsville, Huntsville, AL 35899, USA
- Center for Space Plasma and Aeronomic Research (CSPAR), University of Alabama in Huntsville, Huntsville, AL 35805, USA

